Monitoring and characterization of abnormal process conditions in resistance spot welding

By

Bobin Xing

A thesis submitted for the degree of

Doctor of Philosophy

of The Australian National University

16th of April 2018

Declaration

I hereby declare that I am the sole author of this thesis. This is a true copy of the thesis, including any required final revisions, as accepted by my examiners.

I understand that my thesis may be made electronically available to the public.

Bobin Xing

April 2018

Dedication

To my loving parents

Acknowledgement

Supervisory Panel

Prof. Qinghua Qin, The Australian National University, Chair of Panel

Dr. Yi Xiao, The Australian National University, Secondary Supervisor

Prof. Wugui Jiang, Nanchang Hangkong University, Secondary Supervisor

Abstract

Resistance spot welding (RSW) is extensively used for sheet metal joining of body-in-white (BIW) structure in the automobile industry. Key parameters, such as welding current, electrode force and welding time, are involved in the RSW process. Appropriate welding parameters are vital for producing good welds; otherwise, undersized weld and expulsion are likely to be caused. For a specific type of sheet metal, an acceptable nugget is produced when an appropriate combination of welding parameters is used. However, undersized welds and expulsion are still commonly seen in the plant environment, where some abnormal process conditions could account for the production of the poor quality welds.

Understanding the influence of abnormal process conditions on spot weld quality and other RSW related issues is crucial. A range of online signals, strongly related to the nugget development history, have attracted keen interest from the research community. Recent monitoring systems established the applied dynamic resistance (DR) signal, and good prediction of nugget diameter was made based on signal values. However, the DR curves with abnormal process conditions did not agree well with those under normal condition, making them less useful in detecting abnormal process conditions. More importantly, none of the existing monitoring systems have taken these abnormal process conditions into account. In addition, electrode degradation is one of the most important issues in the plant environment. Two major electrode degradation mechanisms, softening and intermetallic compound (IMC) formation, are strongly related to the characteristics of welding parameters and sheet metals. Electrode misalignment creates a very distinct temperature history of the electrode tip face, and is believed to affect the electrode degradation mechanism. Though previous studies have shown that electrode misalignment can shorten electrode life, the detailed mechanism is still not understood.

In this study, an online-monitoring system based on DR curve was first established via a random forest (RF) model. The samples included individual welds on the tensile shear test sample and welds on the same sheet, considering the airgap and shunting effect. It was found that the RF model achieved a high classification accuracy between good and poor welds. However, the DR signals were affected by the shunting distance, and they displayed opposite trends against individual welds made without any shunting effect. Furthermore, a suitable online signal, electrode displacement (ED), was proposed for monitoring abnormal process conditions such as shunting, air gap and close edged welds. Related to the thermal expansion of sheet metal, ED showed good consistency of profile features and actual nugget diameters between abnormal and normal welds. Next, the influence of electrode misalignment on electrode degradation of galvannealed steel was qualitatively and quantitatively investigated. A much-reduced electrode life was found under the angular misalignment of 5°. Pitting and electrode softening were accelerated on the misaligned electrodes. δ Fe-Zn phase from the galvannealed layer that extends electrodes was found non-uniformly distributed on the worn electrode. Furthermore, electron backscatter diffraction (EBSD) analysis was implemented on the worn electrode, showing marked reduction in grain diameter and aspect ratio. The grain deformation capacity was estimated by the distribution of the Taylor factor, where the portion of <111> pore grain was substantially weakened in the recrystallized region compared to the base metal region.

CONTENT

List of Tables

List of Figures

XIII

Acronyms

AC	Alternating Current
ANN	Artificial Neural Network
AUC	Area Under Curve
BIW	Body-in-White
BM	Base Metal
BPNN	Back Propagation Neural Network
CCD	Charge-coupled Device
CTT	Cross Tension Test
CV	Cross Validation
DC	Condensator Discharge
DR	Dynamic Resistance
EBSD	Electron Backscatter Diffraction
ED	Electrode Displacement
EDS	Energy-dispersive Spectrometer
EF	Electorde Force
GA	Galvannealed Steel
GB	Galvanized Steel
HAZ	Heat Affected Zone
HT	Hold Time
HMM	Hidden Markov Model
IF	Interficial Failure
IMC	Intermetallic Compound
KAM	Kernal Average Misorientation
LVN	Linear Vector Quantization
MFDC	Medium Frequency Direct Current
MR	Moving Range

ND	Normal Direction
OM	Optical Microscope
OOB	Out-of-Bag
RD	Rolling Direction
RF	Random Forest
RMS	Root Mean Square
ROC	Receiver Operating Characteristic
RSW	Resistance Spot Welding
PCA	Principal Component Analysis
PF	Pull-out Failure
PNN	Probabilistic Neural Network
SEM	Scanning Electron Microscope
SVM	Supporting Vector Machine
TD	Transverse Direction
TSS	Tensile Shear Strength
TST	Tensile Shear Test
UO	Ultrasonic Osillagram
WC	Welding Current
WT	Welding Time

Chapter 1 Introduction

1.1 Background

Resistance spot welding (RSW) is extensively used for joining sheet metals in the automobile and aircraft industries. Due to its ease of manufacturing and rapid production rate, RSW is used as a joining technique in body-in-white (BIW) structures. It is reported that a BIW structure consists of 4000 -5000 spot welds [1]. A typical RSW process can be divided into four stages: squeezing, welding, hold and cooling, as presented in Figure 1.1
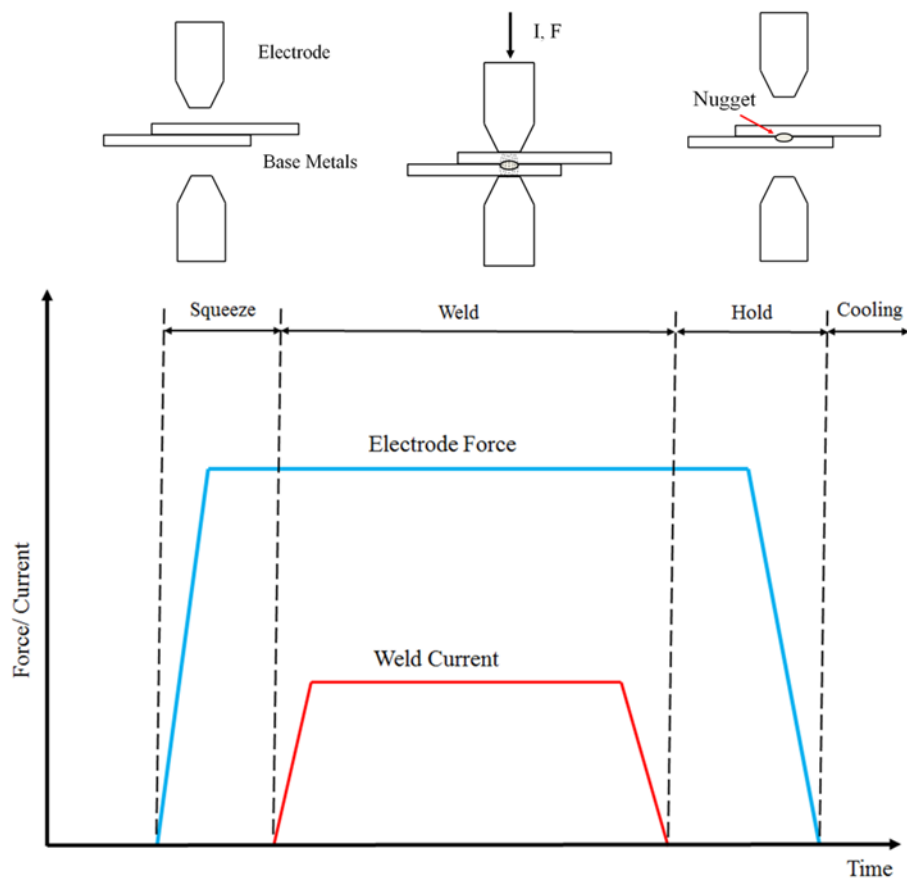
Figure 1.1 Typical RSW welding schedule

In the squeezing stage, the electrodes approach each other and the base metals (BM) are clamped by a constant electrode force. The welding stage follows the squeezing stage. The welding current transmits through the electrodes and the base metal, and the heat generated due to Joule's law melts the base metals and causes two separate sheets to join. The electrode force remains exerted during the welding stage. In the hold stage, the welding current is cut off, and the electrodes remain clamped for complete cooling of the molten liquid. Then, a nugget is formed.
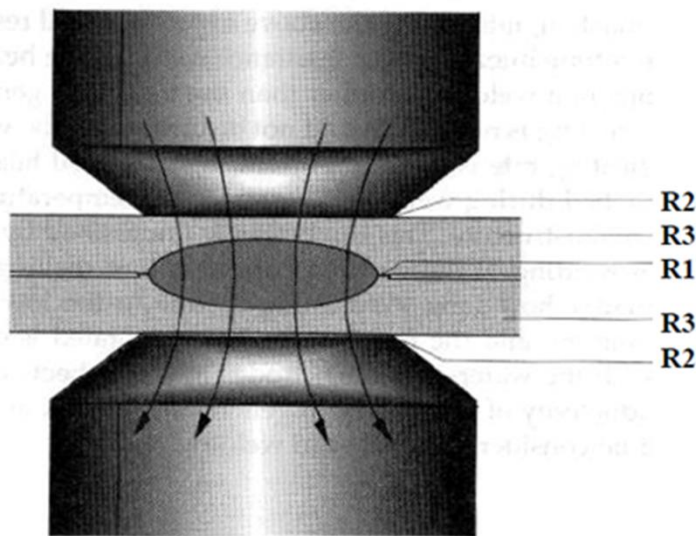
Figure 1.2 Schematic diagram of resistance spot welding [2]

Figure 1.2 presents a schematic diagram of the welding stage. The welding current transmits through the upper electrode, the base metals and the lower electrode. Joules' law can be described by:

$$Q(t) = \int_0^T i^2(t)R(t)dt$$

(1.1)

where Q is the heat generated, i is the welding current, R is the resistance in the circuit, t is the time and T is the total welding time. It can be inferred that welding current I and welding time T are two primary components in Joule heating. The resistance R is

2

comprised of the contact resistance and bulk resistance, both of which are strongly related to the physical properties of the base metals and the contact condition. The electrode force has been experimentally and theoretically proved to impact the contact resistance at the faying surface. Thus, heat generation is a function of welding current, welding time and electrode force. For a specific type of sheet metal, an acceptable nugget is produced when an appropriate combination of welding parameters is used. However, undersized welds and expulsion are still commonly seen in the plant environment, where some abnormal process conditions can account for the production of the poor quality welds.

1.2 Current issues

Abnormal process conditions in the RSW process include the shunting effect, airgap due to mechanical deformation of the sheet, closed edge welds and electrode misalignment, all which are sometimes inevitable in the plant environment. These abnormal process conditions affect heat generation at the faying surface and the sheet/electrode interface. Thus, they cause a substantial decline in nugget size and a high tendency to expulsion. They are also considered to have detrimental influences on electrode degradation. However, existing online monitoring systems in the plant environment do not properly consider these abnormal process conditions in the plant environment. Moreover, the actual influence on electrode degradation is not fully understood.

The objective of this thesis is to introduce a proper online system for monitoring abnormal process conditions. The following tasks are accomplished:

1) Construct a random forest based online monitoring system based on dynamic signals in the RSW process.

2) Propose an appropriate online signal (i.e. electrode displacement) to characterize abnormal process conditions in RSW process.

3) Analyze the influence of abnormal process conditions on electrode degradation, especially for galvannnealed steel and galvanized steel.

1.3 Thesis outline

In this thesis, Chapter 2 presents a literature review of subjects related to abnormal process conditions, electrode degradation and existing online monitoring systems in RSW. Chapter 3 introduces the material and experimental methodology used in this thesis. In Chapter 4, a random forest based online monitoring system is proposed based on the RSW dynamic signals. Chapter 5 compares two popular dynamic signals for characterizing abnormal process conditions. In Chapter 6, the detrimental influence of electrode misalignment on the electrode degradation is presented, using both qualitative and quantitative methods.

Chapter 2 Literature Review

2.1 Materials in resistance spot welding

2.1.1 Base metal

Steel has been widely used in the automobile industry, due to its good weldability and mechanical properties. An acceptable nugget is produced with moderate welding current and electrode force. Zinc coating has been added to render good corrosion resistance of steel. Two typical zinc coating are galvanized coating and galvannealed (GA) coating. Hot-dip galvanized coating usually consists of a thick layer of η phase (pure Zn). The hot-dip coating is uneven in thickness. Thus, the welding factor can vary from weld to weld. Due to the low melting point of the zinc coating, it is difficult to preserve the integrity of the coating. In addition, GA coating comprises several layers of Fe-Zn intermetallic compounds after annealing at 500 °C [3]. Apart from Zn coating, the influences of Al-Sn coating and Zn-Al coating on weldability and electrode life have been thoroughly investigated [4, 5].

Spot welding of stainless steel has also been investigated, due to its superior mechanical strength and corrosion resistance. High electrical resistance renders it easy to join by RSW. The compositions of stainless steel play crucial roles in the final nugget performance. Two phases in austenitic stainless steel, austenite and ferrite, have been found to affect the strength in heat affected zone (HAZ) and nugget and in fatigue strength [6, 7]. Resistance spot welding of ferritic stainless steel is involved in phase transformation in the HAZ and nugget zone [8].

2.1.2 Electrode material

RWMA recommends a range of electrodes in RSW, including A1-1 Cu, A2-1 Cu-Cr, A2-2 Cu-Cr-Zr, and modified electrode tips [9]. The inclusion of Cr and Zr reduces the electrical conductivity of electrodes and increases their strength. Cu-Cr and Cu-Cr-Zr

5

are suitable for steel welding. Apart from the conventional electrodes, some modified electrode caps have been investigated. Parker used a Cu-Al$_2$O$_3$ electrode to weld hot-dip galvanized steel, and the softening effect was alleviated on the Cu-Al$_2$O$_3$ electrode[5]. Zou coated Ni/(TiCP/Ni)/Ni layers on the electrode cap to avoid the reaction with Zn coating [10]. The formed layer separated the Zn from the Cu substrate, and small welding current was used due to increased the contact resistivity.

2.2 Welding parameter

An RSW process comprises a few welding parameters to produce nuggets with sufficient strengths. Depending on the physical properties of the base metal, the welding parameter might vary quite significantly. Also, different types of welder also have a pronounced influence on the value of the welding parameters.

2.2.1 Welding current

A number of power sources are available, including a single-phase AC welder, condensator discharge (DC) welder, medium frequency direct current (MFDC) welder and three-phase DC welder. Their representative current waveforms are presented in Figure 2.1. Different manners of nugget development have been identified using various power sources, and the MFDC welder allows a wider range of welding current in steel welding [11]. It is clear that the welding current processes sinusoidally and the nugget then grows periodically at the AC power frequency. On the other hand, the nugget under MFDC grows constantly without any oscillation in the volume of fusion zone. As suggested in Equation (1.1), the magnitude of the welding current is proportional to the amount of heat generated in the welding stage. Low welding current tends to cause cold weld or stick weld, whereas an excessive welding current can cause severe expulsion during the welding stage. Expulsion not only results in expelled metal from the fusion zone but also introduces an overheated region on the electrode tip. Such high

6

temperature on the electrode is found to be responsible for the rapid reduction in microhardness due to recrystallization.
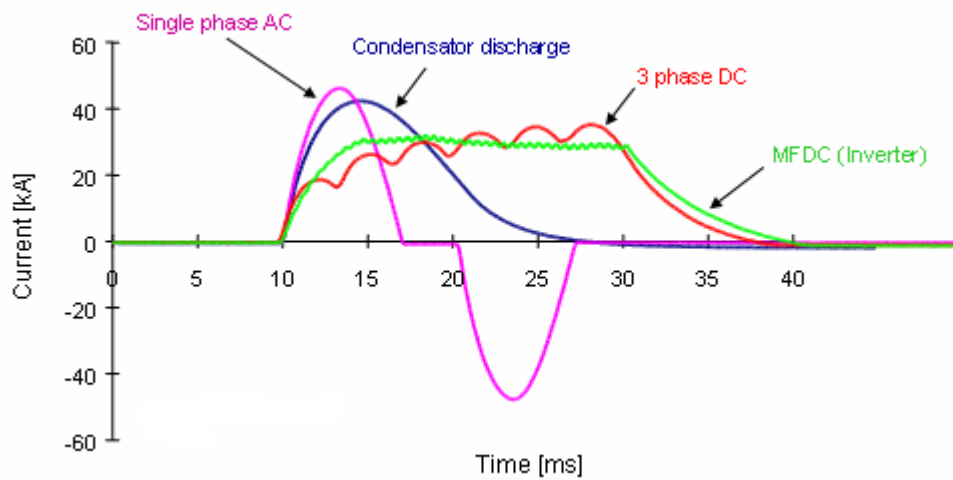
Figure 2.1 Schematic diagram of current waveforms from different power sources [12]

Furthermore, depending on the characteristics of the base metal, the welding current can vary dramatically. Zinc coatings, including galvanized and galannnealed, are recommended for steel to improve corrosion resistance. Coating in sheet metal reduces the electrical resistance at the contact region [13]. Compared to bare steel, higher welding current is required, due to the low contact resistance of the zinc coating. A number of studies have found that an increase in welding current was needed to produce a satisfactory spot weld when welding zinc coated steel [14-16]. Usually, $8 - 10$ kA of welding current can produce a good quality weld in steel strips [17, 18].

2.2.2 Welding time

As one of the essential components in Joule's law, welding time is considered an important factor in heat generation. The length of welding time is also influenced by the physical properties of the base metal. A long welding time is implemented for AHSS steel and stainless steel, whereas a short welding time is utilized for lightweight Al and

7

Mg alloys where the thermal conductivity is much greater. To achieve a good tensile shear strength of the joint, the welding time needs to be chosen wisely. A proper welding time can produce a joint that fails in pull-out mode; insufficient welding time delivers an undersized weld that fails in interfacial shear mode, which is not acceptable based on the industry standard [19, 20] Moshayedi investigated the effect of welding time on residual stress using a 2D axisymmetric finite element model [21]. The welding time was found to play a much more crucial role than the welding currenin determining the radial residual stress near the fusion zone.

2.2.3 Electrode force

During the RSW process, electrode force is exerted on the base metals. The electrodes firmly compress the base metals to ensure passage of the welding current. In addition, electrode force affects the contact resistance at the faying surface and the resistance to the expulsion. The electrode force was found to be inversely proportional to the nugget diameter, as investigated in the numerical simulations in Figure 2.2. The simulated results revealed the temperature distribution in the fusion zone, where the area of fusion zone declined under high electrode force. It was clear that the contact resistance was sensitive to the electrode force applied [Ref. 22].
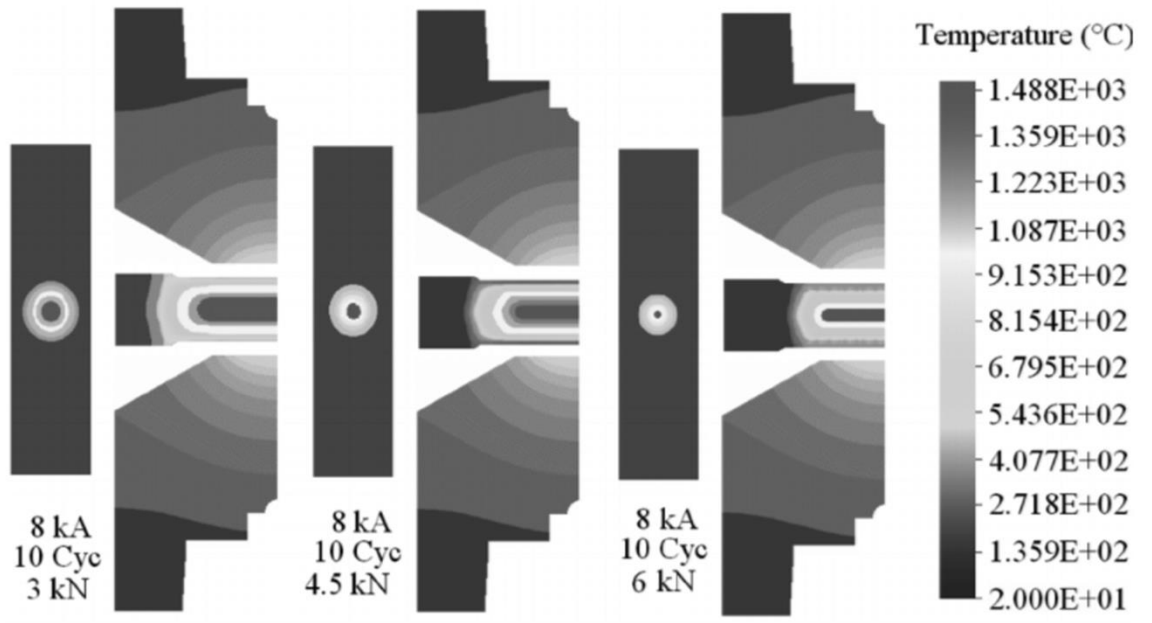
Figure 2.2 The influence of electrode force on nugget development via numerical simulation [22]

To further comprehend the relationship between the electrode force and contact resistance, Badu derived a semi-empirical model of the contact pressure and contact resistance per unit area in steel [23]. The inversely proportional function was validated via theoretical fitting and measurement as presented schematically in Figure 2.3. A high electrode force was found to substantially reduce the contact resistance per unit area.
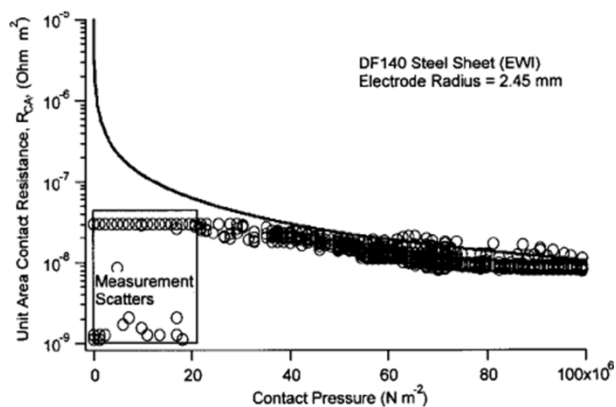
Figure 2.3 Contact resistance at different electrode forces[23]

Furthermore, the expulsion is strongly related to the value of the electrode force. Excessive electrode force have been found to induce surface expulsion and delay the initial melting point, certainly affecting the weld quality as small nugget and deep indentation mark were derived [24]. Moreover, a number of experimental studies have been carried out to investigate the relationship between the expulsion and electrode force [25-28]. Senkara also presented the schematic illustration of expulsion shown in Figure 2.4, where F_N is the total force from the liquid nugget, F_E is the total external force [29]. As a result, a minimal electrode force cannot suppress the internal force in the liquid nugget, and the expulsion at the faying surface is likely to occur. The external force F_E is considerably affected by the process condition (to be further elaborated in subsequent sections). Moreover, the internal force F_N is regarded as a function of heat generation. Thus, it is related to the welding parameters and the physical properties of the base metals.
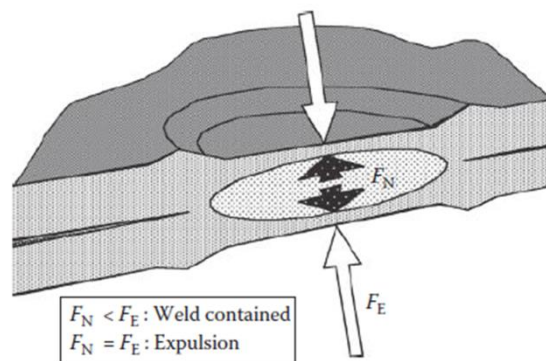
Figure 2.4 Schematic diagram of expulsion model [29]

2.2.4 Weldability lobe

Welding current, welding time and electrode forces are the most important factors in a RSW process. A weldability lobe, including these parameters, has been developed to

suggest viable combination of the welding parameters for making a nugget of acceptable size.
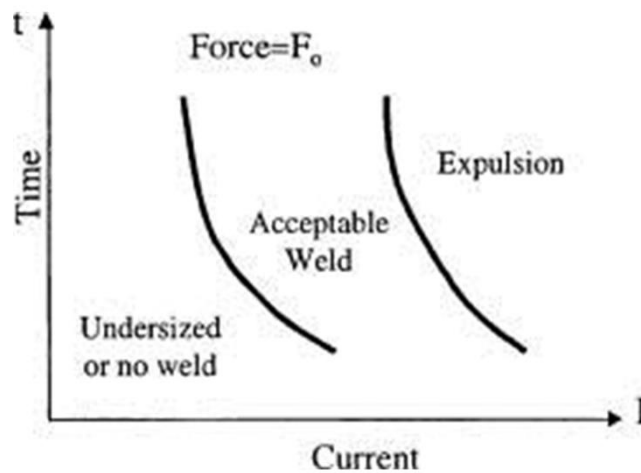
Figure 2.5 A typical weldability lobe [30]

A typical weldability lobe for mild steel is presented in Figure 2.5. Because three parameters are included in the weldability lobe, the user sets the electrode force as a constant (F_0) and varies the value of welding current and welding time. Two limits and three regions are observed in Figure 2.5. When the heat input is below the lower limit, the heat can partially melt the metals at the faying surface and will deliver undersized or no welds. In contrast, excessive heat above the upper limit produces much greater thermal expansion stress so that expulsion is likely to occur. The weldability lobe gives insight intowelding parameters in commercial use, where viable combinations can be found between the upper and lower limits. When electrode degradation becomes a major concern in the plant environment, the values should be as close as possible to the upper limit. Besides, many factors affect the shape of the weldability lobe, including the power source of the welder [31], the chemical composition of the base metals [32, 33], the coating type and weight [34-36], electrode misalignment and air-gap in the sheet metals. Figure 2.6 compares weldability lobes under a single-phase AC and MFDC

11

power source. It is seen that MFDC is capable of producing good welds over a larger range than that in the AC welder. With small current, the MFDC welder can still deliver welds of acceptable-size whereas the AC welder can produce undersized welds. The influence of the weight and type of coating on the weldability lobe is substantial, due to the changed contact resistivity on the zinc coating. The heat generated in the initial cycles is used for the melting zinc coating and breaking down the surface, after which the heat is used for the nugget nucleation and growth. The weldability lobe for a base metal with thicker zinc coating shifts to the right, as much more current intensity is required to melt zinc coating. Moreover, the contents of carbon and phosphorous have been identified as having substantial impact on the welding current in the weldability lobe [37]. High content of carbon and phosphorous would induce interfacial shear failure. Thus, the high welding current is not applicable for welding steels with high phosphorous. Titanium, as a precipitation hardening addition, has been found to reduce the nugget strength and the welding range by a noticeable margin [38]. Furthermore, boron alloyed steel is widely used due to its appealing strength-to-weight ratio. The content of boron affects the weldability and microhardness of the nugget [39]. Proper welding parameters should be used to avoid interfacial shear failure or the generation of internal cracks in the fusion zone.
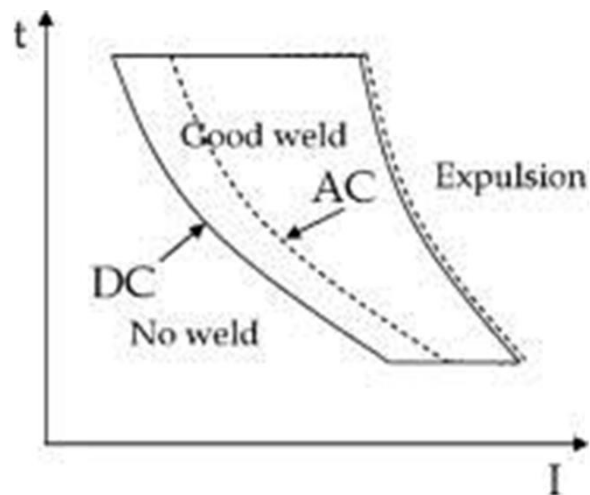
Figure 2.6 Weldability lobes under single-phase AC and MFDC source [31]

2.3 Monitoring weld quality in resistance spot welding

In the plant environment, a reliable and efficient quality monitoring system is desired. Achievement of a highly efficient and accurate online monitoring system is still a challenge to researchers and engineers. Unsatisfactory welds can be delivered in the production line under an improper combination of welding parameters. For instance, an undersized weld nugget with insufficient deformation-bearing capacity can lead to catastrophic structural failure. On the other hand, expulsion, described as the expelled molten metals at either the faying surface or the workpiece/electrode surface, undermines the joint strength due to the substantial deficiency of nugget volume, thus reducing the lifespan of electrodes due to ultrahigh temperature along with the electrode tip surface. Therefore, it is extremely important to maintain weld quality consistently throughout industrial production.

2.3.1 Destructive inspection

Destructive inspections, being performed on a one-sample basis off the production line, show appealing reliability for distinguishing unsatisfactory welds from welds with high quality. Common destructive inspections include the tensile shear test (TST), and the

13

cross tension test (CTT), as shown in Figure 2.7. Different failure mechanisms have been demonstrated in these tests. Pouranvari further discussed the stress distribution in the nugget subjecting to TST and CTT [40], as shown in Figure 2.8. CTT is modeled as a Mode I cracking condition, where the stress intensity condition is predominant. A joint susceptible to interfacial failure in CTT usually attains low fracture toughness, and an acceptable sized joint in pull-out failure has a low strength at the heat-affected zone (HAZ). In contrast, the failure mode in TST is greatly determined by the mechanical strength of the BM and the size of the fusion zone. The competition between the tensile stress along the loading direction and the compressive stress perpendicular to the loading direction decide the failure mode of the joint. CTT and TST have been reported to focus on different aspects of a joint's the mechanical properties [41].
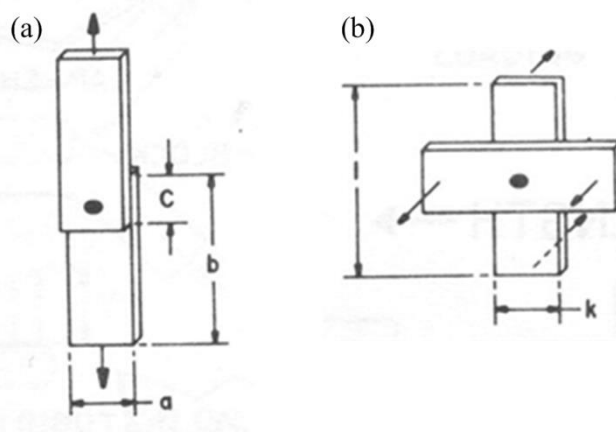
Figure 2.7 Typical destructive tests. (a) TST and (b) CTT [38]
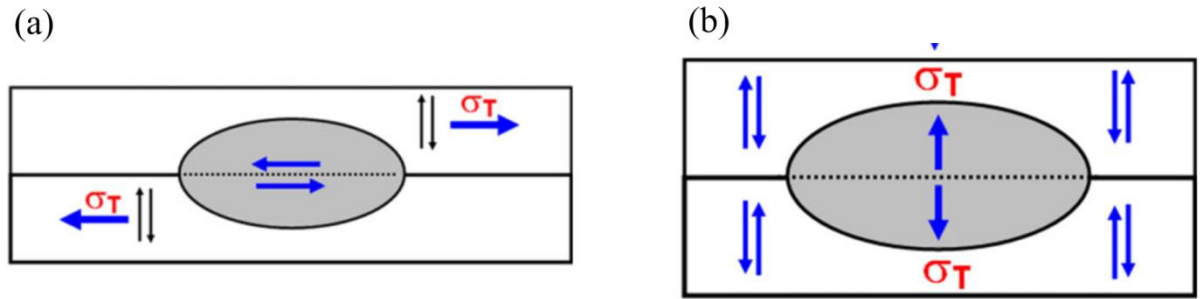
Figure 2.8 Stress distribution of the joint. (a) TST and (b) CTT [40]
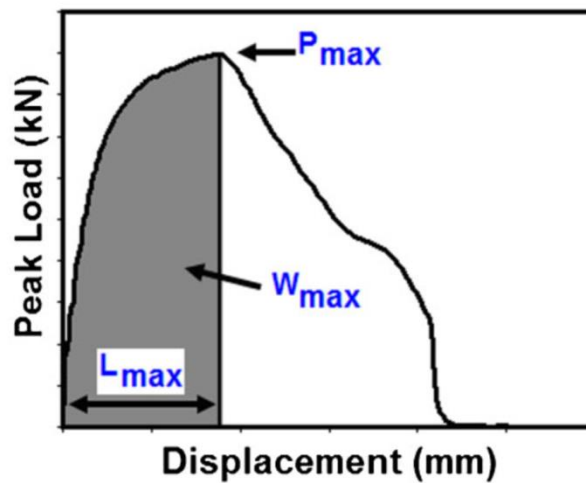
Figure 2.9 A typical load-displacement of mild steel in TST [40]

A typical load-displacement curve in TST is shown in Figure 2.9 [40]. The peak value (P_{max}) in the load-displacement curve indicates the tensile shear strength (TSS), an important measure of weld strength that indicates the quality of the weld. The area under the load-displacement curve also gives insight into the energy-bearing capacity of the joint, as suggested by Pouranvani [40]. However, factors including the cost of implementation, the usage of material, and low productivity prevent the extensive employment of destructive inspections in the plant environment.

2.3.2 Non-destructive inspection

Non-destructive methods utilized a number of process signatures in evaluating weld quality. For this purpose, an off-line signal, ultrasonic waveform, and on-line signals such as mechanical and electrical signals have been sampled and processed. Because the components of these signals vary in relation to the nucleation and development of nuggets, they can be used to distinguish undersized welds and expulsions from acceptable sized welds.

2.3.2.1 Ultrasonic waveform

Ultrasonic waveform, an off-line signal, is employed to determine the final nugget diameter, as demonstrated in Figure 2.10. The nugget diameter and the relative height and sequence of echoes are strongly closely related, shown in Figure 2.11, though little information about nugget development history has been provided [42, 43]. Moreover, the reported patterns for welds with severe misalignment have not revealed the true nugget diameter, as the echoes could not be received due to deformation of the sheet [44]. Though it is extensively used in the plant environment, the ultrasonic waveform is not the focus of this work.
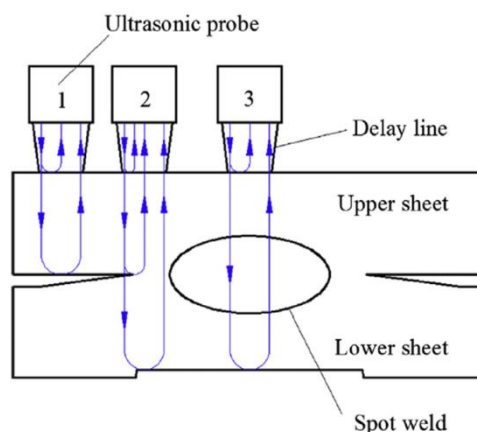
Figure 2.10 Schematic diagram of an ultrasonic scan on a spot weld [45]
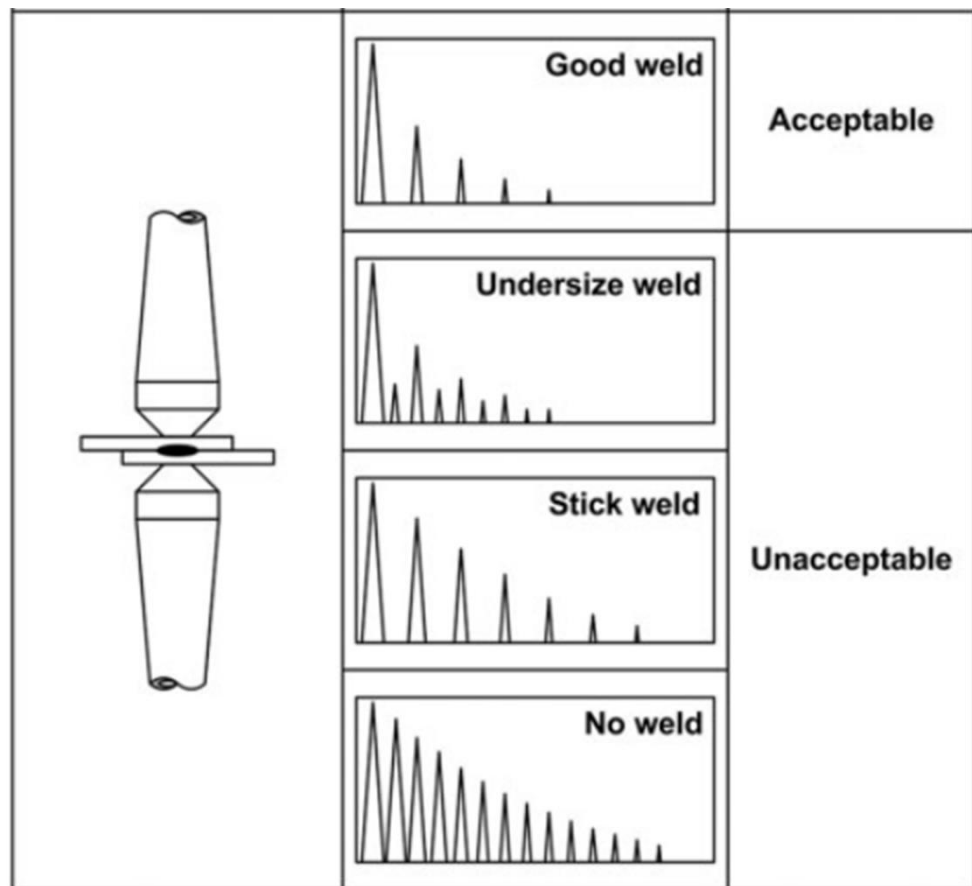
Figure 2.11 Weld qualities and their associated ultrasonic C-scan waveforms [43]

2.3.2.2 Electrode displacement

Electrode displacement (ED) is generated as the electrodes move away from base metal under the thermal expansion of the sheets and solid-to-liquid phase transformation. ED is determined by a range of factors, such as the RSW power source [31], surface condition[46], welding parameters [47], and electrode shape [48]. ED curves have been collected via the techniques of image processing [49-51], non-contact type laser triangulation sensor [52-55] and contact-type displacement sensor [56, 57], as shown in Figure 2.12.
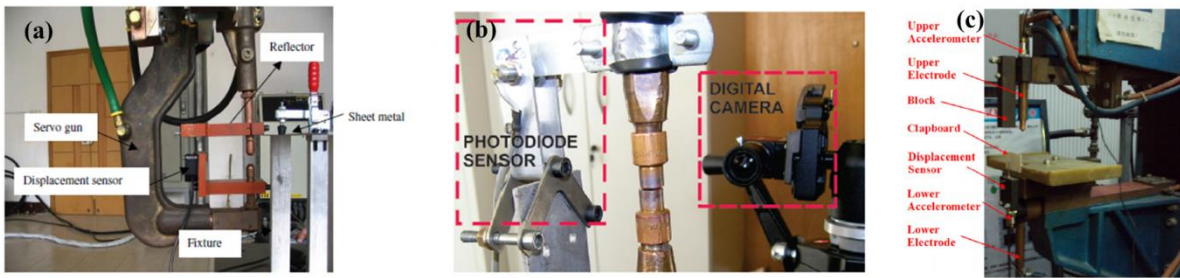
Figure 2.12 Electrode displacement set-up in existing work. (a) Laser triangulation sensor [52]. (b) CCD camera [51], and (c) LVDT displacement sensor [58].

Jou revealed that ED values are strongly related to the thermal expansion of the sheets, thus are tuned by welding parameters, such as welding current, welding time, and electrode force [47]. Typical ED curves are shown in Figure 2.13. The ED curve values vary significantly based on the volume of the fusion zone. When no weld or an undersized weld is formed, the ED curve yields a small peak value. The peak value of the ED is constrained by the dimension of the electrode, and excessive heat input leads to a flat platform after the peak value. If the electrode force is too small to contain the molten metal, the liquid metal expels from the faying surface, resulting in a noticeable drop in the ED curve in case D.
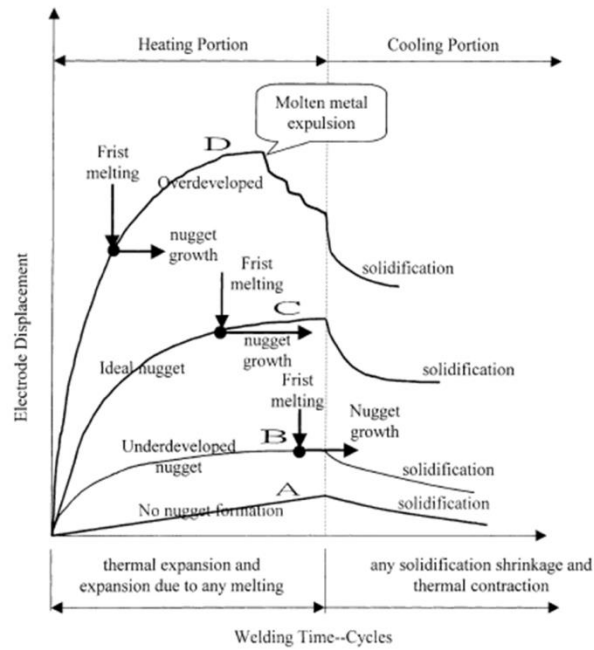
Figure 2.13 Electrode displacement curves of different weld qualities [47]

Furthermore, Kuščer suggested that conventional methods of ED measurement fail to consider the contribution of the copper electrode to the total thermal expansion, as the measurement based on image processing yields a lower value than those from displacement sensors [59]. Furthermore, the constraints related to the cost of achieving high precision of displacement sensor make ED sampling only favorable in the laboratory environment, rather than the plant environment. If mount the electrode displacement was mounted on a C-type or X-type gun, the short working distance could limit the collection of ED signals.

2.3.2.3 Dynamic resistance

Dynamic resistance (DR), an electrical signal, is frequently used in the plant environment. Gedeon et al. highlighted that the ease of installation and process and the low cost of measurement allow this signature to be widely adopted in the production environment [60]. With the simutaneous collection of voltage and current signals during

the welding phase, DR curves can be derived from these signals at different stages that involve pronounced physical phenomena. Dickinson discussed the physical phenonmena in the DR curve of steel, shown in Figure 2.14 [38]. For steel, the DR can be divided into the stages of surface breakdown, asperity collapse, nugget nucleation, nugget development and expulsion if the electrode force cannot outperform the thermal stress of the molten metal. Dynamic resistance is the sum of contact resistance at different surfaces and bulk resistance of the base metals. The contact resistance gradually decreases with time whereas the resistivity of steel increases proportionally with the increase of temperature. Because the resistivity of both Al and Mg is much lower than that of steel, theor DR curves show many fewer characteristics, as they gradually decline with welding time. Apart from relating to the welding parameters, the DR signal has been identified as a function of the electrode tip diameter, as shown in Fan's work [61], making DR signal useful in understanding electrode wear.
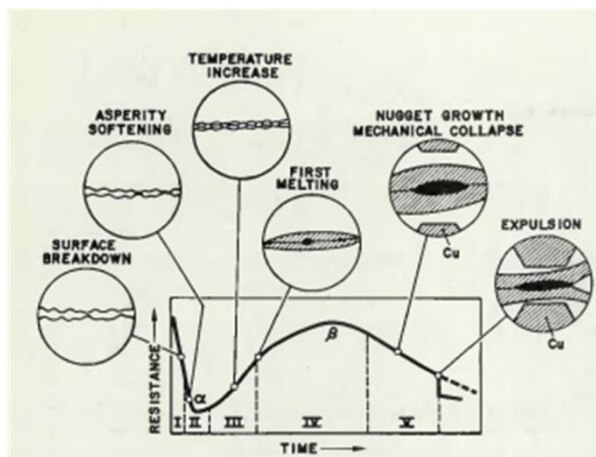
Figure 2.14 Typical Stages of DR curve in steel [38]

Gedeon suggested that DR can be calculated in different methods under AC power sources, including the root-mean-square (RMS) method and the peak value method for every half cycle [60]. The DR curve with more data points can be calculated when the inductance L in the secondary circuit is known. Resulting DR values are calculated via:

20

$$V = IR + L \cdot dI / dt \tag{2.1}$$

where the inductance L is calculated at the peak point of the current with zero gradients (dI/dt=0). Luo also presented DR curves with all sampling points in the welding stage via:

$$R(t) = \frac{U(t)}{i(t)} \tag{2.2}$$

where $U(i)$ and $i(t)$ are welding voltage and welding current, respectively. Furthermore, Zhou derived an analytical equation Equation (2.3) in determining the DR R_{RMS} with high resolution [62]; however, to implement this method, inductive voltage needs to be eliminated from the electrical potential.

$$R(i) = \begin{cases} R(i) & if\ i=1 \\ R(i) & if\ i=2\ and\ R(i) > 0.5(R(i+1)+R(i-1)) \\ 0.5(R(i+1)+R(i-1)) & if\ i=2\ and\ R(i) < 0.5(R(i+1)+R(i-1)) \\ R(i) & if\ i \geq 3\ and\ R(i) > 0.25(R(i+2)+R(i+1)+R(i-1)+R(i-2)) \\ 0.25(R(i+2)+R(i+1)+R(i-1)+R(i-2)) & if\ i \geq 3\ and\ R(i) < 0.25(R(i+2)+R(i+1)+R(i-1)+R(i-2)) \end{cases}$$

$$\tag{2.3}$$

On the other hand, DR of a MFDC welder have been calculated via Ohms law, suggested by Zhao [63] and Wen [64]. The DR curves differentiated weld qualities based on the appearance of the profile. The mean values of the DR curves, varied by welding current and welding force, indicate whether an adequate nugget is formed [64]. Moreover, Fan demonstrated the application of DR curves in expulsion detection under various circumstances [65]. A sudden decline in the DR curves, associated with ejection of molten metal, could indicate the presence of expulsion.

2.3.2.4 Electrode force

Electrode force, similar to ED, responds to nugget growth and development. The features of electrode force are affected by welding parameters (welding current and electrode force), welding machine characteristics (stiffness of the welding arm) and sheet materials (thickness and physical properties) [66, 67]. Electrode force is captured via strain measurement, force measurement on the welding clamps and force sensor integrated on the drive motor.

Electrode force has been proposed for monitoring the weld quality of Al alloy on the MFDC servo gun. The DR signal of Al alloy does not exhibit many key features, and installation of a laser displacement sensor is difficult in the plant environment. Ji compared the electrode force and ED at different welding parameters during welding of an Al alloy [57], as shown in Figure 2.15. The change in welding current affected the values of the electrode force curves, similar to the ED curves. A large oscillation could be seen in the values of the electrode force curve, when the thermal expansion force was varied against the temperature. Excessive welding current led to expulsion at the faying surface, and a noticeable drop was seen in the ED curves. An undersized weld resulted in a gradual increase in the values of the electrode force. An acceptable sized nugget was found to deliver a gradual increase in the values of the ED curves, with a slight decline following after the peak point. The change in welding time affected the length of the ED curves, and a prolonged welding session (11 cycles) could result in expulsion.
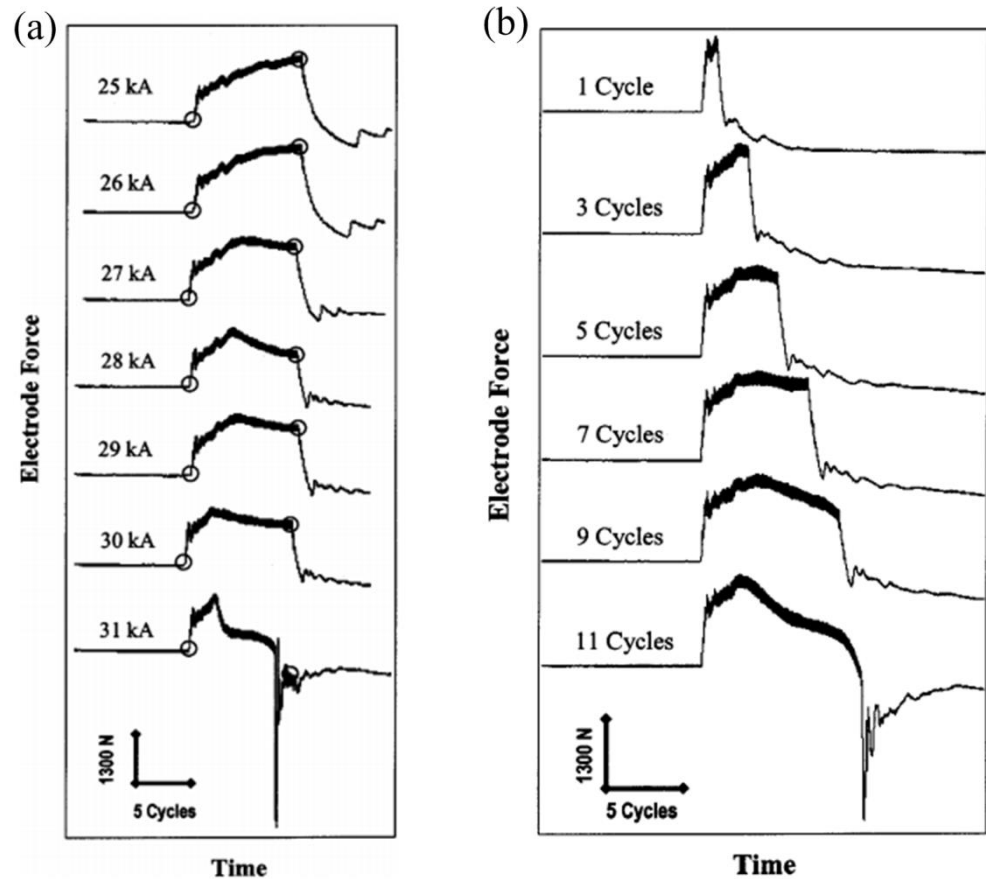
Figure 2.15 Electrode force curves during welding with Al sheets. (a) varied welding currents. (b) varied welding time [57]

2.3.2.5 Electrode vibration

Electrode displacement curve experiences strong oscillation in the welding stage due to the fluctuation in temperature of the nugget and associated thermal expansion. Signal processing is usually implemented to eliminate the vibrating component of the curve. Wang applied a bandpass filter to the original electrode displacement signal of 1mm low carbon steel and identified that electrode vibration was also strongly related to the nugget development, when [58]. The outline of the filtered signal implied the physical meaning of the nugget development, and the influences of welding current on electrode vibration are revealed in Figure 2.16. Moreover, the fluctuation characteristic of the electrode could be further investigated via each half cycle of the welder [68]. The fluctuation peak was found to monitor the different weld qualities.

23
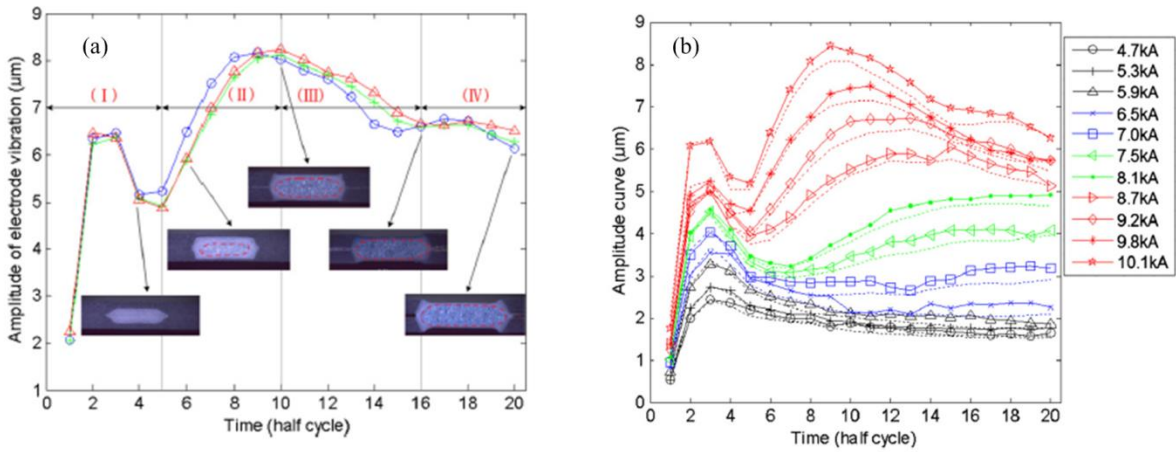
Figure 2.16 (a) Electrode vibration at different stages of nugget development of low carbon steel. (b) the influence of welding current on electrode vibration [58]

2.3.2.6 Indentation mark

The indentation mark also provides useful information on the weld quality, that can be evaluated via ED curve, servo gun or image processing [52, 69]. The ED curve provides a history of the relative position of the sheets in the welding stage and the hold stage. The difference between the starting and endpoint values of the ED curve was found to closely relate to the actual indentation depth measured via servo gun. Most of the outliers of indentation depth in Figure 2.17 were found to yield poor weld strength, which can be considered as a weld evaluation tool in the plant environment.
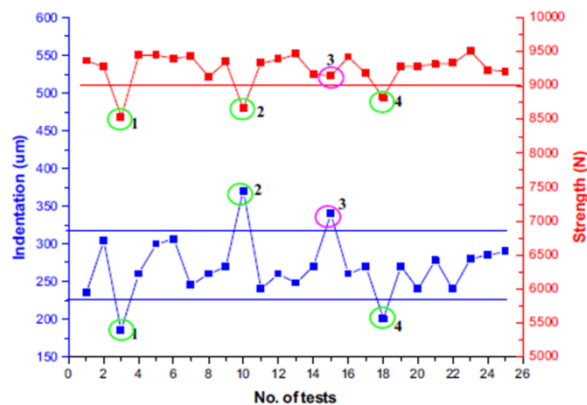
Figure 2.17 Online weld quality inspection using indentation depth [52]

On the other hand, image processing of the indentation marks was carried out by Ruisz to detect the effective heating area in the nugget [69]. The expulsion and poor quality welds were evaluated accordingly.

2.3.3 Characterization of dynamic signals

The characteristics of dynamic signals correspond to the heat generation in the welding stage and the electrode force exerted on the sheet metals. Expulsion or undersized nuggets cause the dynamic signals to change dramatically. Researchers have utilized a number of methods to characterize the dynamic signals, including a statistical approach [64, 70-72], moving range (MR) chart [73], principal component analysis (PCA) [18, 74, 75], radar chart [76] and pattern recognition [77]. Statistical methods include the individual point value, mean value, standard derivation value andslope between two points. The selection of statistical values requires a comprehensive understanding of the nugget development. For instance, the DR curves of mild steel have a trough α and a peak β, associated with the breakdown of contact asperity and with nugget nucleation. The endpoint value in DR curves provides a good indication if expulsion occurs, as the loss of molten metal substantially reduces electrical resistance. Furthermore, the thermal expansion of sheets accounts for the electrode displacement; thus, the peak of the ED curve is related to the total thermal expansion and heat generation.

MR charting is used to monitor high-frequency characteristics of RSW. The method properly evaluates the process stability of the curve. Any abnormal condition in a specific time frame is found to be out of bounds of the MR. PCA involves transformation from a range of possibly correlated variables in the time domain to an array of linearly uncorrelated variables. A radar chart converts the values from the time domain to a new domain, in which the area, gravity, girth and maximum value of the radar chart can be further evaluated. The graphical pattern recongition method,

converted from a bi-polarized pattern vector, is similar to the statistical method, in which a number of crucial profile features are extracted from the dynamic signal. Based on the patterns, a few classification can be made.

2.4 Welding process conditions

Though the weldability lobe may be determined for a particular material and accessed from the material handbook and peers' work, many process factors affect the weld quality in the plant environment, such as electrode degradation, electrode misalignment, shunting, poor fit-up problem and closed edge welds. Undersized welds and expulsion are likely to occur if these factors are not well addressed in the plant environment.

2.4.1 Electrode degradation

In the lab environment, electrodes used for the experiments can be easily dressed, and the use of a new pair of electrodes is suggested for every new group. In contrast, electrodes assembled for BIW manufacturing need to make many more spot welds than their counterparts in the lab. The types of coating and the properties of the BM have pronounced influences on the electrode life. Willams found that the electrode lives for welding bare steel and hot-dip zinc coated steels reached ~ 5000 and ~ 1500 welds, respectively; in addition, galvannealed (Fe-Zn) steel allowed longer electrode life of ~ 2000 welds, but Zn-Al coating reduced the electrode life to ~ 500 welds [78].

Mechanical deformation and chemical alloying are the two major factors in deterioration of electrode performance in the RSW. The former factor causes expansion in the contact area and mushrooming of the electrode tip, as illustrated in Figure 2.18, especially in electrodes during welding with steel; as a result of electrode mushrooming, the current intensity declines and an undersized button is produced [79]. On the other hand, the latter factor involves intermetallic compound (IMC) formation between the

26

copper element in the electrode and the elements distributed at the surface of the base metals, as shown in Figure 2.19. The brittle alloy products are picked up during the continuous welding session, leading to electrode pitting.
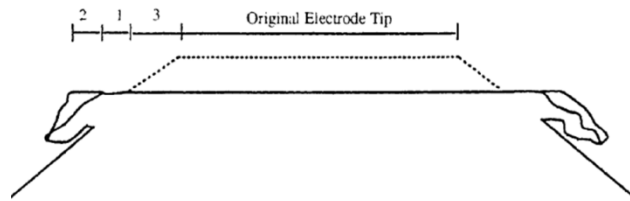
Figure 2.18 Schematic diagram of electrode mushrooming [5]
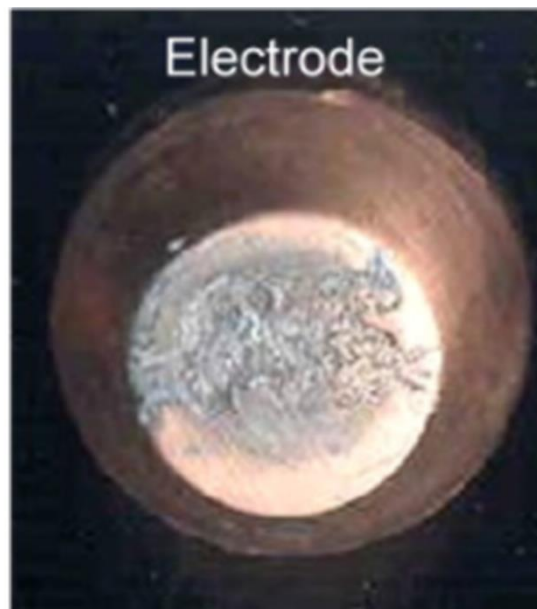
Figure 2.19 Alloy reaction on the electrode [80]

2.4.1.1 Electrode softening

Mechanical deformation of electrodes results mainly from softening of the electrode, primarily attributable to the high temperature along the electrode tip. Welding parameters, such as welding time, welding current and electrode force contribute to heat generation in the fusion zone, according to Equation (1.1). Because the contact resistance at the faying surface outperforms other contact and bulk resistance as seen in

Figure 1.2, a significant proportion of the heat is generated at the faying surface. Nevertheless, the proportion of heat generated from the electrode-workpiece surface is not negligible, implying that sufficient temperature is generated at the electrode tip surface during the welding stage. Simulation [1, 81-85], empirical [86] and experimental works [87-89] have been devoted to determining the temperature distribution along the electrode tip surface. The welding parameters and the electrical resistivities of the base metals are found to affect the peak temperature in the electrode tips. The geometry of the electrode can also deliver different temperature fields, such that electrodes with small tip diameter yield high peak temperature and round sided electrodes yield lower temperature than tapered electrodes [1]. A larger taper angle allows a longer electrode life, as verified in Zn-coated steel at different thicknesses shown in Figure 2.20.
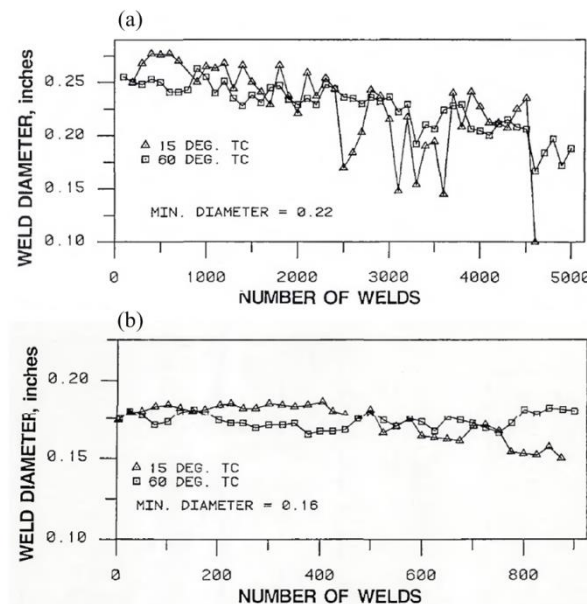
Figure 2.20 Electrode life at different taper angles (a) 1.27 mm GA steel. (b) 0.8 mm galvanized steel [1]

Gauthier used an electrical-mechanical-thermal model to analyze the temperature field distribution along with the number of welds [85]. The temperature simulated along the electrode tip showed good agreement with the measured values, in which both

temperatures exceeded the softening temperature of copper (480 °C). When the welding current is removed, the heat in the fusion zone is dissipated away from the water channel in the electrodes. Such heating and cooling cycles in the electrode tip gradually soften electrodes. Deformation (mushrooming) of the electrodes is believed to be a response to the electrode softening effects.

From previous work, recovery process and recrystallization process have been nominated as primary mechanisms of the electrode softening. The recovery process was suggested to reduce the microhardness of electrodes by Parker, when the dislocation, jog, and defect generated at the manufacturing stage of the electrode were annihilated under the temperature in RSW [5]. No apparent evolution in grain structure appeared in Figure 2.21 (a), and only a few recrystallization regions in Figure 2.21 (b) were believed to occur under the localized heat.
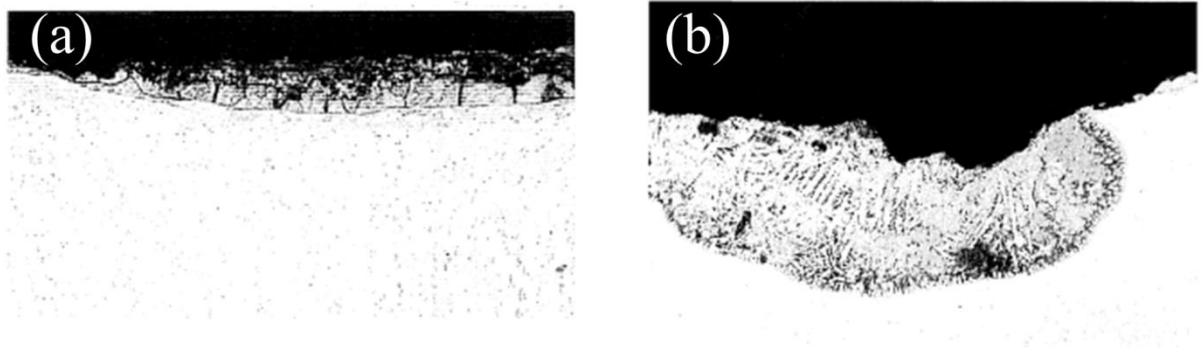
Figure 2.21 (a) Electrode tip after 2000 welds with galvanized steel. (b) recrystallisation grains in the localized region. [5]

On the other hand, the recrystallization process has been investigated in a wider range of studies of electrode degradation [86, 90-93]. It involves apparent changes in the grain size underneath the electrode tip surface and a considerable reduction in hardness. Zhao used Ni-Cr alloy and Ni-Cu alloy insert strips in small-scale RSW of zinc-coated steel [93]. Recrystallization layers of different thickness were found, and a distinct difference

between the original structure and the recrystallized grain was identified, as in Figure 2.22. The copper strip was found to have the thickest layer of the recrystallized structure and the 304 stainless steel strip had the thinnest recrystallized layer, suggesting that the electrode softening was alleviated by a stainless steel strip.
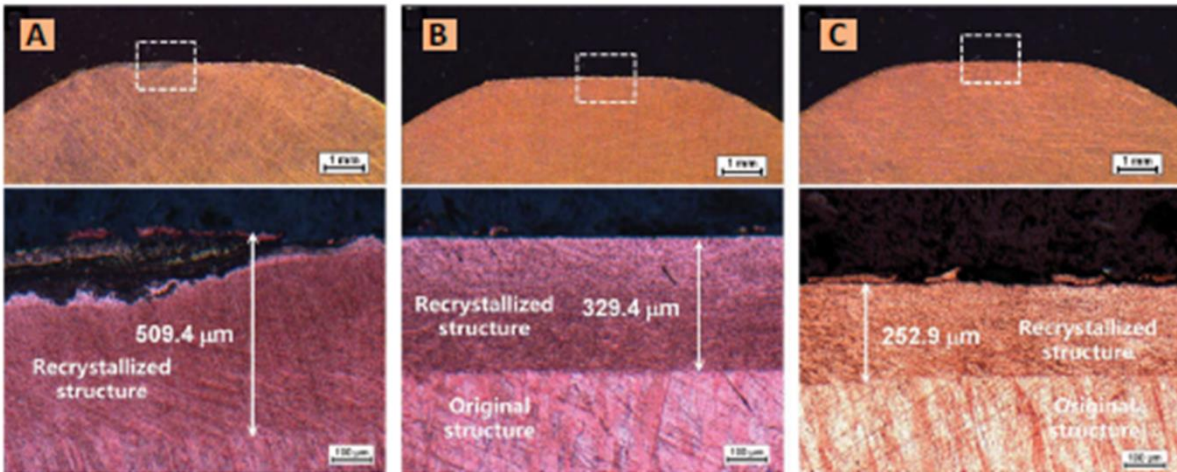
Figure 2.22 Recrystallization region in the electrodes welded with 0.1-mm inserted strips after 600 welds. (a) copper strip. (b) CuNi18Zn20 strip. (c) 304 stainless steel strip. [93]

2.4.1.2 Chemical alloying

Intermetallic compound formation is likely to occur at the electrode tip surface when welding zinc-coated steels and aluminium alloys. Dilthey presented three mechanisms for IMC transfer between electrode and base metal: (1) the local bond, formed directly between the electrode and BM, is transferred from the electrode surface and accumulated on the base metal; (2) the resulting IMC transfers from the BM to the electrode substrate; and (3) the IMC breaks internally and adheres to the electrode and BM [94]. Because the temperature is the highest at the center of the tip surface [85], the pitting initiates at the center of the electrode and expadns continuously in the axial direction. Wang used FE models to validates the adverse impact of a ring-shape

morphology on worn electrodes [79]. The pitting in the center reduced the current intensity at the faying surface, causing insufficient heat to the base metals at the center and generation of the void in the nugget. Because the voids at the center line in the fusion zone were found to affect the failure mode in the tensile shear test [17], undersized welds were likely to be delivered when the pitting diameter was large enough. Depending on the type of coating or the compositions of the base metals, the IMC products formed varied dramatically.

Figure 2.23 demonstrates the development of alloy products during welding of galvanized steel. The zinc element from the substrate coating reacted with the copper from the electrodes and formed beta brass even after severval welds [5]. The final alloy product included an outer layer, gamma brass and beta brass, as the content of Zn diffused in the depth direction.
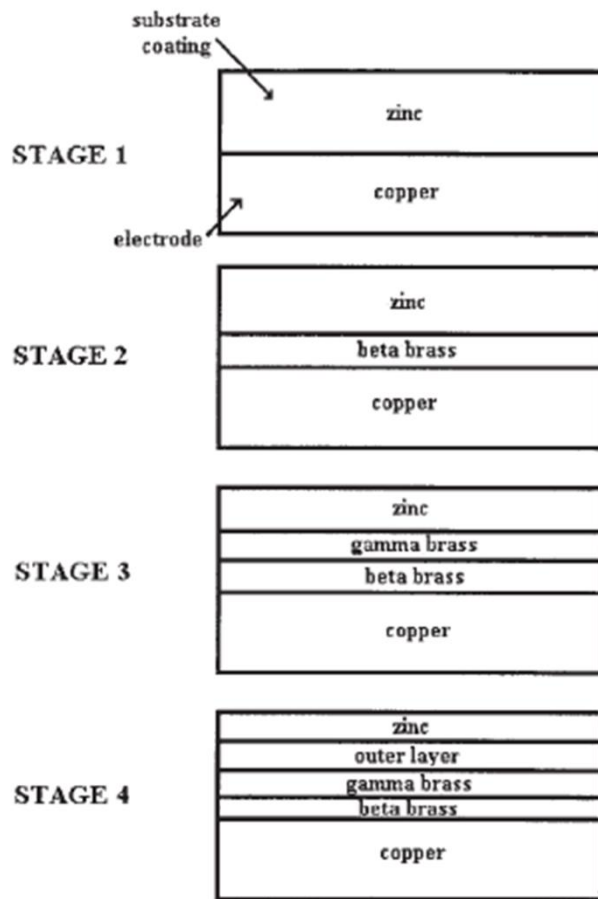
Figure 2.23 Schematic illustration of alloy formation during welding of galvanized steel

[5]

In contrast, galvannealed steel can result in a Fe-Zn-Cu rich IMC layer on the worn electrode, according to Hu [95]. Three types of galvannealed coating that differed in Fe-Zn phases examined under electrode life studies are illustrated in Figure 2.24. η, ζ, and δ Fe-Zn phases were found in the outermost regions of the coating in the three tested electrodes, respectively. δ Fe-Zn was found to be accumulated in the outermost layer at the electrode tip surface, which was further considered to be a physical barrier preventing the diffusion of Zn into the copper matrix. However, η and ζ Fe-Zn did not form uniformly along the tip surface and, in turn, protect the copper matrix from alloying reaction. Kondo investigated the electrode wear in alternative RSW of GA steel

and bare steel [87]. The FeZn phase was picked up by the bare steel, resulting in a much-reduced electrode life compared to that in the welding of GA steel.

	#1	#2				#3		
	A	A	B	A	B	C	D	E
Fe	0.3	0.5	71.3	0.6	5.4	23.0	34.6	55.1
Cu	81.3	51.1	5.9	31.3	22.6	5.9	0	0
Zn	18.4	48.4	39.0	68.1	72.0	71.1	65.4	44.9
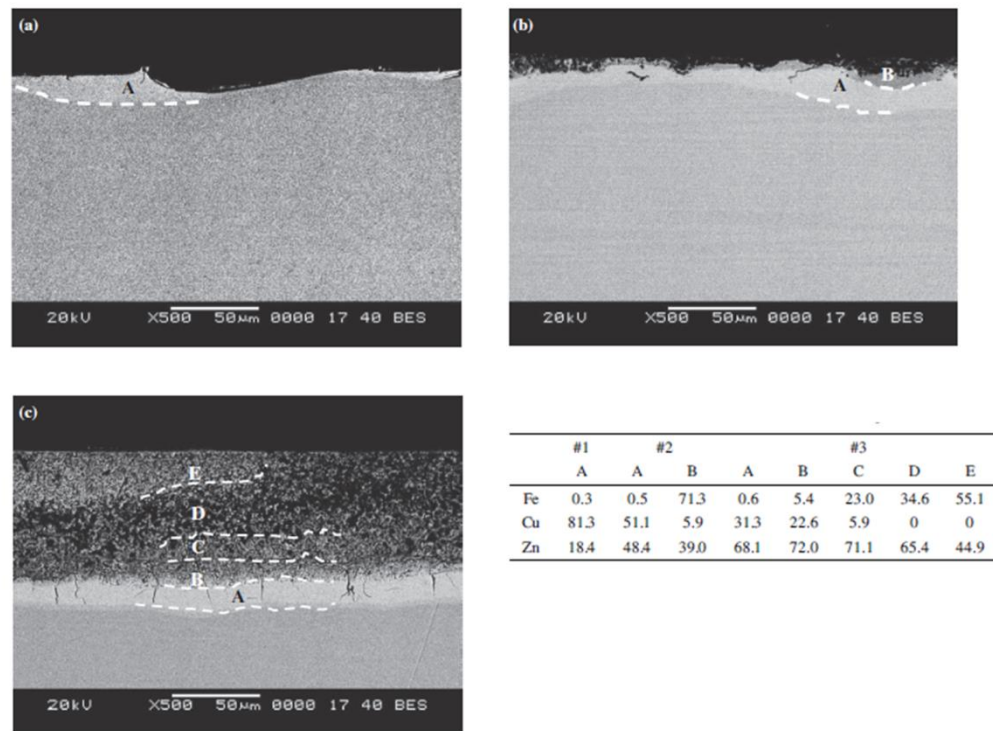
Figure 2.24 SEM images of the worn electrodes welded with GA steels [95]

Some researchers have introduced modified coated electrodes to prolong electrode life when welding zinc-coated steels. For instance, a Ni/(TiC$_P$/Ni)/Ni layer was used by Zou in coating copper electrode, and an alloying formation with molten zinc was substantially lessened [10]. Chen also investigated a number of Ni-based coated electrode and their tip diameter expansion rate is demonstrated in Figure 2.25, suggesting that the Ni/(TiCP/Ni)/Ni was suitable for welding Zn-coated steel whereas the TiC$_P$/Ni laser treated electrode worsened the mushrooming [96]. A modified electrode cap designed by Mazur also indicated that smooth surface quality could reduce localized heating and extend the electrode life [97].
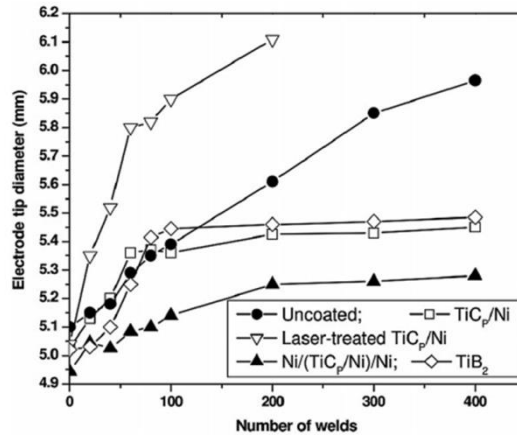
Figure 2.25 Growth of modified electrode tip [96]

Zhao introduced inserted strips in welding ultrathin steel sheets [93]. The strips made of Ni-Cu alloy and Ni-Cr stainless steel were found to significantly reduce the diffusion distance of the Zn element. Ni and Cu elements are soluble in each other, and no intermediate phase is found between Cu-Fe. The presence of Fe and Ni significantly prevented the formation of brittle phase, amd could therefore be used to alleviate pitting in the electrode.

2.4.1.3 Monitoring electrode wear in RSW

Alloying formation and recrystallization occur for a short time in every weld, so that the alloying product accumulates on the electrode tip, and the tip grows in the axial direction. The appearance of the electrode is affected by pitting and mushrooming. As a result, the current intensity and the resulting nugget diameter change correspondingly. Imaging processing and dynamic signals have been used to characterize electrode wear. Image processing includes carbon imprints of the electrode [98] and outliers of the electrodes [99, 100]. Peng analyzed the carbon imprints of electrodes from the beginning to the end-of-life under AC and DC [98]. Three factors extracted from the carbon imprints welded with aluminum sheets described the electrode wear-out, namely relative radius, edge concentration and eccentricity, as shown in Figure 2.26. The

34

increment in the radial axis remained nearly the same under two different power sources, while the severe pitting in the center reduced the effective contact area in both electrodes.
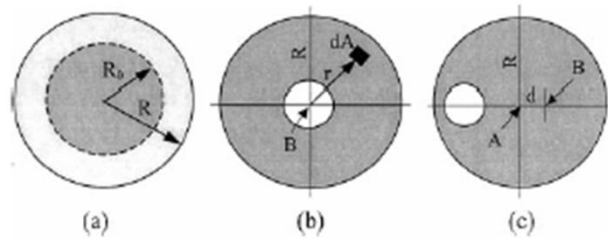
Figure 2.26 Features extracted from the carbon imprints of the worn electrodes. (a) relative radius. (b) edge concentration. (c) eccentricity. [98]

CCD camera captured the outline of the worn electrode from the side view, as shown in Figure 2.27 [99]. The electrode tip width T_p was found between new and worn electrodes, where it was obtained via active contour segregation and outline subtraction.
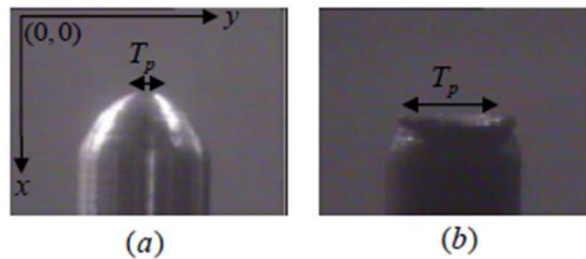
Figure 2.27 CCD side view of (a) new electrode and (b) worn electrode [99]

Electrode displacement, induced by thermal expansion of the sheets, was used by Wang to monitor electrode wear [73]. The signals collected from the worn electrodes were substantially lower than those from brand-new electrodes, as seen in Figure 2.2.28. The

welding current could be compensated based on the difference in the ED curves between the brand-new and worn electrodes, using a neuro-fuzzy inference system [54].
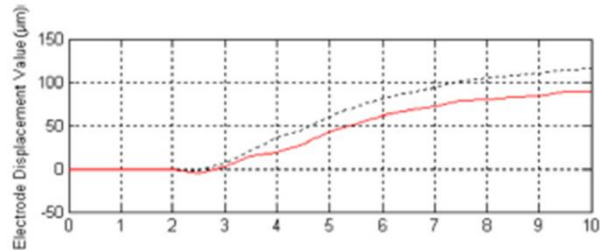
Figure 2.2.28 ED signals of the ideal electrode (black, dotted) and worn electrode (red) [54]

Lastly, the temperature of the electrode, measured by the thermocouple, has also been used to monitor the electrode wear in austenite steels [88]. The thermocouple was mounted at the end of the electrode, without interfering with the RSW process. The difference in temperature obtained from the brand-new electrode and worn electrode could easily be seen.

2.4.2 Electrode misalignment
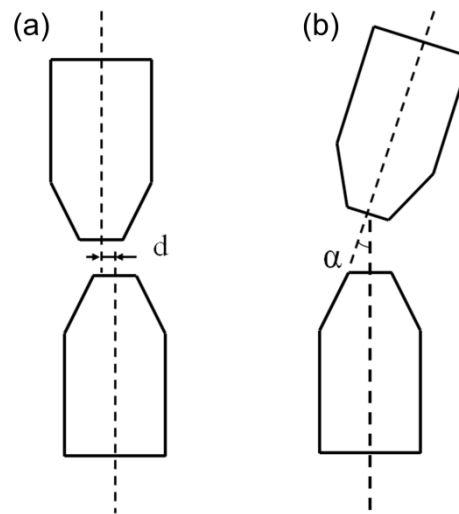
Figure 2.29 Schematic illustration of electrode misalignment. a) axial misalignment. b) angular misalignment.

Electrode misalignment has been found to substantially affect the welding quality in RSW. Such misalignment is primarily due to the flexibility of the welding machine arms for positioning the electrode. It can be divided into axial misalignment and angular misalignment, as shown in Figure 2.29. Rotation and off-centring of the electrodes can be found. Misalignment in electrodes results in a much narrower weldability lobe, as shown in Figure 2.30, and more heat is required to produce a nugget of adequate size [101, 102].
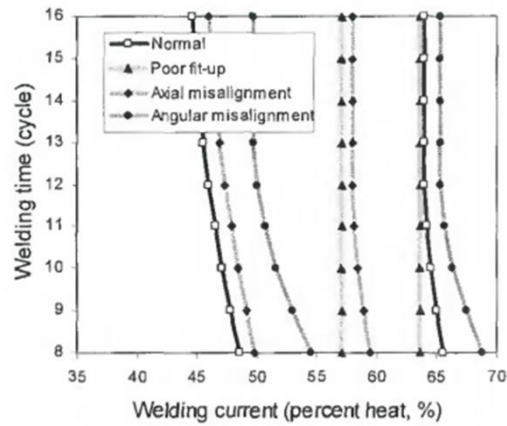
Figure 2.30 Weldability lobes under various abnormal process conditions [101]

Electrode force needs to be moderate to avoid producing expulsion or undersized welds. Expulsion was reported to have a high tendency to occur under angular misalignment [29]. According to ISO 18278-2, acceptable alignment can be identified based on the carbon imprint, where the difference in the horizontal length L1 and vertical L2 is less than 1 mm [103]. However, as indicated by Kim, even a tiny magnitude of misalignment can result in an uneven temperature profile [89] that could contribute to different behaviors in electrode degradation.

Since theoretical solutions are available only for a few problems with simple geometries and boundary conditions [104-109], developments of various numerical metohds [110-119] are important and critial for efficiently investigating welding behaviour including simulation of electrode misalignment. Nielsen conducted a three-dimensional numerical simulation of electrode misalignment [102]. Peak temperatures in the nugget under different misalignment conditions are shown in Figure 2.31. Asymmetric nuggets resulted from uneven heat generation; severe electrode indentation and sheet separation were seen with increased rotation angle. Nonetheless, the joint strength was not

considerably reduced by the electrode misalignment, as validated via numerical simulations and experiments.
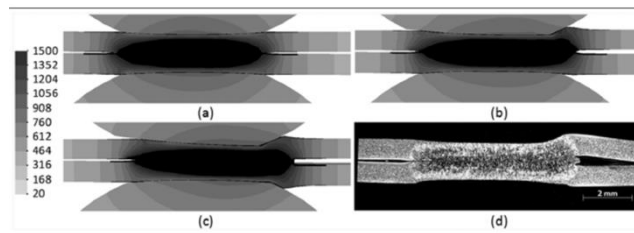
Figure 2.31 Peak temperature in nugget from simulation. (a) ideal electrode. (b) 2 °rotation in upper electrode. (c) 4 ° rotation in upper electrode. (d) experimental result [102]

2.4.3 Shunting effect

In the manufacturing of the BIW structure, many spot welds are continuously produced within the same region of a component, as shown in Figure 2.32, where the problem of shunting is inevitable

Figure 2.32 Multiple welds in the same part

Figure 2.33 demonstrates the fundamental principle of single shunting. As a parallel electrical path from the existing weld (shunt weld) is formed, the welding current flowing to the new weld (shunted weld) is reduced. Insufficient heat generation caused by the shunting influences the strength and nugget diameter of the shunted weld.
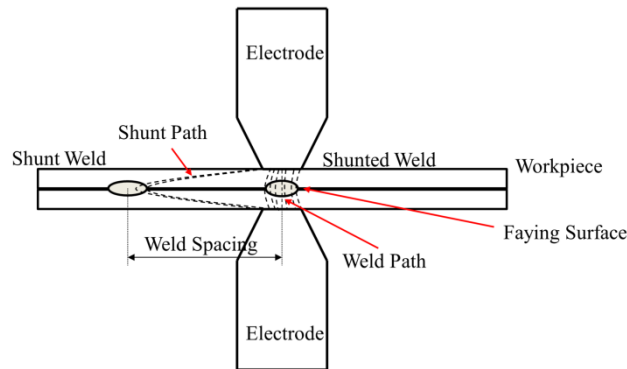
Figure 2.33 Schematic diagram of single shunting

Researchers have carried out experimental studies of the shunting effect of RSW on various metals. Wang investigated the effects of some experimental parameters on shunting and derived an analytical equation for shunting in mild steel, from which the critical minimum weld spacing for mild steel under various conditions was evaluated [120, 121]. Wang found that the contact resistance at the faying surface substantially affected the critical minimum welding spacing, as the consequent low electrode force and high contact resistance aggregated shunting. He also pointed out that darker and larger impression mark presented in shunted welds could be considered in the visual inspection of weld quality. On the other hand, it was found that the low electrical resistivity of aluminium made it more vulnerable to the shunting effect [122]. The use of increased current, rather than increased weld spacing, was more effective in solving the shunting problem in aluminum alloy. A triangular patterned weld sequence with

unequal-thickness aluminum was investigated by Li [123]. The contribution of the first weld to the shunting effect outperformed a second shunt weld when the welding spacing was small.

Apart from experimental investigation, some numerical studies have been conducted to assist understanding of the shunting problem [124-126]. Good agreement was achieved between simulated nugget diameters and measured ones. Moreover, the simulated current density for shunted welds was proportional to weld spacing. A heat compensation mechanism was revealed in multi-spot welds, as the shunted weld was heated by electrical current and temperature rose in the base materials due to the previous welds [123]. However, the existing studies modeled the shunting without the consideration of any workpiece deformation, and the physical properties of base materials were simplified, as shown Figure 2.34. The shunt path in actual conditions is much complex than that in the theoretical model. The air-gap created by making a shunt weld affects the contact condition while making a shunted weld. Actual shunting should consider electrical and mechanical phenomena.
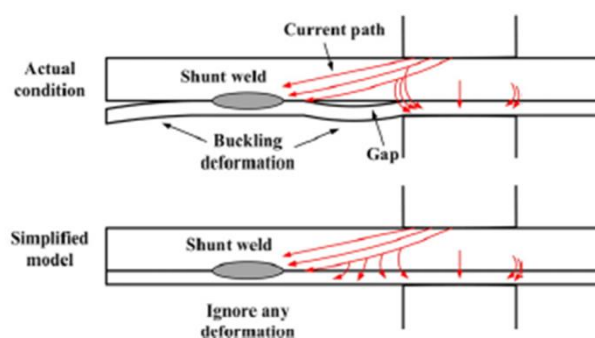
Figure 2.34 Actual shunting condition and the simplified model in Li's work [122]

The shunting effect has been documented via a range of dynamic signals, as manifested in Figure 2.35. Zhang conducted a case study of shunting problems based on the ED signals with a varied number of shunt welds and weld spacing [127]. A clear difference in the signals was observed among shunt and shunted welds that aligned with the difference between acceptable sized welds and undersized welds. On the other hand, the relationship developed in the TSS and profile quantities in the DR curves was found to contradict the trends observed in shunting [64, 128]. Likewise, the electrode vibration signals processed from ED accurately estimated the nugget diameters of the shunted welds [58]. In such cases, the vibration signal of double shunted welds showed different signal characteristics from those of the single shunted weld and the shunt weld. However, some key features in the vibration signals disappeared in the case of severe shunting, making the track of same profile quantities in shunting from vibration signals less favorable.
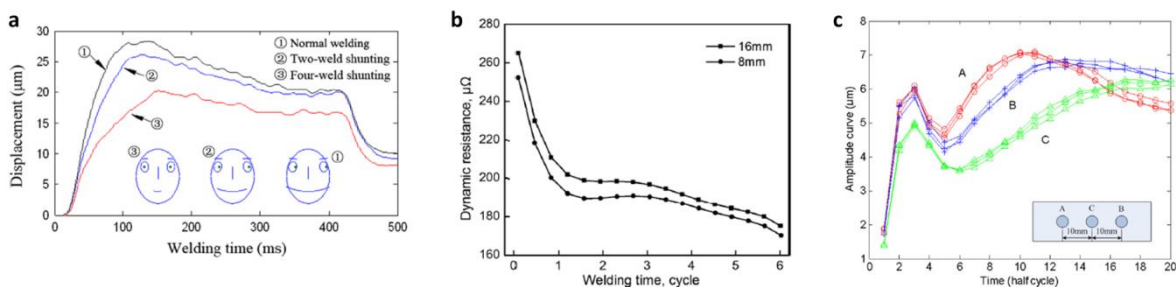
Figure 2.35 Dynamic signals of shunting effects in existing studies. a) ED [127]. b) DR [64]. c) electrode vibration [58].

2.4.4 Poor fit-up problem

Fit-up problem are process-related issues when more than one weld is made in the same area of the component. They result in the deformation of the sheets next to an existing weld, as shown in Figure 2.36.
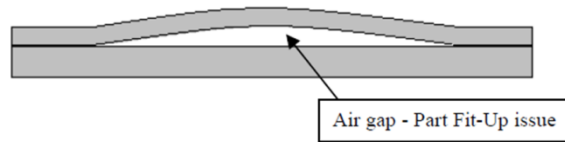
Figure 2.36 Fit-up problems in sheet metal stack [129]

In experimental and simulated studies, poor fit-up conditions were purposely introduced by inserting bars or triangle vices to create air gaps, as illustrated in Figure 2.37. An additional rod or shim was placed to create the poor fit-up condition experimentally. Cho exaggerated poor fit-up intensity by inserting a rod between two sheets of steel.
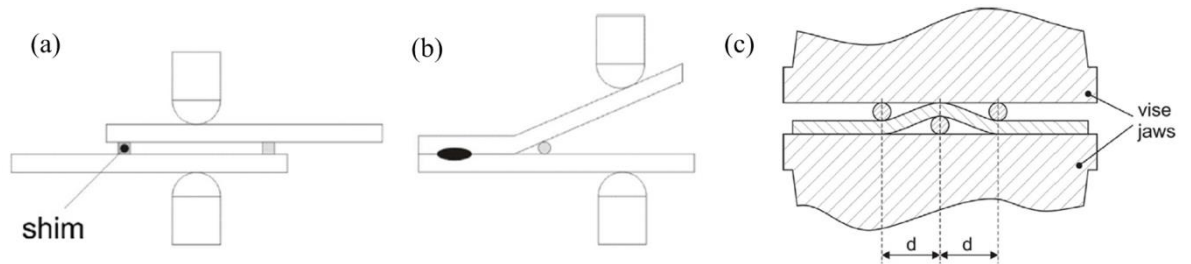
Figure 2.37 Poor fit-up problems presented in the literature. (a) from Jou [47]. (b) from Cho [101]. (c) from Podrzaj [130]

Poor fit-up problem have been found to significantly affect weld quality. Cho studied the influence of poor fit-up on weldability [101]. Compared to that of a normal weld, the weldability range of the weld with a fit-up problem was drastically narrowed. It was believed to have the strongest detrimental effect on the weld quality in aluminium over electrode misalignment. Brauser investigated production-related gaps in the deformation behaviour of TRIP steel [131]. The TSS and fatigue strength of samples with a gap of 3 mm were found to decline more than the gap-free sample. Poor fit-up was also likely to

43

trigger expulsion under moderate heat input [132]. The fit-up problem had to be addressed by changing some of the welding parameters. A pre-heating phase was used by Podrzaj and Kimchi, respectively [130, 133]. The additional preheating phase improved the weld strength with serious fit-up problems. However, Pordzaj also pointed out that regions with severe fit-up conditions could not be used for manufacturing spot welds, where additional preheating failed to compensate for the insufficient heat generation and produced undersized welds. Instead, these regions should be avoided in the production line. When a new weld is made in the region with a poor fit-up condition, part of the applied electrode force is used to eliminate the air gap. The effective applied force required to contain the molten metal is reduced accordingly. Expulsion is more likely to occur in these regions. Increasing the electrode force is believed to substantially improve the weld quality in poor fit-up problems, where the increment of electrode force is a function of electrode radius and the contact radius of the sheets [134]. Electrode force has been also considered as a good monitoring signal for quantitatively understanding the intensity of the fit-up problem. A force stepper was developed on an MFDC welder, where a three-level force profile considerably improved the weld quality by 10% [129]. A similar force stepper based on a neuro-fuzzy network was also presented by Zhang [135]. Some dynamic signals have been implemented to monitor poor fit-up problems in RSW. Different values of the signals were observed between good and poor fit-up conditions. Some profile features were extracted to allow control of the welding parameter to compensate for the insufficient heat generation.
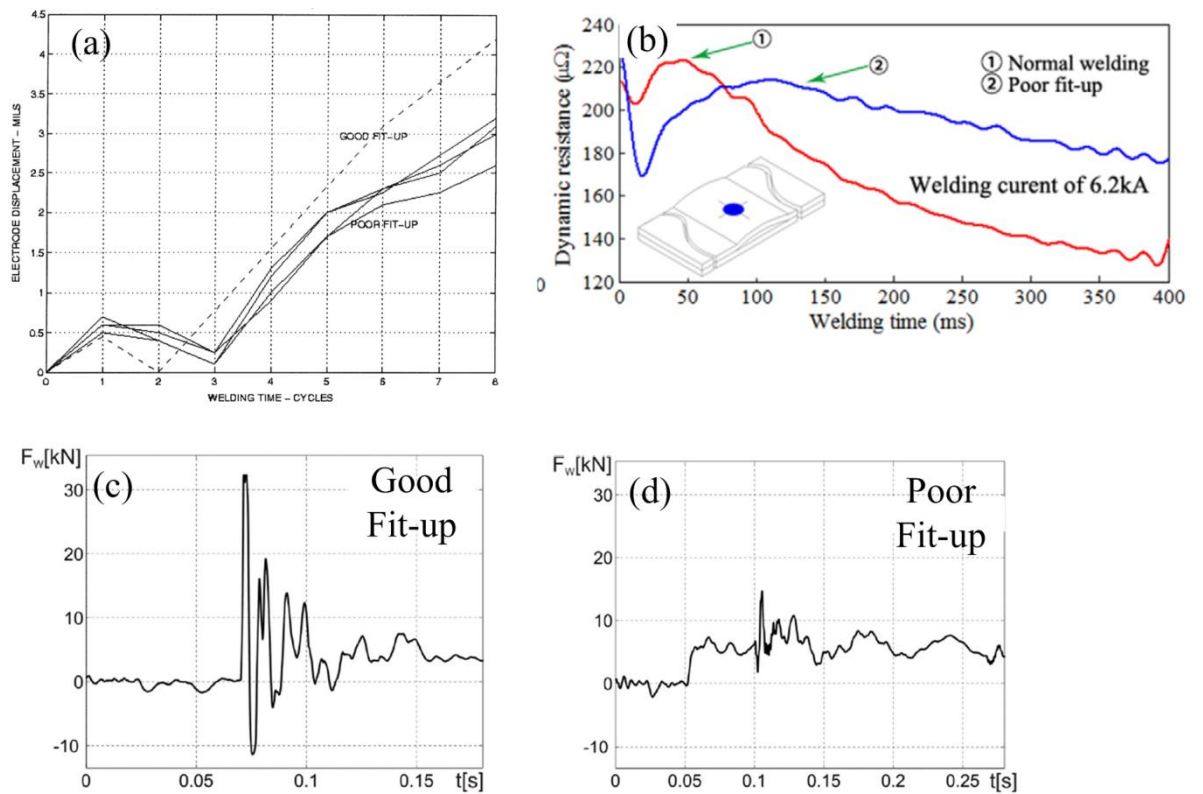
Figure 2.38 Existing dynamic signals of poor fit-up problem. (a) ED [47]. (b) DR [128]. (c) and (d) electrode force [130]

2.4.5 Close edged welds

A minimum distance from the edge is required when spot welding sheet metals. Deep indentation marks and considerable reductions of thickness can be found at the spot weld, leaving a deformed and non-cosmetic edge. Making spot welds at the edge of sheet metal can result in expulsion because there is limited surrounding metal to constrain the molten metal. However, spot welds close to edge are made due to the limited width of parts, as shown in Figure 2.39.

Figure 2.39 Spot welds close to edges in the B-pillar

A group of signals have been provided to monitor the welds close to edges, as shown in Figure 2.40. Zhang used an ED signal to characterize welds close to an edge [127]. He found that the temperature increased more rapiadly than that in a normal weld due to decreased heat dissipation. Also, the ED amplitude was much less than that in the normal weld. Wen showed the influence of closeness to an edge on the DR curves of stainless steel [64]. The short distance from the edge caused a rise in expulsion during welding stainless steel, and the endpoint value of the DR was proportional to the distance from the edge. Though different electrode vibration signal values were presented, the signals needed to be further processed to show the difference between a good weld and a weld close to an edge [58].
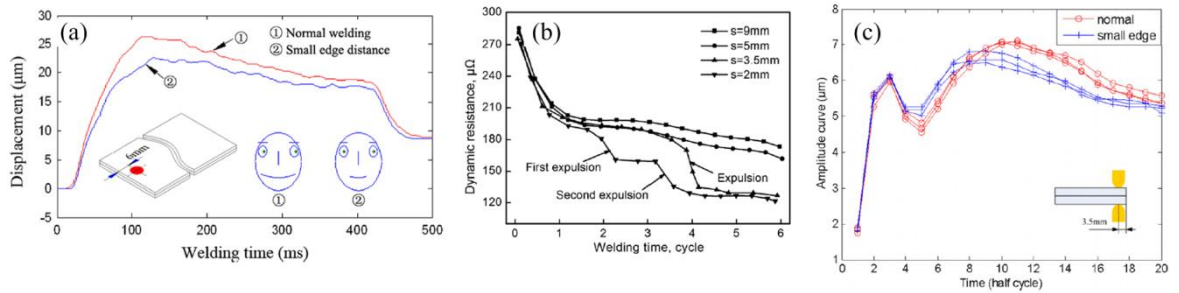
Figure 2.40 Existing dynamic signals on welds close to edges. (a) ED [127]. (b) DR [64].(c) electrode vibration [58]

To address the negative influence of closeness to an edge, Hirsch found that instead of using one pulse, three welding pulses could minimize expulsion for welds close to an edge, where the welding time was one-third of the original one [136].

2.5 Estimation of weld quality in RSW

The establishment of a non-destructive monitoring system for RSW is highly desirable. Attempts to establish quality estimation systems have been made based on a number of methods, using the characteristics extracted from the dynamic signals. For instance, the artificial neural network (ANN) has been described as a black-box model for evaluating the weld quality, based on the information collected in the RSW process. The ANN structure usually consists of three major components, input layer, hidden layer and output layer. The number of input variables depends on the signal of interest in the study, and the arrangement of the hidden layer, such as the number of nodes and functions among neurons, needs to be evaluated by a set of experiments. Data also needs to be divided into training set and test set, and cross-validation is necessary to avoid over-fitting.
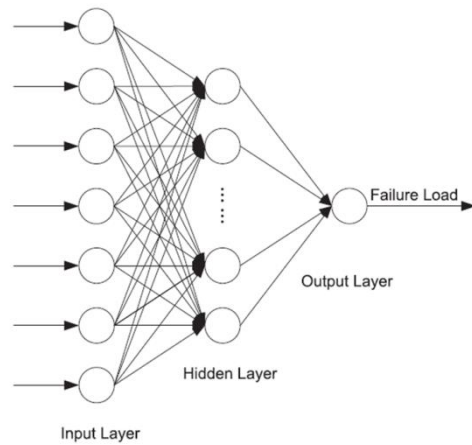
Figure 2.41 Schematic diagram of an ANN structure

A summary of typical existing work is presented in Table 2.1, with both achievements and drawbacks provided.

Table 2.1 Comparison of existing monitoring systems of RSW based on dynamic signals

Method	Data Source	Base Materials	Achievements	Drawbacks	Typical Studies
Non-linear regression	ED	Mild steel	Establishment of a nonlinear relation between ED features and tensile shear strength	Expulsion ignored in the study	[137]
Random forest (RF)	UO	Mild steel	Weld quality classifier based on UO signal, variable importance identified via RF approach, strong resistance to overfitting, and better classification accuracy than ANN and regression.	Off-line signal, UO, does not provide as much development history of nugget as DR does	[43]
Back propagation	DR and weld parameters	Titanium alloy	Satisfactory prediction of weld quality based on	User fails to interpret ANN	[74]

48

neural network (BPNN)			principal components from DR signals and weld parameters	mechanism, and principal components derived from DR do not have much physical meaning	
Chernoff face Analysis	ED	Mild steel	Efficient in distinguishing good welds from expulsion and welds under abnormal conditions based on facial impression	Further processing of the facial impression to weld quality classifier relies on human operator judgment.	[127]
BPNN and probabilistic neural network (PNN)	DR and voltage	Titanium alloy	Different applications for tested neural networks. BPNN predicts failure load while PNN focuses on weld quality	The interpretation of ANN is very challenging	[138]
Linear vector quantization (LVN)	DR	Zinc-coated steel	Intrusive sensor affecting the welding operation is not required. A small training set is required.	DR shows limited discernible features in Al and Mg alloys, making classification difficult.	[139]
Hidden Markov models (HMM)	ED	Mild steel	Good prediction of weld strength based on the fluctuation features of ED, while greater error is ottained from the HMM based on ED curves.	High accuracy in HMM relies on the training set.	[53]

Note: ED- Electrode displacement. UO- Ultrasonic oscillogram. DR- Dynamic resistance.

Breiman proposed a pattern recognition technique, the Random forest (RF), as a mathematical model for classification [140]. The schematic diagram of a RF model is shown in Figure 2.42.
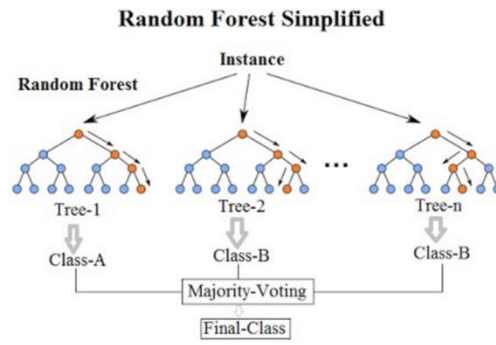
Figure 2.42 Schematic diagram of a simplified RF model

The RF method adopts an ensemble of independent decision trees $h_i\{X\}$ (i=1,2…k). The classification result of the RF is an unweighted majority based on the voting of each independent tree, which is considered as a weak learner. Each tree is planted under independent random vector Θ of the identical distribution. A bootstrapping method creates *ntree* sample sets constituting of about $\frac{2}{3}$ of the original data set, in which *ntree* indicates the total number of trees. In the performance of the bootstrapping method, approximately one-third of the original data being unselected for each tree, referred as out-of-bag (OOB) data.

The advantages of applying RF over current quality monitoring methods lie in the better interpretability of the algorithm and its capability of sorting out thousands of features and dealing with missing values. The evaluation of variable importance provided by RF allows users to identify the importance of variables and possibly reduce the dimension of the data. Current methods, such as the artificial neural network (ANN) and non-linear regression, are prone to overfitting when the training set is improperly evaluated, whereas the RF exhibits appealing overfitting resistance with an increased number of trees [140]. So far, efficient application of the RF in monitoring RSW weld quality has rarely been demonstrated. Only two ultrasonic signal oriented studies in the laboratory environment were found. Martín incorporated ultrasonic oscillograms into an RF

50

classifier, in which four levels of the weld, namely good weld, no weld, undersized weld and stick weld, were considered as the classes for RF classification [141]. Pereda compared a series of the ultrasonic waveform based classification methods including RF for the quality assessment of RSW. From the classification results and the receiver operating characteristic (ROC) curve, the RF technique was shown to outperform some popular classification methods such as ANN and logistic regression [43], as demonstrated in Figure 2.43.
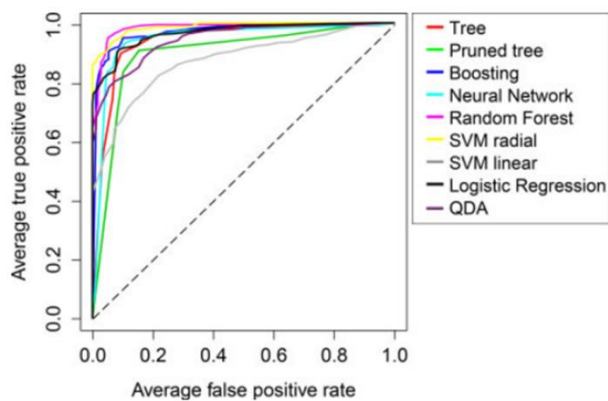
Figure 2.43 Receiver operating characteristic curve for each method tested; dotted line represents random guessing [43]

Chapter 3 Experimental Method

3.1 Material used in this study

3.1.1 Zinc-coated and bare steel sheet

In this study, several types of zinc-coated steel and bare mild steel were purchased from BlueScope Steel. The bare metal was 1-mm-thick cold rolled steel CA2S-E, of which the chemical compositions and material properties are listed in Table 3.1 and 3.2.

Table 3.1 Chemical composition of CA2S-E (wt %)

Material	C	Si	S	P	Mn	Al	Fe
CA2S-E	0.04 – 0.07	0.005 – 0.01	0.008 – 0.02	0.005 – 0.02	0.18 – 0.25	0.03 – 0.05	Bal.

Table 3.2 Mechanical properties of CA2S-E

Material	Yield Strength (MPa)	Ultimate Tensile Strength (MPa)	Elongation (%)
CA2S-E	160 – 250	270 – 340	34 – 46

1-mm-thick G2S galvannealed steel and 1-mm-thick G2 galvanbound (GB) steel were used for endurance test. The chemical compositions are provided in Table 3.3. The minimum zinc mass of GA and GB coating are 100 g/cm^2 and 275 g/cm^2, respectively.

Table 3.3 Chemical composition of G2S and G2 (wt %)

Material	C	Si	S	P	Mn	Al	Fe
G2S	0.035 - 0.07	≦ 0.02	≦ 0.02	≦ 0.02	0.20 - 0.30	0.02 - 0.07	Bal.
G2	0.35 - 0.07	≦ 0.02	≦ 0.02	≦ 0.025	0.20 - 0.30	0.02 - 0.07	Bal.

Table 3.4 Mechanical properties of G2S and G2

Material	Yield Strength (MPa)	Ultimate Tensile Strength (MPa)
G2S	290	350
G2	290	350

3.1.2 Electrodes

In the previous studies, different electrode shapes and different compositions of electrodes were used. The design of the tip morphology notably affects the temperature distribution, force distribution, contact condition, resistance against expulsion and the degradation of the electrodes. On the other hand, the electrode composition determines the alloying reaction with base metals. Cu-Cr and Cu-Cr-Zr are the most commonly used electrodes in steel welding, Cu-Al$_2$O$_3$ electrodes have also been investigated for preventing electrode wear.

In this study, 6-mm-diameter Cu-Cr truncated electrodes were used, in which the raw copper bar was manufactured via cold extrusion. The detailed electrode geometry is presented in Figure 3.1.
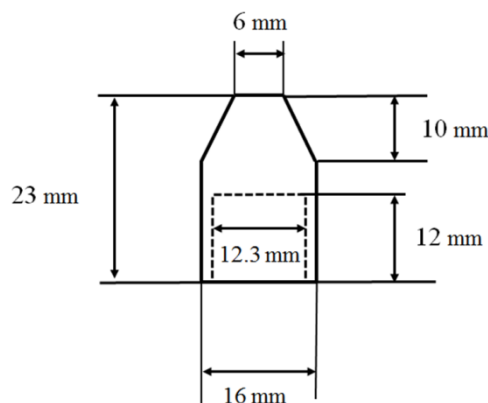
Figure 3.1 Geometry of the electrodes used in this study

3.2 Preliminary experimental work

3.2.1 Experimental set-up

Spot welding sessions of steel were carried out on a single phase AC pedestal welder (EasyBeat, DN-50), as shown in Figure 3.2, at the frequency of 50 Hz. The duty cycle was ten welds/ min. The capacity of the AC welder was 75 kVA. It had three welding stages: preheating stage, welding stage, and tempering stage. The electrode force was pneumatically controlled, with the pneumatic pressure ranging from 0.3 MPa to 0.7 MPa.
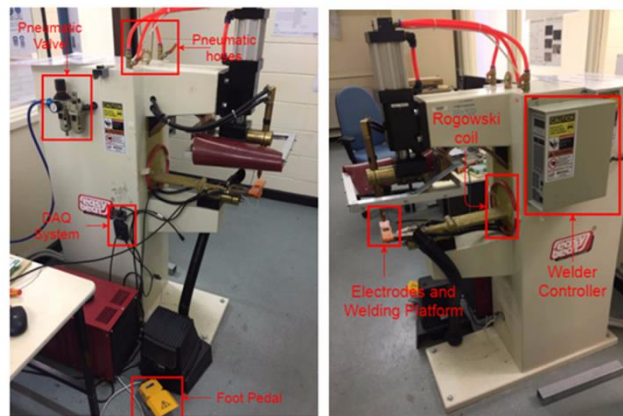
Figure 3.2 DN-50 AC pedestal welder

3.2.2 Dynamic signal collection
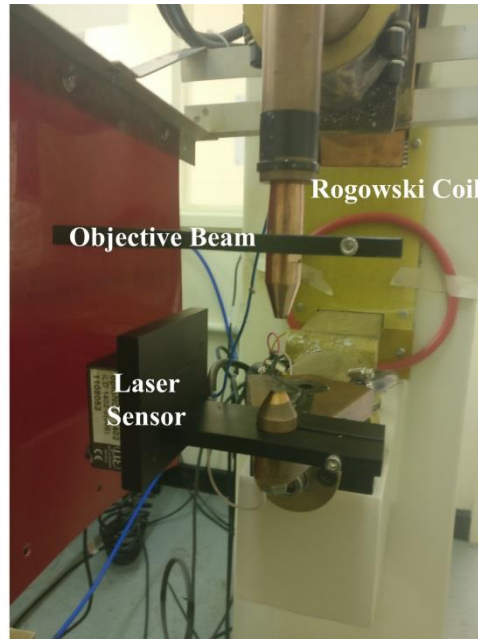
Figure 3.3 Dynamic signal measurement system

The experimental set-up used with the AC welder is shown in Figure 3.3. Electrode displacement, welding voltage across electrodes and welding current were recorded simultaneously. The ED system consisted of a MICRO-EPSILON non-contact laser displacement sensor (optoNCDT 1402-5) and an objective beam. The sensor fixture and the objective beam were made of engineering plastic that had an appealing combination of mechanical strength and resistance to thermal expansion. The laser displacement sensor had resolution of 1 μm, capable of probing the movement of the electrode due to thermal expansion of the nuggets.

A Rogowski coil was used to record the current waveforms, and the electrical potential of the electrodes was recorded from the secondary circuit. The sampling frequency was 10 kHz. Welding current I_w and welding voltage U_w were acquired for DR computing. In this study, the DR was calculated via the RMS method, using the equations:

$$R_{RMS} = {U_{RMS}}\big/{i_{RMS}}$$

(3.1)

$$U_{RMS} = \sqrt{\frac{1}{N}\sum_{i=0}^{N} v_d^2}$$

(3.2)

$$I_{RMS} = \sqrt{\frac{1}{N}\sum_{i=0}^{N} i_d^2}$$

(3.3)

where U_{RMS} and I_{RMS} are the effective voltage and current every half cycle, respectively; v_d and i_d are the original welding voltage and welding current sampled; N is the number of sampling points each half cycle.
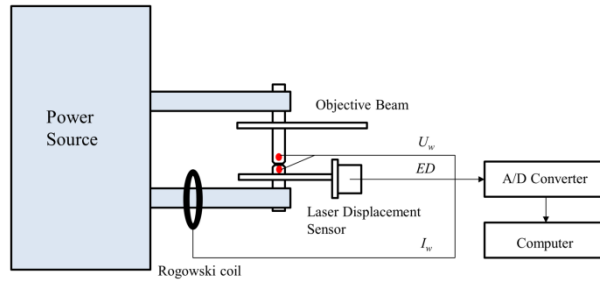
Figure 3.4 Schematic diagram of the experimental set-up

The signal collection set-up of electrical current, voltage and ED is shown in Figure 3.4. A National Instrument board (USB-6008) was used to convert analog data to the computer. The original ED oscillated at the frequency of 100 Hz corresponding to the changed temperature of the sheets that was twice of that of the spot welder (Ref. 23, 24). A low-pass Butterworth filter was adopted to remove the signal oscillation. Carbon imprints of the electrodes were taken for misalignment check on the basis of 50 welds during the test. The binary carbon imprints were then analyzed under ImageJ to

calculate the tip area and tip diameter (Ref. 25). Side and top views of the electrodes were captured with a CCD camera at the end of electrode life. Active contour segregation method (Snake Active Contour package) was applied to track the electrode outline under Matlab (Ref. 12, 26). The width of the electrode tip, a parameter to characterize the level of mushrooming, was calculated using Cullen's method (Ref. 13).

3.2.3 Construction of a RF-based quality monitoring system in RSW mild steel

Four welding parameters, namely weld current (WC), weld time (WT), electrode force (EF) and hold time (HT), comprised a welding schedule. The first three parameters determined heat input in the weld stage; while HT value accounted for the cooling rate of the molten metal. A DR curve was first used to construct the system. AS HT did not differentiate values of DR, the control variables selected were selected as WC, WT and EF. Detailed welding parameters are shown in Table 3.5.

1-mm thick mild steel CA2S-E was used, and the welding session was done under a DN-50 AC welder. To reproduce the destructive test frequency in the plant environment, two types of welds were made, namely destructive weld and continuous weld. In total, seven welds were made. Three destructive samples were stretched until failure at every welding schedule. The other four welds were made on the same sheet metal with a weld spacing of 20 mm, in which shunting effect did not substantially affect the nugget size of bare mild steel [120]. The weld schedule began with weak parameters (small weld current and short weld time) and the EF was initially fixed at 1700 N. When an expulsion was identified, the subsequent experiment using the current welding schedule was terminated. The EF was increased, and weld current and weld time was applied with weak parameters again. Hence, not all combinations in Table 3.5 were carried out. In total, 368 welds were made and were later used to construct RF models.

Table 3.5 Welding schedule used in the RF model construction

Weld Current	Weld Time	Electrode Force	Hold Time
8.0 kA	160 ms	1.7 kN	200 ms
8.8 kA	200 ms	2.0 kN	
9.6 kA	240 ms	2.3 kN	
10 kA		2.7 kN	
10.4 kA			
10.8 kA			
11.2 kA			

A RF classifier was implemented, using the "random forest" R package [142]. For every node in a kth tree $h_i\{X\}$ (i=1,2…k), *mtry* features were selected out of the total *M* features of the input data. The value of *mtry* had to be much lower than *M*; otherwise, the correlation among trees would strengthen. A high value of *mtry* would adversely affect the accuracy and reliability of the RF classifier. The *mtry* features were employed to determine the optimum split variables and the best split-point. This recursive step continued until a maximal tree was created, suggesting that the optimum split parameter for the current node was identical to that of the parent node. No pruning was carried out for any tree. These actions allowed a low bias among the ensemble of decision trees. Likewise, randomization had to be assured for the RF model. It was accomplished by a series of operations, including bootstrapping, a random *mtry* selection from each node and optimization of the value of *mtry*. The low bias and low correlation guaranteed reliability of the RF model.

The decisions of the parameter *ntree* and *mtry* tended to substantially affect the accuracy of the classifier. A discussion of the sensitivity to *ntree* and *mtry* was performed. The original data were divided into a training set (75%) and test set (25%). The RF models were constructed based on the training set, making the test set independent of the RF models. Ten-fold cross-validation was conducted on the training data to examine the overfitting.

3.2.4 Spot welding under abnormal process conditions

Electrode Misalignment

The carbon imprints provided a good indication of the alignment of the electrodes. Axial misalignment and angular misalignment and their relative shapes in the carbon imprints are presented in ISO standard 18278-2:2004 in Figure **3.5** [103]. The carbon imprints were collected in the manufacturing process, where the spot welding was done in the usual manner without applying any welding current. Moreover, a carbon imprint paper was placed on a steel sheet, and a white paper with grid lines was placed between the steel sheet and the carbon imprint paper.
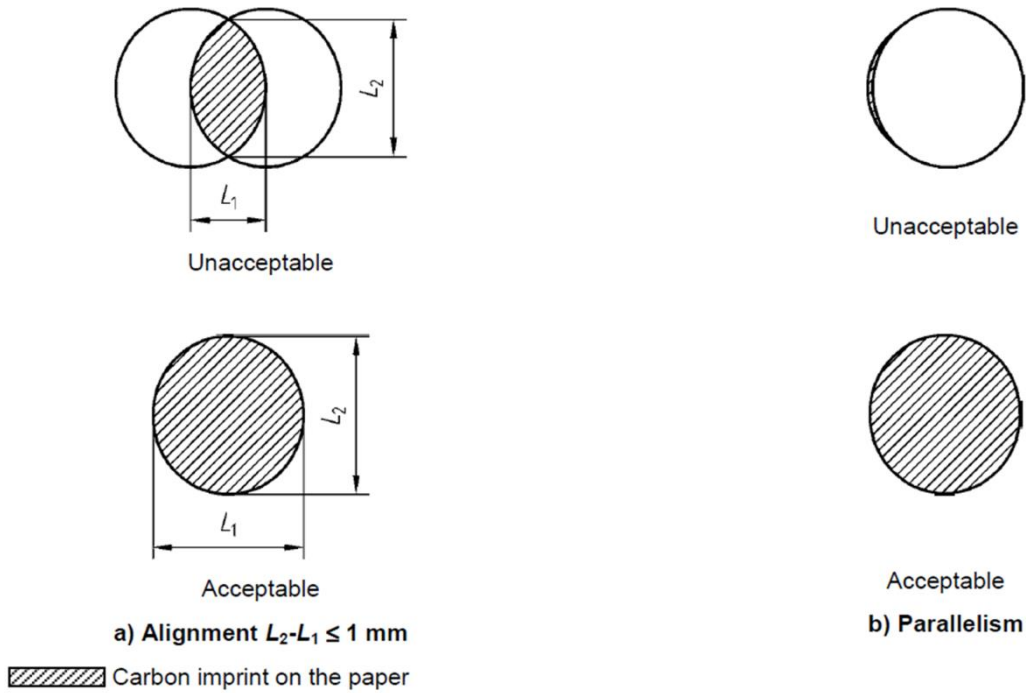
Figure 3.5 Typical carbon imprints with electrode alignment

The flexibility of the welding arm accounts for electrode misalignment in the production environment. The welding machine arm for positioning the upper electrode was manually rotated to 5° to create angular electrode misalignment due to the flexibility of the spot welder. Note that any severe electrode misalignment as in Figure 3.5 (a) was not considered in this work, as it would drastically narrow the weldability lobe and expulsion could not be contained by the electrode force. The appearance of the weld also implies whether electrode misalignment has occurred, as manifested in Figure 3.6. An uneven indentation mark can be seen when electrode misalignment occurs, whereas a complete indentation ring can be observed in normal conditions. An uneven indentation mark or expulsion at the faying surface or sheet surface suggests that the electrode does not contact properly with the base metals.
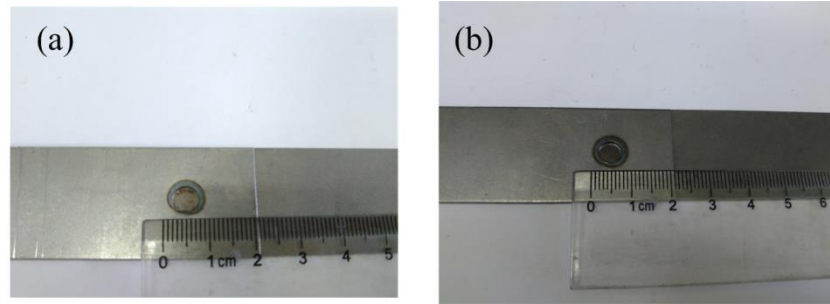
Figure 3.6 Weld appearances of (a) misalignment and (b) normal condition

Shunting
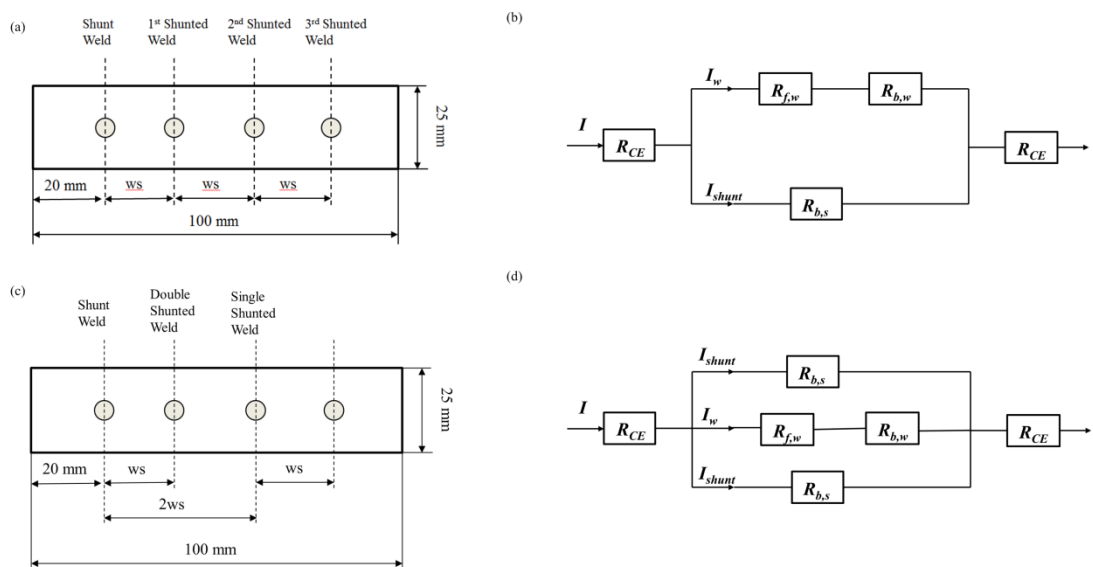
Figure 3.7 Schematic diagram of welding sequence applied. (a) single shunting. (b) equivalent circuit for single shunting. (c) double shunting. (d) equivalent circuit for double shunting.

Spot welds were made in the sequences arranged as shown in Figure 3.7 (a) and (c), with altered weld spacing (*ws*). These two distinct weld sequences created single shunting and double shunting, respectively. Shunted welds were named after the order of the production sequence; thus, shunted welds next to shunt welds were referred to first shunted welds, and shunted welds next to the first shunted welds were referred to second shunted welds. Similar naming were also applied to double shunted welds. The equivalent circuits of single and double shunting are presented in Figure 3.7 (b) and (d),

respectively. The welding current I_w and shunting current I_{shunt} in single shunting are calculated by

$$I_w = I \cdot \frac{R_{b,s}}{(R_{b,s} + R_{b,w} + R_{f,w})}$$

(3.4)

$$I_w = I \cdot \frac{(R_{b,w} + R_{f,w})}{(R_{b,s} + R_{b,w} + R_{f,w})}$$

(3.5)

I is the overall welding current flowing from the electrode. $R_{b,s}$ is the bulk resistance of the shunting path, and $R_{b,w}$ is the bulk resistance at the welding path, and $R_{f,w}$ is the contact resistance at the faying surface. $R_{b,s}$ was found to be inversely proportional to the weld diameter of the shunt and shunted weld and proportional to the weld spacing and the thickness of the sheet; $R_{b,w}$ and $R_{f,w}$ were found to be independent of weld spacing [121]. The problem was simplified by assuming that $R_{b,s}$ for the shunting path was identical in double shunting. Thus, the equivalent equation of I_w of double shunting was derived:

$$I_w = I \cdot \frac{\frac{1}{2} R_{b,s}}{(R_{b,s} + R_{b,w} + R_{f,w})}$$

(3.6)

where $\frac{1}{2} R_{b,s}$ is the equivalent bulk resistance for two parallel shunt welds. When the ratio $(R_{b,w} + R_{f,w}) / \frac{1}{2} R_{b,s}$ increased, the portion of the shunting current I_{shunt} simultaneously increased.

1-mm thick CA2S-E mild steel was welded under the DN-50 AC welder. The weld parameters that identify the appropriate welding current are listed in Table 3.6. Each weld sequence was repeated three times with the optimal welding current. The time

interval between two adjacent welds was 15 s. Before measuring signals on shunted welds, electrode conditioning was implemented on the 1-mm-thick mild steel. According to Hu's work, it is necessary to eliminate dynamic behavior in the joint strength of a new pair of electrodes [95]. Welding parameters in the electrode conditioning included 8.8 kA of welding current, an EF of 2.7 kN and the welding time of 0.2 s. The electrode conditioning was continued until consistent ED signals were obtained for ten welds.

Table 3.6 Welding parameters used in the shunting study

Current (kA)	Time (ms)	Electrode Force (kN)	Weld Spacing (mm)
7.2,8.8,10.4	200	2.7	8, 12, 15, 24, 30

Fit-up problem

A poor fit-up problem occurs when a number of welds are made in the same area of a component. An air-gap greatly affects the contact condition of sheets, requiring a large portion of the EF to suppress it. The fit-up problem used in this study was presented as shown in Figure 3.8, where the fit-up intensity, denoted by *H*, varies from 0 to 2 mm. Two fit-up problem types, depending on the welding sequence, were presented. Figure 3.8 (a) presents a typical fit-up problem in the sheet when a spot weld was made in the same area. Figure 3.8 (b) demonstrates the air-gap generated between two existing welds. The inserted strips were made of thin metal shims (0.1mm thick) and masking tape was used to prevent any electrical current diverted by this path. It can be seen that double shunting could also create poor fit-up conditions, similar to this example. A 1-mm thick CA2S-E mild steel sheet was used and the study was performed under the DN-50 pedestal welder. The welding parameters used are listed in Table 3.7

Table 3.7 Welding parameters used in poor fit-up problem

Current (kA)	Time (ms)	Electrode Force (kN)	Gap intensity (mm)
8.8	200	2.7	0, 0.5, 1.0, 2.0
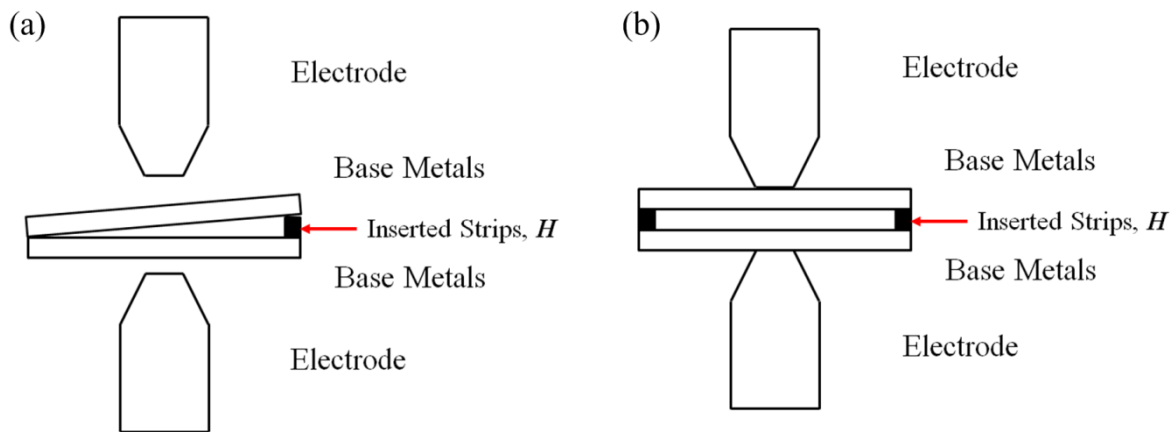
Figure 3.8 Schematic diagram of fit-up problem. (a) one-sided gap. (b) double-sided gap

Close edge problem

Spot welds were purposely produced close to the edge of the sheet, as shown in Figure 3.9, where L is the distance between the edge of the sheet metal and the position of the spot weld. A very small L leads to a severe expulsion, rendering the dynamic signal collected less useful. Thus, the minimum distance from the edge was set at 6 mm, where no expulsion was seen. The weld spacing (ws) between close edged welds was 30 mm, enabling a major portion of welding current to be transmittied through the faying surface. All spot welds were made under the welding parameters in Table 3.8 under the DN-50 AC welder, with 1-mm thick CA2S-E mild steel sheet used.
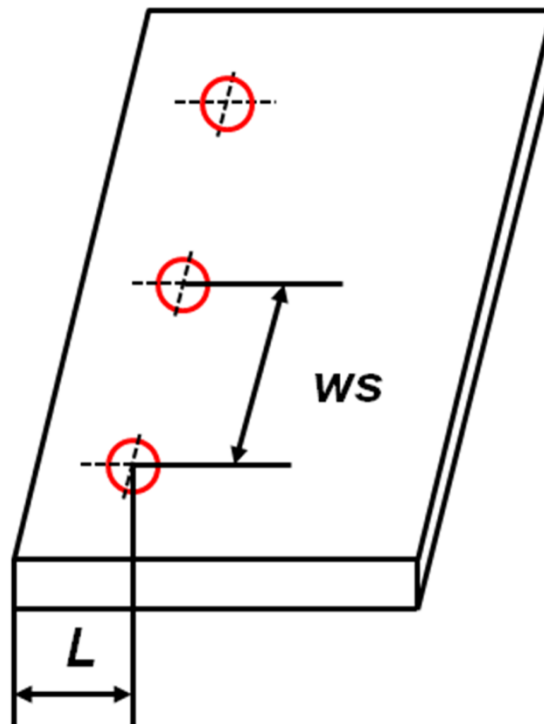
Figure 3.9 Schematic diagram of a close edged weld

Table 3.8 Welding parameters used in the close edged welds

Current (kA)	Time (ms)	Electrode Force (kN)	Distance from edge (mm)
8.8	200	2.7	6, 8, 10

3.2.5 Electrode life test procedure

3.2.5.1 RSW of Zn coated steel

In this subsection, the welding parameter used for theelectrode endurance study is presented in Table 3.9. Then, artificial electrode misalignments were produced for two tested groups in Table 3.10, respectively. Five tensile-shear specimens were tested at 50 weld intervals.

Table 3.9 Welding parameters used for the endurance test

Material	Welding Current	Welding Time	Electrode Force	Hold Time
GA	11 kA	200 ms	2.7 kN	500 ms
GB	11.5 kA	200 ms	2.7 kN	500 ms

Table 3.10 Initial configuration of the electrode alignment in the endurance test

Material	L1 (horizontal, mm)	L2 (vertical, mm)	Carbon Imprints
GA	5.96	5.86	
GB	5.90	5.82	

If the averaged tensile-shear strength dropped below 80% of the initial value, the electrodes were considered to reach the end-of-life. The cross-sections of spot welded samples were examined at 50-weld intervals. Worn electrodes in the electrode life test were prepared by the standard metallurgical method for an optical microscope (OM) and scanning electrode microscope (SEM) at 10 and 200 welds. In addition, the side views and the top views of the worn electrodes were taken with a CCD camera, as shown in Figure 3.10.
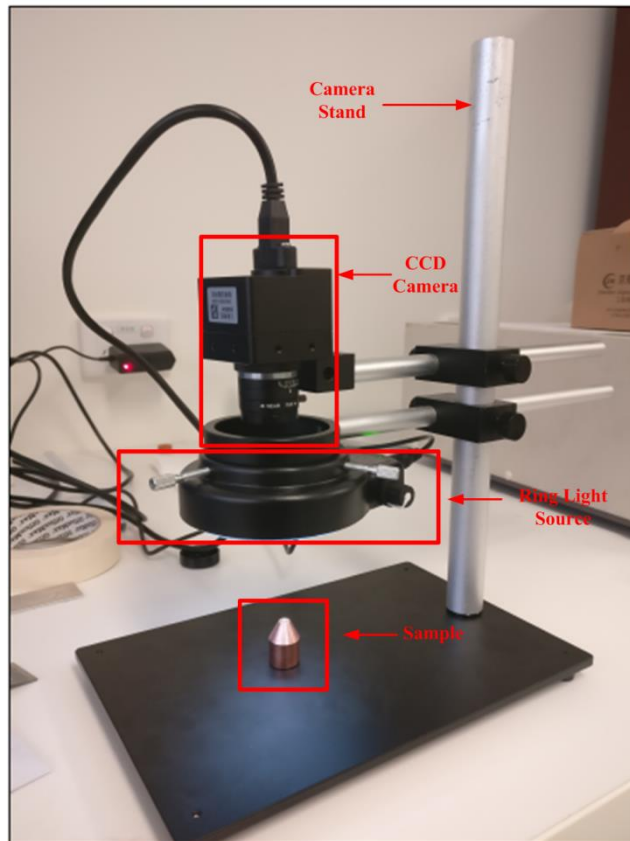
Figure 3.10 CCD camera set-up

3.2.6 Destructive test and Vickers microhardness test

The tensile shear test is a measure of the quality of a resistance spot welded joint. A joint is subjected to a pair of parallel forces until destruction. The tested specimens were prepared to a size of 100 mm x 25 mm and the overlap area was 25 mm × 25 mm as shown in Figure 3.11. An Instron 4505 was used in this study, as shown in Figure 3.12. The crosshead velocity was 5 mm/min.
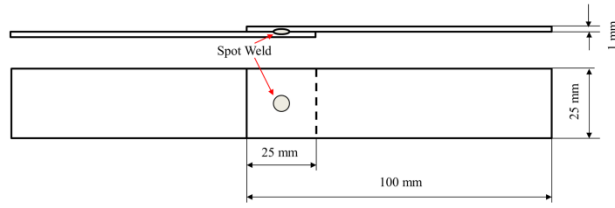
Figure 3.11 Specimen dimension for tensile shear test

Figure 3.12 Instron 4505 universal test machine

The microhardness of the worn electrodes was measured by a Vickers microhardness tester (MHT-1, Matsuzawa), with a load of 100 g and a load time of 15 s The positions for Vickers microhardness are demonstrated in Figure 3.13, in which points were sampled at a distance of 0.5 mm. The Vickers microhardness was calculated via:

$$Hv = 1.8544 \cdot \frac{F}{d^2}$$

<div align="right">(3.7)</div>

where F is the indenter load (N), d is the diagonal length of the indentation mark (mm).
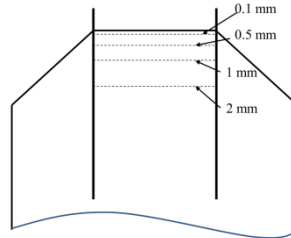
Figure 3.13 Schematic diagram of the positions of Vickers microhardness tests

3.3. Microstructure characterization

3.3.1 Sample preparation

Samples for OM and SEM had to be prepared using a standard metallurgical procedure. The fresh etching reagent (25 ml ammonia + 5 ml hydrogen peroxide + 25 ml distilled water) was used to reveal the grain boundary and recrystallization regions of the copper electrodes. 4% nital reagent was used for etching the steel. The samples for EBSD were prepared with SiC papers (600 grit, 800 grit and 1200 grit) and 3 μm and 1 μm diamond suspension; then the 0.02 μm colloidal silica suspension was used for the final mechanical-chemical polishing. Ion milling was used to improve the index rates for EBSD mapping under Leica EM TIC 3x in Figure 3.14 . The ion milling parameters were 10 V, 2 mA and 10 mins, while the stage was oscillated by 20° with a tilt angle of 3°.

Figure 3.14 Leica EM TIC 3x

3.3.2 Experimental configurations

The samples were analyzed under a Nikon stereomicroscope (shown in Figure 3.15) for low-magnification images and an MDS metallurgical light microscope for high-magnification images.

Figure 3.15 Nikon stereomicroscope

A Hitachi 4300 scanning electron microscope was used to characterize the base metals and the electrode after welding. The chemical compositions of samples were measured by an energy-dispersive spectrometer (EDS), shown in Figure 3.16. The working configurations for the EDS were voltage of 15 kV, working distance of 25 mm and probe current of 600 pA.
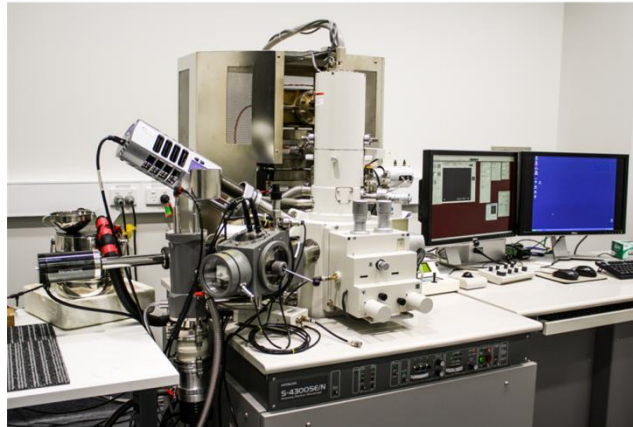
Figure 3.16 Hitachi 4300 SEM

The EBSD analysis was carried out under a Zeiss Ultraplus FESEM (demonstrated in Figure 3.17), where the working distance of 25 mm, beam current of 4 nA and accelerating voltage of 15V were implemented during mapping. The accelerating voltage and beam current values were found to substantially influence the index rate and the strength of the Kikuchi pattern [143]. Because refined grain was found in the recrystallized region, a low accelerating voltage produced good resolution. The beam current value affected the interaction zone on the sample surface. To reduce the scanning time, the step sizes selected were 1 μm and 0.5 μm for the base metals and recrystallization regions, respectively. The rolling direction (RD) was perpendicular to the electrode surface.

Figure 3.17 Zeiss Ultraplus FESEM

Chapter 4 Construction of random forest-based quality monitoring system in RSW

To advance the technique for monitoring weld quality of RSW from the laboratory to the plant environment, dynamic resistance, a reliable and affordable dynamic signal, is here proposed in preference to ED or EF for monitoring weld quality in RSW. In this section, an experimental study of a RF-based classifier using DR signals of mild steel is presented.

The welds made for RF construction were divided into TST samples and continuous welds, similar to the weld sequence in the production environment. The DR curves of shunted welds were found to vary from those of normal welds when weld spacing was sufficient. Profile features with physical meanings were used for RF construction, and their importance to classification accuracy was further evaluated and ranked. Additional DR gradient and weld parameters were included to improve the accuracy of classification.

4.1 Class selection for RSW weld quality classification

Weld quality can be divided into three major types based on failure modes.
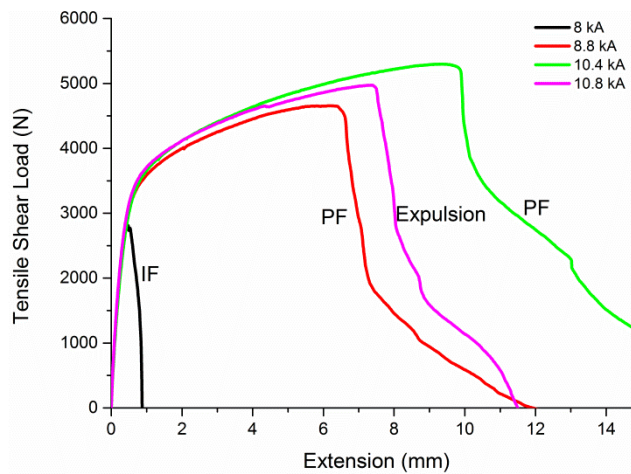
Figure 4.1 Extension-load curves of different weld qualities.

Averaged extension-load curves of the tested specimens using different welding current are demonstrated in Figure 4.1. Distinguishing interfacial failure (IF) and expulsion from pull-out failure (PF) is strightforward. The IF specimen does not exhibit an desirable tensile shear load bearing capacity prior to failure, whereas the specimen with expulsion presents a downward trend in tensile-shear load and failure energy, though a greater heat input is applied. Specimens with PF mode attain a good combination of strength and ductility and thus were viewed as good welds.

Furthermore, Figure 4.2 displays three types of RSW weld failures after the TST. Figure 4.2 (a) shows rupture of the couplers in the interfacial shear mode, suggesting that an undersized weld had formed. In Figure 4.2 (b), the specimen failed in PF mode. The weld nugget was preserved after the test. The fracture initiated from the HAZ region, indicating that the HAZ was prone to cracking. In Figure 4.2 (c), expelled molten metal on the faying surface was seen after the TST. Deficiency of the weld nugget was generated, and the mechanical performance was deteriorated. Based on the extension-load curves, the failure mode, and observation on expulsion, three weld quality classes were utilized as the classification response in the RF model, indicating undersized weld, acceptable sized weld, and expulsion.
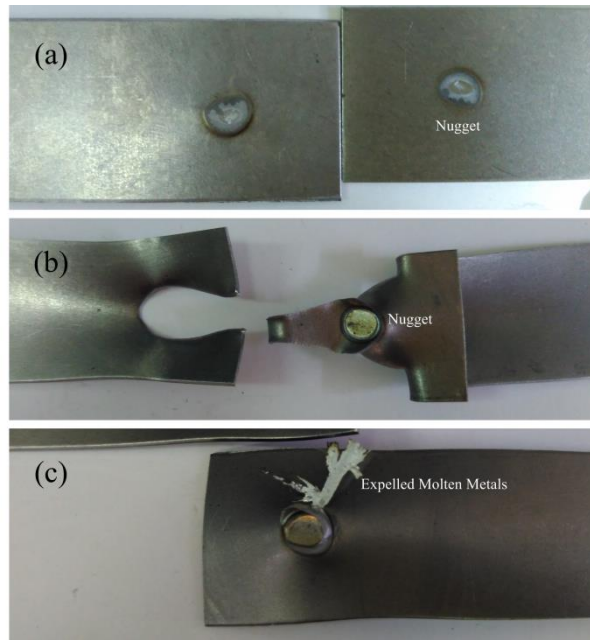
Figure 4.2 Three types of failure in RSW. (a) cold weld. (b) good weld. (c) expulsion

4.2 Characteristics of dynamic resistance signature on RSW

Welding current and welding voltage were collected and processed, as shown in Figure 4.3. The effective voltage and current were calculated per half cycle.
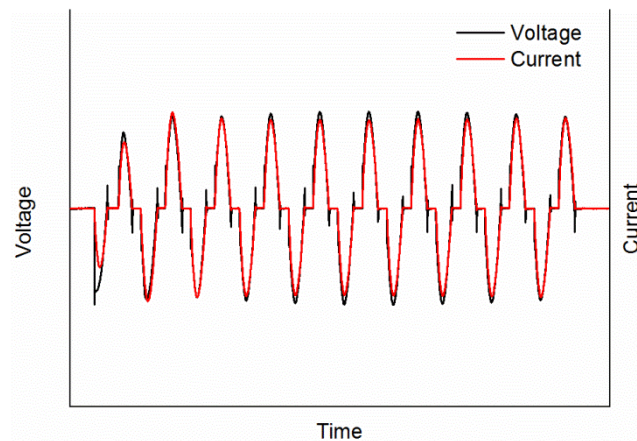
Figure 4.3 Welding current and welding voltage collected in the AC pedestal welder

As mentioned, root-mean-square DR was used to represent the dynamic resistance. The nature of different weld time causes the difference in the lengths of the DR curves,

making direct importation of the DR signatures into the RF classifier less feasible. Instead, some characteristics were extracted to describe each DR plot. From the DR curve of mild steel presented in Figure 4.4, the DR first declined until the trough α, then climbed to reach the β peak. After this extreme point, the DR showed a descending trend to the terminal point of the DR curve.

Three stages corresponded to specific physical phenomena in the RSW process. Stage I indicated the intimate contact of workpieces and breakdown of asperities. With the increased contact area, the DR unambiguously dropped. Stage II was indicative of local melting and formation of the nugget. The bulk resistivity of the steel increased along with the ascending temperature. The elevated bulk resistivity outperformed the influence of contact area reduction in nugget nucleation, accounting for the rise in DR in Stage II. After the β peak, the DR curve gradually decreased with the enlarged nugget diameter until reaching the end point in Stage III.
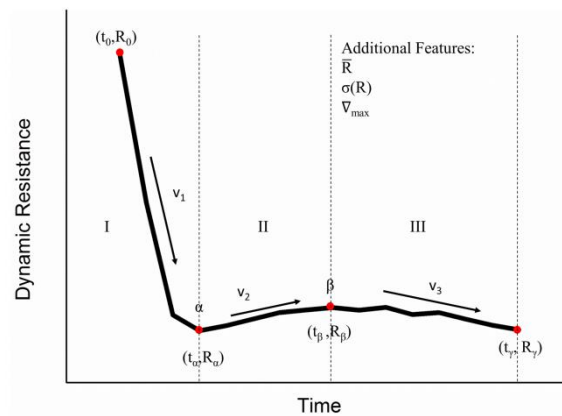
Figure 4.4 Schematic diagram of extracted features of the representative DR curve

In total, nine features ($M=9$) were selected to describe the DR curves for the training dataset. These extracted features, shown in Figure 4.4, were critical DR values of trough R_α, peak R_β, end point of DR curve R_γ and their relative velocities for surface asperity breakdown v_1 (Stage I), local melting and initiation of nugget formation v_2 (Stage II),

and nugget growth v_3 (Stage III). The maximum absolute gradient in Stage III ∇_{max} was also recorded to ensure the accuracy to distinguish minor expulsion from an acceptable sized weld. When minor expulsion occurred, the decline in DR sometimes might not be differentiated from an acceptable sized weld if only the overall gradient in Stage III was considered. The maximum absolute gradient better described the sudden change in DR. Moreover, the averaged DR value $\bar{R}$ and standard deviation σ of the DR curve were taken into account because the expulsion produced a rise in the precipitous drop in DR value.

Representative DR curves for three weld quality classes are plotted in Figure 4.5, with a constant EF of 2.7 kN and weld time of 12 cycles. Weld currents, ranging from 8 kA to 8.8 kA, resulted in undersized welds, and weld current beyond 10.8 kA caused expulsion at the faying surface. Weld currents between 8.8 kA and 10.8 kA produced acceptable-sized welds.

By combining the physical characteristics of DR curve, remarkable differences were observed in thethree classes. Undersized welds did not display an apparent trough α and peak β, suggesting that minor local melting and inadequate nugget formed. The tendencies of acceptable sized welds precisely resembled the typical DR curve of mild steel in RSW, as reported by Dickinson [38]. Noticeably, the endpoint value of the acceptable sized weld was substantially smaller than that of the undersized weld. This trend showed that DR significantly decreased during Stage III owing to successive expansion of the nugget diameter. Two modes of expulsion were observed in the DR curves, early expulsion and late expulsion. Early expulsion is clearly indicated by the remarkable drop in DR shown in Figure 4.5, because the ejection of molten metals induced a substantial reduction in contact area. Late expulsion usually occurred in the last few half cycles of the welding phase. The DR curve of the late expulsion was quite

different from that of early expulsion. However, the features extracted from the DR curves did not vary significantly.
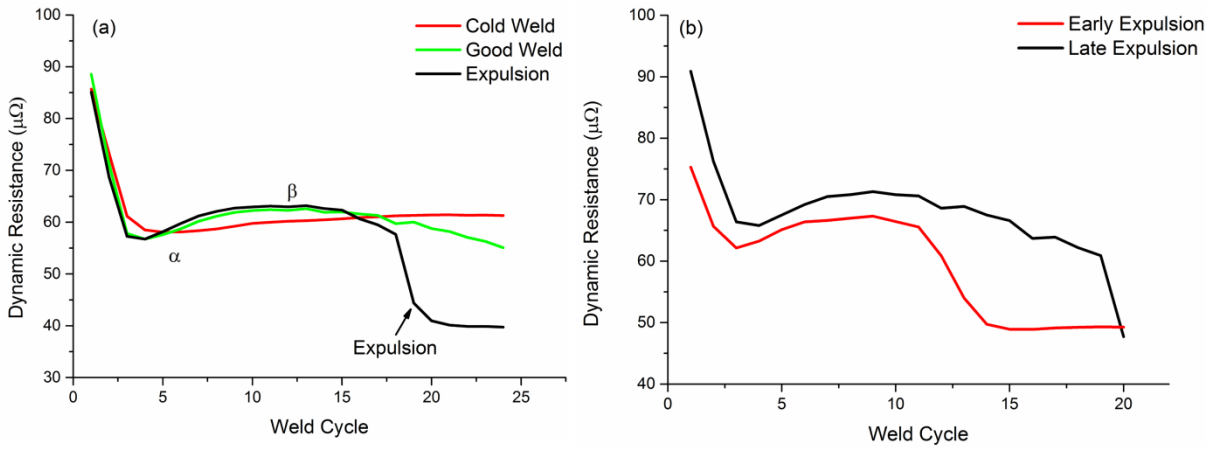
Figure 4.5 (a) Representative DR curves for three levels of joints at 12 weld cycles. (b) Representative DR curves of early expulsion and late expulsion at 10 weld cycles
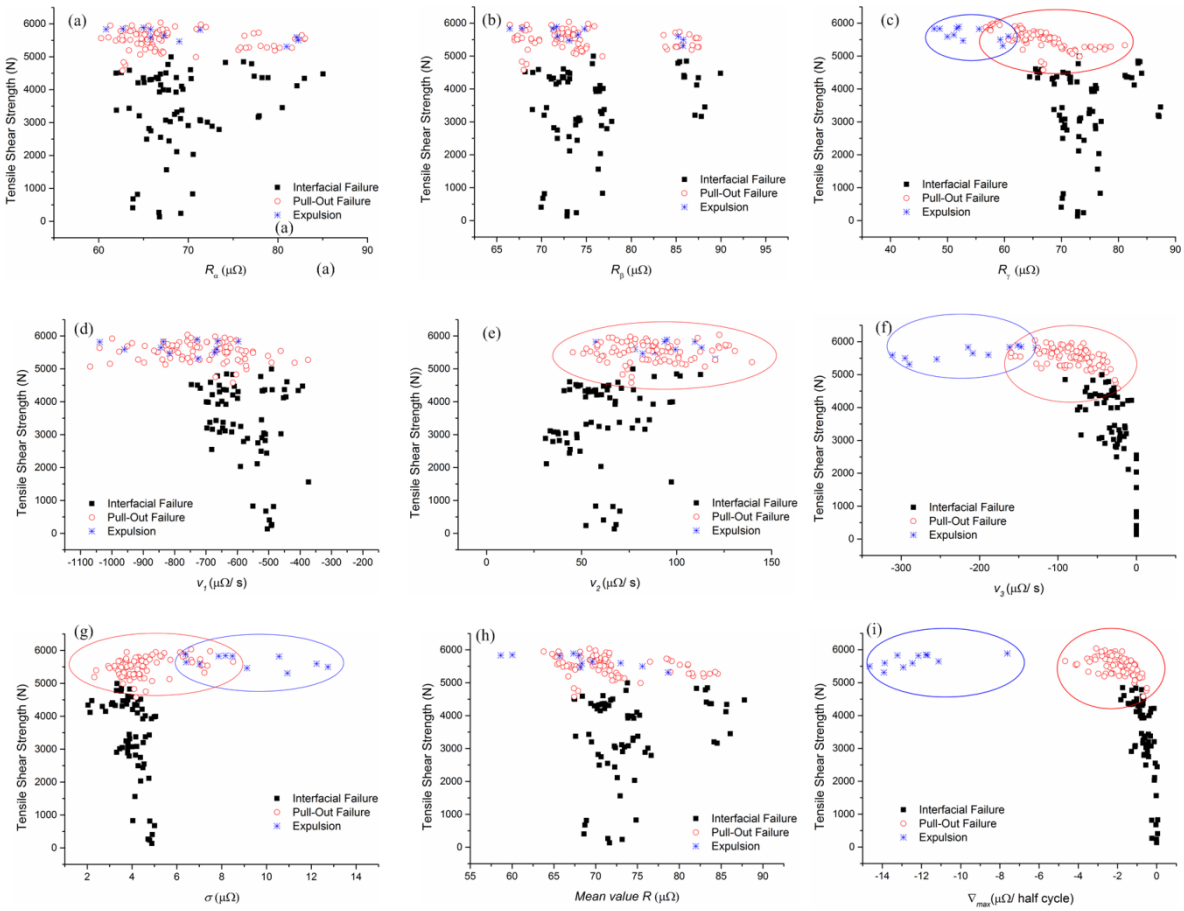
Figure 4.6 Scatter plots of DR features and tensile shear strength

The relationship between DR features and the tensile strength of the joints is shown in Figure 4.6. The dot colors are based on the failure modes. The plots of R_α, R_β, v_1, v_2 and $\bar{R}$ give good insights into the difference in heat generation between undersized and acceptable-sized welds, where they are located in two different regions. In addition, the plots of v_3, σ, and ∇_{max} show that three types of welds quality were found in different regions based the profile feature. The overlapped regions in Figure 4.6 indicate the potential misclassification in the constructed system, as that sole profile feature does not distinguish well between the two failure modes.

Prior to training, correlation analysis among extracted characteristics was adopted to evaluate weather sufficient parameters were extracted. A correlation coefficient approaching 1 or -1 shows strong linearity between two variables; a correlation coefficient approximating 0 implies a weak relation between two variables. Correlation of 0.6 and above indicates a strong correlation.

The inter-item correlation analysis among the input variables is shown in Table 4.1. R_α, R_β, and $\bar{R}$ were found to have strong correlations with each other and showed very weak correlations with three gradients. R_γ and v_3, on the other hand, had a strong relationship with each other. In addition, the three gradients for asperity collapse, nugget nucleation, and nugget growth had no significant correlations with each other. An increase in Stage II did not necessarily imply a well-formed nugget. For undersized welds, the values of v_3 were negligible. The overall gradient in Stage III v_3 and the maximum absolute gradient ∇_{max} shared strong correlations, associated with the sudden decline of expulsion. The standard deviation σ showed a strong inverse correlation with R_γ. This phenomenon could be understood by considering the response of the DR curve to expulsion. When expulsion occurred, a sudden drop in DR was observed, leading to a significant increase in σ.

Table 4.1 Inter-variable correlation matrix

Variables	R_α	R_β	R_γ	v_1	v_2	v_3	$\bar{R}$	σ	∇_{max}
R_α	1.00	0.95	0.48	0.18	0.23	-0.33	0.89	0.23	-0.26
R_β	0.95	1.00	0.58	0.11	0.40	-0.28	0.94	0.16	-0.19
R_γ	0.48	0.58	1.00	0.31	-0.06	0.55	0.77	-0.51	0.59
v_1	0.18	0.11	0.31	1.00	-0.42	0.33	0.16	-0.24	0.22
v_2	0.23	0.40	-0.06	-0.42	1.00	-0.48	0.26	0.24	-0.33
v_3	-0.33	-0.28	0.55	0.33	-0.48	1.00	-0.04	-0.68	0.89
$\bar{R}$	0.89	0.94	0.77	0.16	0.26	-0.04	1.00	-0.12	0.08
σ	0.23	0.16	-0.51	-0.24	0.24	-0.68	-0.12	1.00	-0.83
∇_{max}	-0.26	-0.19	0.59	0.22	-0.33	0.89	0.08	-0.83	1.00

4.3 Construction of RF classifier based on DR curves

The RF method requires users to provide the number of trees *ntree* and the number of features to be used at each node *mtry* prior to the implementation. The choices of *ntree* and *mtry* substantially affects the accuracy of the model. Here, the influence of parameter sensitivity on the RF results was examined. In this work, nine features ($M = 9$) were extracted from the DR curves, and the optimal value of *mtry* should approximate to $\sqrt{M}$ in classification [140]. The *OOB* errors of RF models utilizing *mtry* ranging from 1 to 6 and *ntree* from 10 to 10000 were compared. By using the bootstrapping process, each tree was planted based on a different sample set from the training set. Test data, independent of the training set, were later utilized for prediction based on the constructed models.
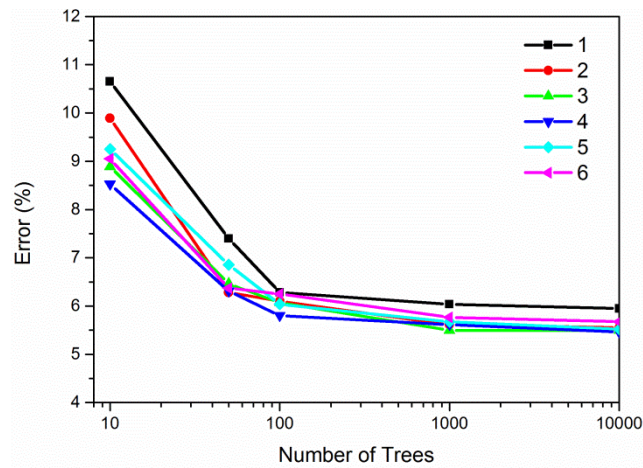
Figure 4.7 Summary of the influence of *ntree* and *mtry* on *OOB* misclassification error

(%)

The summary of the influence of *ntree* and *mtry* on *OOB* errors is presented in Figure 4.7. It is clearly seen that the selections of *ntree* and *mtry* had a pronounced effect on *OOB* errors. The accuracy of classification was strongly dependent on the number of trees in the ensemble, and the smallest *OOB* error was achieved by an ensemble of 10000 trees. In contrast, the ensembles of 10 - 100 trees tended to generate much higher *OOB* error rates. For the number of features considered at each node, *mtry* of 4 produced the most appealing performance compared to other selected values. With consideration of all circumstances, a RF model with *ntree*=1000 and *mtry*=4 was constructed for the DR curves. A typical confusion table of the RF employed is presented in Table 4.2. The individual misclassification rates for undersized welds, expulsion and acceptable-sized welds were 3.4%, 0%, and 8.5%, respectively. Misclassification of acceptable sized welds into undersized welds accounted for most of the errors made by the classifier. Based on the TST, some joints had a failure load close to the peak load of PF mode with low EF applied; however, they still failed in IF mode. Such samples could not be clearly distinguished.

Table 4.2 Confusion matrix for one attempt of training data in random forest classification (*ntree*=1000, *mtry*=4). Columns stand for predicted class and rows stands for original judgments.

	Undersized welds	Expulsion	Acceptable sized welds	Classification Error (%)
Undersized welds	111	0	4	3.4
Expulsion	0	15	0	0
Acceptable sized welds	9	1	108	8.5
Classification rate		94.4%		
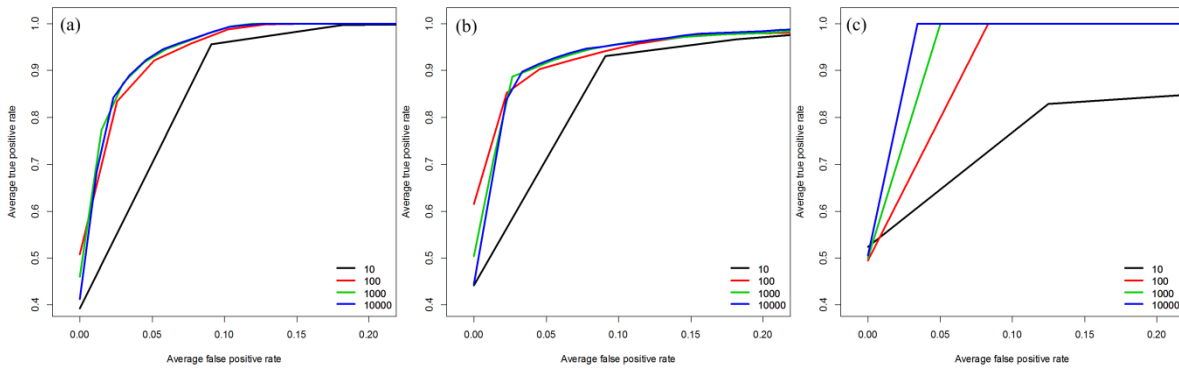
Figure 4.8 Enlarged ROC curves based on the influence of *ntree*. (a) IF. (b) PF. (c) Splash.

Figure 4.8 shows the average ROC curves of classifiers with varied *ntree* from 10 to 10000, using the test dataset. Because ROC was specified for a binary classification problem rather than the multiclass classifier, a "One-vs-All" approach was adopted to generate ROC curves [144]. The area under the curve (AUC) of the multiclass classifier was calculated as

$$AUC = \frac{AUC_{IF} + AUC_{PF} + AUC_{Expulsion}}{3}$$

(4.1)

A higher value of *ntree* allowed greater AUC in all three classes, where a greater AUC suggested a good classifier. AUCs for *ntree* of 10, 100, 1000 and 10000 were 0.9890, 0.9926, 0.9931 and 0.9932, respectively. The increment in AUC from 10 to 100 trees outperformed the increments from 100 to 10000 trees. Moreover, the AUCs of the PF classification were the lowest among the three classifiers, suggesting remained misclassification of PF into other classes.

The 10-fold cross-validation *(*CV) misclassification and test prediction error are compared in Figure 4.9 (a). The average prediction error and the error induced by cross-validation are 6.4% and 7.6%, respectively. The RF model based on DR profile quantity did not overfit. To further reduce the misclassification error between good welds and undersized welds, three welding parameters (WC, WT and EF) were added into the RF classifier. Ten independent sets of training and tests were carried out with the RF parameters unchanged, as schemed in Figure 4.9 (b). It is clear that both CV error and test error declined significantly from the results relying on DR signals. Significant improvements in cross-validation error and prediction error were obtained. The average cross-validation error (1.4%) was slightly greater than the test error (1.2%), indicative of no overfitting for the constructed models. The inclusion of weld parameters was proven to effectively optimize the classification rate.
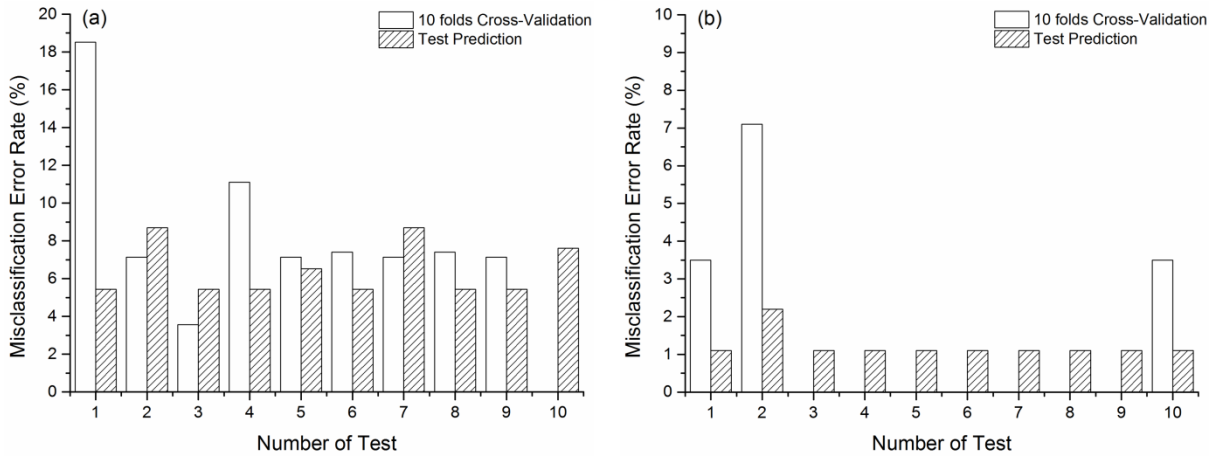
Figure 4.9 Comparison of test error and CV error based on (a) DR signals (b) DR and weld parameters

4.4 Variable importance evaluation of the RF classifier

The variable importance of extracted DR features was investigated via permutation accuracy importance (PAI) [140]. Estimations of variable importance give a good indication for ranking the relative importance of input features in constructing the ensemble of decision trees. For the k_{th} tree $h_i\{X\}$ (i=1,2…k) built in the forest, a unique bootstrapping data and out-of-bag data was created. The classification is employed based on the *OOB* data and the count of the accurate classification R_b^{OOB} is estimated accordingly. For an *ntree* model, the out-of-bag error rate is determined. Then, the feature m_i (i=1,2…M) used in the data set is randomly permuted once per time and the procedure in building a RF and estimating the *OOB* error is repeated based on the newly permuted variables. The importance measures D_j for variable m_i and z-score are given by:

$$D_j = \frac{1}{M}(R_b^{OOB} - R_{bj}^{OOB})$$

(4.2)

$$z_j = \frac{D_j}{s_j \sqrt{M}}$$

(4.3)

where s_j is the standard derivation of the decrease in classification of undistorted data. Then, z_j is transformed into a significance value based on the assumption of Gaussian distribution.

Variable importance evaluation of two optimum RF classifiers was carried out. The mean decrease in accuracy indicated the significance of the variables after permutation of the values. From Table 4.3, it is observed that four features R_γ v_2, v_3 and ∇_{max} extracted from DR had the most significant impact on decision-making for the DR based RF classifier. On the basis of the mean decrease in accuracy value, other five parameters were less important Recall from the inter-item correlation analysis, that v_3 and ∇_{max} had strong inter-correlation. Hence, both were found to play crucial roles in classifying weld quality. It is intriguing that the independent slopes v_2 and v_3 were influential for RF classifier accuracy. When sufficiently large current was transmitted through the workpieces, asperity collapse occurred that increased the contact area. The large gradient of v_2 implied that the heat input resulted in a substantial film breakdown with an enlarged contact region and local melting at the faying surface. Moreover, a descending trend (significant v_3 and ∇_{max} and small R_γ) in DR during nugget growth indicated an inverse relationship with the final nugget diameter. Expulsion accounted for the precipitous decline in DR, and contributed to a much smaller R_γ compared to those of good welds. Factors like R_α, R_β and v_1 were more closely related to the initial surface condition and contact status of the faying surface, rather than the nugget growth and development in Stage II and III.

In Luo's work, it was straightforward to adopt the relative averaging value of DR to distinguish weld quality [71]. Unlike the existing approach in differentiating the weld quality, good welds and poor welds showed minimal difference in the average values $\overline{R}$ and standard derivation σ in the DR curves. That finding might result from different

approaches for calculating the DR values. Similarly, Wan adopted PCA on discrete points on the DR curves [74]. Five principal components selected over PCA, accounted for over 99.6% of the original DR signal, and the first component (PC1) registered the accountability proportion of 78.3%. However, the actual physical meanings of the principal components extracted from the curves were difficult to interpret. When undersized welds were produced in the production line, any indication from the derived principal components was limited. In contrast, R_γ v_2, v_3 and ∇_{max}, the most significant variables of RF, allowed users to examine the actual history of nugget development and to take actions to avoid producing further undersized welds. Moreover, to adopt PCA with varied welding time, users needed to ensure the same dimensionality as the original data. The result generated might poorly differentiate the significance of welding time, that needed to be corrected by inputting the actual weld time into the model.

In the use of DR and the weld parameter based RF classifier, the values of WC became the most important factor in determining the classification accuracy, over the four features R_γ v_2, v_3, and ∇_{max}. WT and EF were considered less important features for the classification, due to the relatively narrow range of values compared to that of weld current and minor contribution based on Joule's equation.

Table 4.3 Variable importance of extracted features from DR curves

DR	Mean Decrease in Accuracy	DR and weld parameters	Mean Decrease in Accuracy
R_α	23.26	R_α	14.58
R_β	16.17	R_β	11.81
R_γ	50.18	R_γ	29.58
v_1	29.43	v_1	18.16

v_2	53.47	v_2	34.00
v_3	50.03	v_3	33.48
$\overline{R}$	20.57	$\overline{R}$	14.79
σ	21.41	σ	18.21
∇_{max}	58.42	∇_{max}	42.35
~	~	WC	77.26
~	~	WT	15.65
~	~	EF	9.23
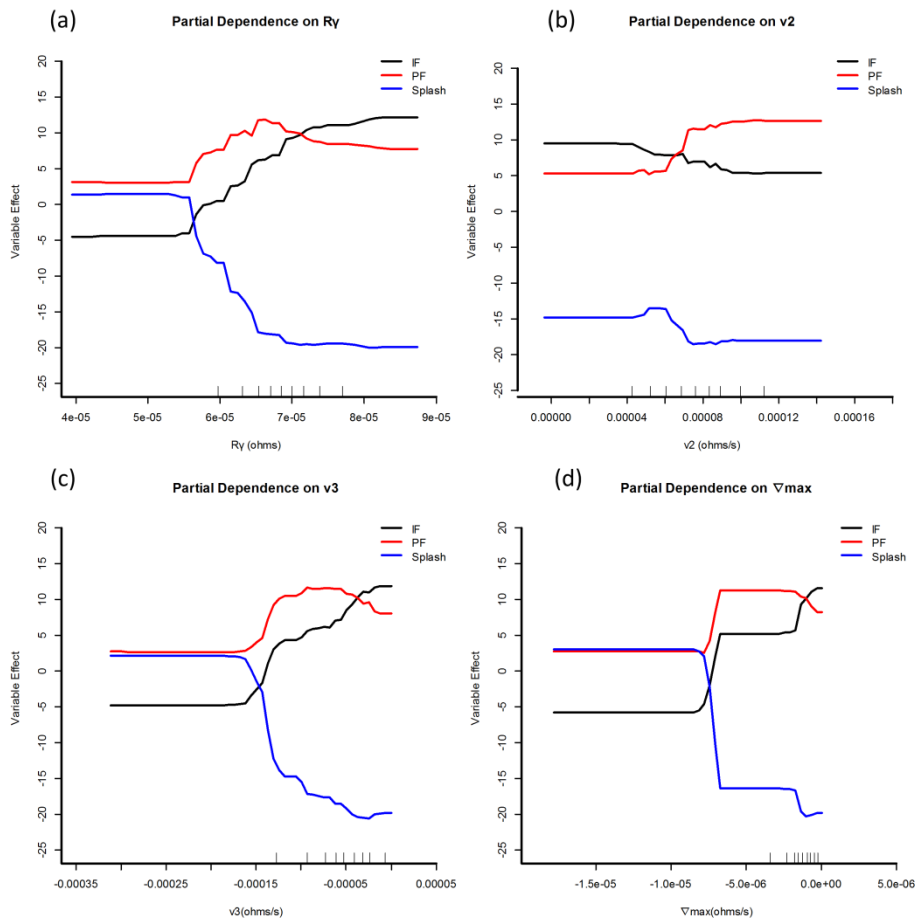
Figure 4.10 Partial dependence plots of significant features. (a) R_γ. (b) v_2. (c) v_3. (d) ∇_{max}.

The partial dependence of significant features on the classification probability was also investigated via the R language "partial plot" function [142]:

$$\tilde{f}(x) = \frac{1}{n}\sum_{i=1}^{n} f(x, x_{ic)}) \tag{4.4}$$

$$f(x) = \log p_k(x) - \frac{1}{K}\sum_{j=1}^{K} \log p_j(x) \tag{4.5}$$

where x is the variable of interest and x_{ic} is the other variables in the data, K is the number of classes, k is the class to be investigated, and p_j represents the fraction of the vote for j. A positive value in $\tilde{f}(x)$ increases the probability of the corresponding class, and vice versa.

Here, the partial dependences of previously discussed features on three weld classes are presented in Figure 4.10. For R_y, v_3 and ∇_{max}, they show nearly identical plots although the corresponding x values are different. To isolate expulsion from the other classes, the feature values needed to be smaller than the threshold values, that were 5.5e-05 Ω, 1.8e-04 Ω/s and 0.75e-05 Ω/s, respectively. Moreover, the classification of IF and PF mode was achieved by the intersection point in each sub figure, as shown in Figure 4.10. When greater variable effect of PF mode was located between 5.5 e-05 Ω and 7.2 e-05 Ω, R_y was more likely to predict the weld quality as PF mode. On the other hand, v_2 displayed an opposite trend in distinguishing IF and PF mode, while the impact of the variable on expulsion remained negative. This finding suggested that v_2 had a negligible connection with the phenomenon of expulsion, and failed to solely predict expulsion because it accounted for nugget growth velocity in Stage II.

4.5 Shunting effect in DR curves

In this section, two types of spot welds were considered: making spot welds on the same sheet and making every spot weld on new sheet metal. The former joints resembled the

production sequence in the plant environment. The latter joints, on the other hand, were prepared into the tensile shear specimens and provided an indication of weld quality at that welding schedule. However, the spot welds on the same sheet gave rise to shunting effect. Though identical welding parameters were applied to the group of welds, the differentiation in contact status between the faying surface and workpiece/electrode surface and shunting current could result in different DR curves. The shunting current effect is usually considered the predominant influence for the quality of continuous welds and the resulting quality control system, where the resulting DR of continuous welds (shunted weld) might be lower than that of the first weld on the workpiece (shunt weld), according to the equation:

$$R_{DR} = (R_w \times R_s) \Big/ (R_w + R_s)$$

(4.6)

where R_{DR} is the resulting DR derived by measured voltage and current, R_w is the effective resistance of the weld path, and R_s is the effective resistance of the shunting path, which is proportional to the weld spacing. In this study, however. the weld spacing was equal to the minimum distance for mild steel (20 mm) [120]. DR curves of the shunt and shunted welds are compared in Figure 4.11. It is clearly seen that the difference in DR values was significant at Stage I between the shunt and shunted welds and the difference in DR values become smaller in Stage II and III. Moreover, in the basis of Equation (4.6), it was inevitable that the values of $\bar{R}$ for shunted welds were smaller than those of the shunt welds.
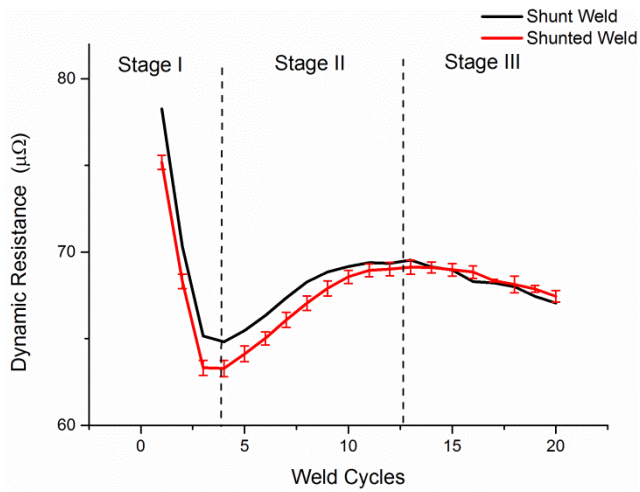
Figure 4.11 Shunting effect in DR curves (Weld spacing equals 20mm)

To investigate the influence of shunting, another DR based RF classifier was constructed (*ntree*=1000, *mtry*=4), with all shunted weld excluded from the original data source. In total, 228 samples were used. The resulting confusion matrix plotted in Table 9, however, did not show any significant improvement in classification accuracy (about 92.6%). From the partial dependence shown in Figure 4.12, the variations in R_α and v_1 and $\overline{R}$ did not substantially affect the probability of classification within the varying range. Hence, after excluding all shunted welds, the improvement in accuracy was negligible. In this case, the continuous welds with weld spacing beyond the minimum values (20 mm for mild steel) did not significantly affect the classification accuracy. Wen's work revealed the inverse relationship of nugget diameter and endpoint value of the DR curves of stainless steel and the DR curves of weak and severe shunting [64]. Shunting proportionally decreased the endpoint value of DR values with weld spacing, making it inconsistent with the previous relationship found with nugget diameter. Thus, this finding implied that the RF classifier might have difficulty in distinguishing undersized welds due to severe shunting in continuous welds if no more information was provided.
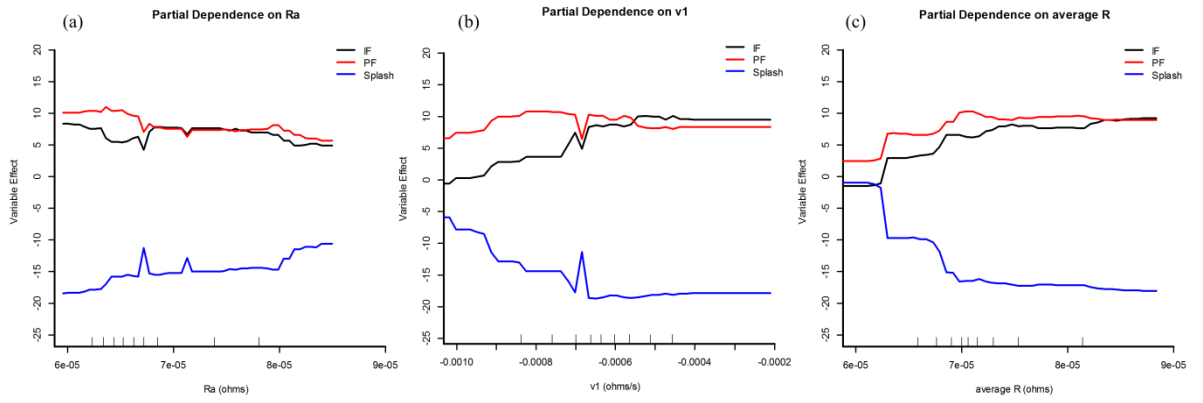
Figure 4.12 Partial dependence plots of significant features. (a) R_α. (b) v_1. (c) $\overline{R}$.

Table 4.4 Confusion matrix for DR curves without shunted welds in random forest classification (*ntree*=1000, *mtry*=4). Columns stand for predicted class and rows stands for original judgments.

	Undersized welds	Expulsion	Acceptable sized welds	Classification error (%)
Undersized welds	83	0	7	7.7
Expulsion	0	21	1	4.5
Acceptable sized welds	8	1	106	7.8
Classification rate			92.6%	

4.6 Summary of construction of RF-based online monitoring system

The RF classifier was adopted for a selected dynamic signal, DR, in the RSW process. Three levels of weld quality were considered as classes in this study, namely undersized weld, acceptable sized weld, and expulsion. The values of *ntree* and *mtry* substantially affected the performance of the classifier, as revealed via *OOB* error and AUC. The preliminary results showed that RF could provide a satisfactory classification (~93.6%) based on the DR profile quantities. The introduction of weld parameters into the classifier substantially improved the predicted classification accuracy (98.8%). Using variable importance evaluation by RF, four features from DR profiles and weld current were considered to be the most important for the classifiers, information that was not available from other black-box models. However, v_2 provided little information in classifying expulsion compared to the rest of the features. Issues were also identified regarding the RF classifier. The misclassification of good welds into cold welds was predominant, a feature that still required interpretation by a human operator. Shunted welds with sufficient weld spacing did not significantly undermine the accuracy of the RF classifier. Further work on severe shunting is expected, where the key profile

features and the actual nugget size might be substantially affected. The RF-based monitoring system is proposed to evaluate weld quality on the production line.

Chapter 5 Monitoring abnormal process conditions in RSW

The weld quality of a spot weld is indicated by the weldability lobe, in which a group of welding parameters determine heat input and thus nugget size. Nonetheless, a range of abnormal process conditions in the plant environment can affect weld quality, even when proper welding parameters developed from normal process conditions are used. It is important to differentiate the welds under these abnormal process conditions from good welds, using an online monitoring system. From the previous section, the DR tends to be affected by a severe shunting effect, from which inconsistencies between key profile features and actual nugget size can be derived. Thus, DR and ED are compared, where shunting, poor fit-up of parts, close-to-edge welds are primarily investigated.

5.1 Signal processing in dynamic signals

5.1.1 Electrode displacement

Examples of original and de-noised ED signals are presented in Figure 5.1. The ED occurred in three stages: squeeze, weld, and hold. ED signals were collected when two electrodes were in contact during the squeeze stage. The signal showed no fluctuation in the squeeze stage. In the welding stage, the welding current flowed through the base materials, and the base metals began to melt, induced by Joule heating. The thermal expansion and solid-to-liquid phase transformation together accounted for the total ED in the welding stage. Strong vibration, similar to the vibrations reported in Wang's work [58], was found to accompany the elevated displacement, stimulated by the AC power source. The frequency of the oscillating signal of the ED was around 100 Hz, twice that of the spot welder. Electrode force was applied to the steel in the hold stage. The molten metal experienced rapid cooling through the water-cooled electrodes, resulting in a

gradual decline in ED. The collected signal was further processed through a low-pass filter to eliminate the frequency components arising from electrode vibration. The de-noised signal shown in Figure 5.1 (a) precisely describes the equivalent ED.
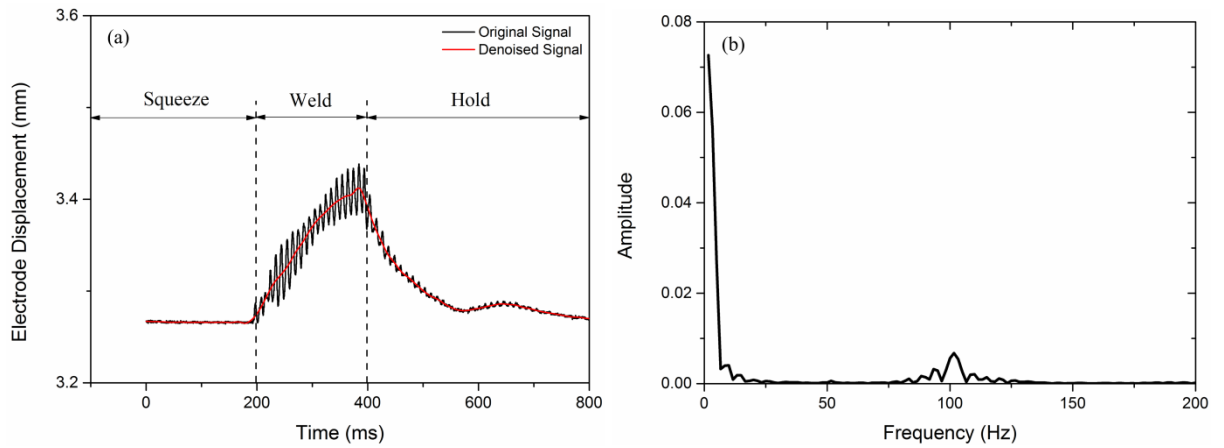
Figure 5.1 (a) Electrode displacement in the time domain. (b) frequency spectrum of electrode displacement

5.1.2 Dynamic resistance

The root-mean-square DR was calculated every half cycle via Equation (3.1). Due to the small sampling size, no significant oscillation was observed in the DR curve. Thus, no signal processing was done for the DR curves.

5.2 Shunting effect

5.2.1 Effect of welding current on ED

The shunting effect is known as a phenomenon in which the welding current for a brand-new weld is diverted by existing welds in the same area. It is important to determine the welding current that produces shunt welds.
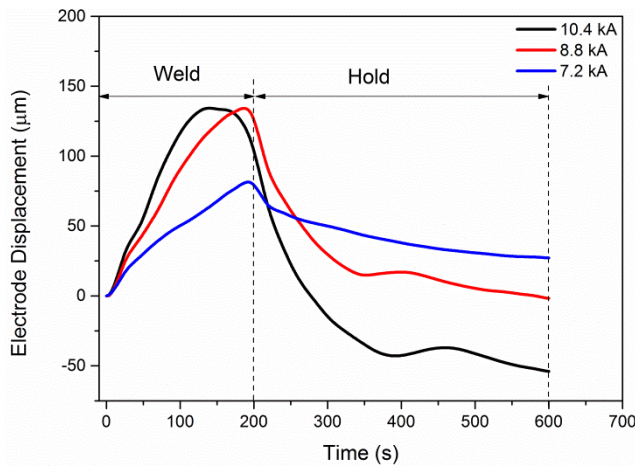
Figure 5.2 Effect of welding current on electrode displacement

The EF of 2700 N and the welding time of 200 ms were used. Cold welds were produced with the welding current of 7.2 kA, whereas good welds were produced with the welding current of 8.8 kA. The welding current of 10.4 kA was the upper limit without expulsion. Figure 5.2 demonstrates the ED signals with different weld currents. Significant variations in ED profiles are seen. The lowest peak value is located in the ED curve for a cold weld that has a gentle slope in the welding stage. The base materials began to melt and form a nugget, but the heat input was insufficient for yielding an adequate-sized nugget. When an acceptable sized weld was made, a much higher ED peak value was generated, and a moderate electrode velocity was achieved. However, no marked increase in peak value was found for welding currents from 8.8 kA to 10.4 kA. Further thermal expansion was constrained by the limited electrode geometry [57]. Therefore, the displacement value did not increase any futher. On the other hand, the ED velocity with the welding current of 10.4 kA outperformed those at lower current levels, as a greater amount of Joule heat was generated by:

$$P = i(t)^2 R(t) \tag{5.1}$$

where $i(t)$ is the welding current, $R(t)$ is the total resistance. Expulsion was likely to occur if

excessive welding current was used, which weakens the mechanical performance of the nugget and aggregates electrode degradation [65]. To investigate the shunting effect, the welding current of 8.8 kA was used in the subsequent welding experiments.

It is worth mentioning that a considerable difference in ED signals in the hold stage was found with respect to different spot weld qualities. Such differences in ED signals could be explained by two methods. Firstly, Lai and colleagues investigated the effect of the indentation mark depth on the weld strength, where the indentation depth was measured by the difference between starting point and end point of the ED signal [145]. They found that the indentation depths of cold weld and expulsion usually sat outside the acceptable weld size range. However, the values in present study were much lower than those established in the study of Lai et.al's. Hence, the endpoint value in present study may not accurately reveal the indentation mark. Alternatively, Jou suggested that the ED signals in the hold stage can reflect solid-state phase transformation [47]. As the level of heat generated was increased, an adequate volume of liquid metal was preserved at the faying surface. When the welding current was terminated, the electrodes clamped on the base material while the molten metal experienced a rapid cooling period via the water-cooled channel on the electrodes. The heat input determined the size of fusion zone, thus leading to the volume change in the hold stage.
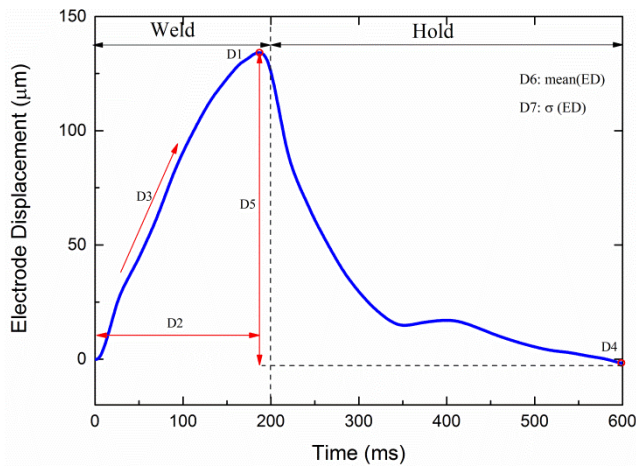
Figure 5.3 Electrode displacement profile quantity extraction in the time domain

Seven profile quantities with physical meanings were extracted from the ED signal in the time domain, as shown in Figure 5.3, in which D1, D2 and D3 correspond to the peak value in ED, the location of the ED peak and ED velocity, respectively. D4 and D5, on the other hand, reflect the endpoint value of the ED displacement and the overall decline between D1 and D4. Lastly, D6 and D7 are the mean value and the standard deviation of the ED signals, respectively.

5.2.2 Effect of welding spacing on electrode displacement
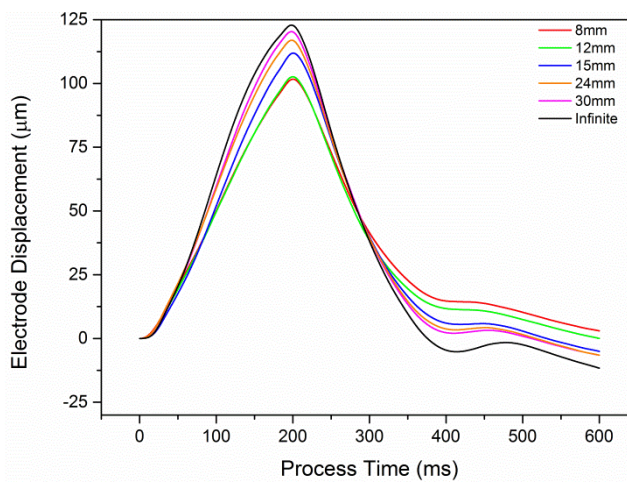
Figure 5.4 Electrode displacement of the single shunted welds at different weld spacing.

98

The ED signals of the averaged first shunted weld at different weld spacings are summarized in Figure 5.4, where the weld spacing ranges from 8 mm to 30 mm. It is noted that, with the decrease in weld spacing, the peak values of the ED signals shift downward and the slopes of the ED in the welding stage decrease proportionally. The shunting path substantially diverted the welding current, resulting in small thermal expansion and gentle ED velocity for the shunted welds. Figure 5.5 shows longitudinal sectional views of the nuggets for various welding spacings. The nugget diameters for shunt welds were nearly identical. Due to the shunting effect, it wasfound that the nugget diameters of the shunted welds were substantially reduced from that of shunt weld with the weld spacing of 8 mm, whereas the decrease in nugget diameter was less evident with larger weld spacings. The relationship between the weld spacing and the nugget diameter of tested samples is shown in Figure 5.6. They were fitted with a polynomial curve, similar to that in the work of Bi [122]. It is known that the acceptable minimum nugget diameter should exceed $5\sqrt{t}$, where t is the thinnest thickness of the base materials. The approximate minimum weld spacing was found to be around 20 mm, as demonstrated in Figure 5.6. Furthermore, the indentation marks in shunted welds with different spacings did not distinctly vary in Figure 5.5, usually around ~150 μm. The indentation depths in Figure 5.4 are ~ 10 μm, calculated based on Lai's work, which did not reflect the actual indentation mark [145].
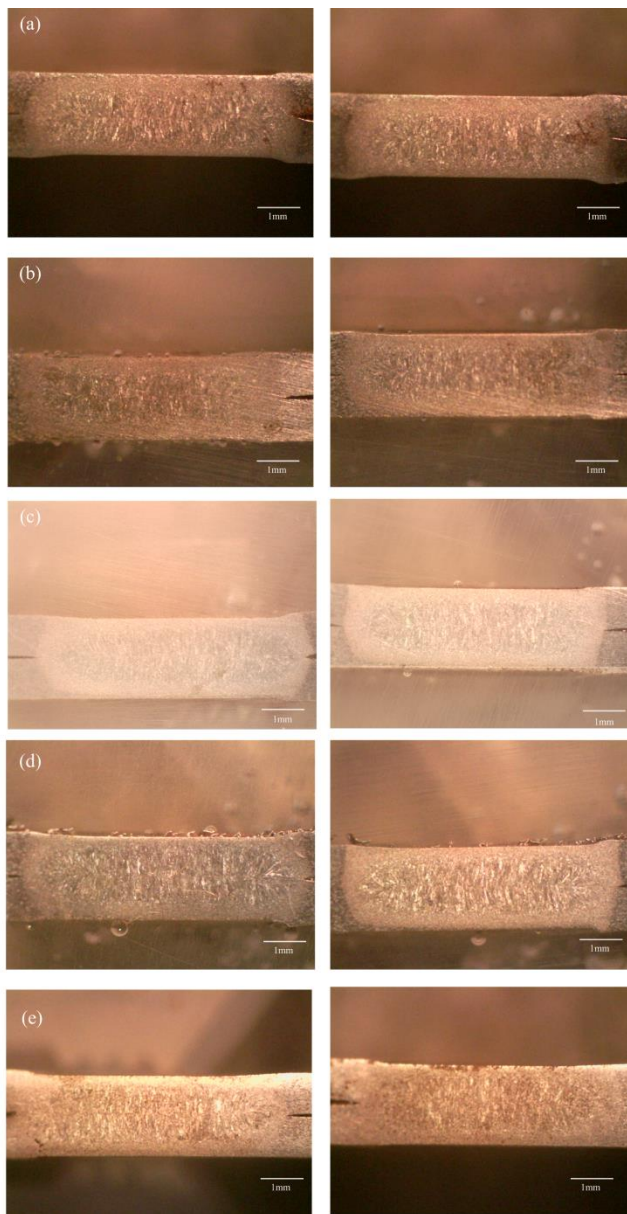
Figure 5.5 Longitudinal-sectional views of shunt welds and first single shunted welds. a) 8 mm. b) 12 mm. c) 15 mm. d) 24 mm. e) 30 mm
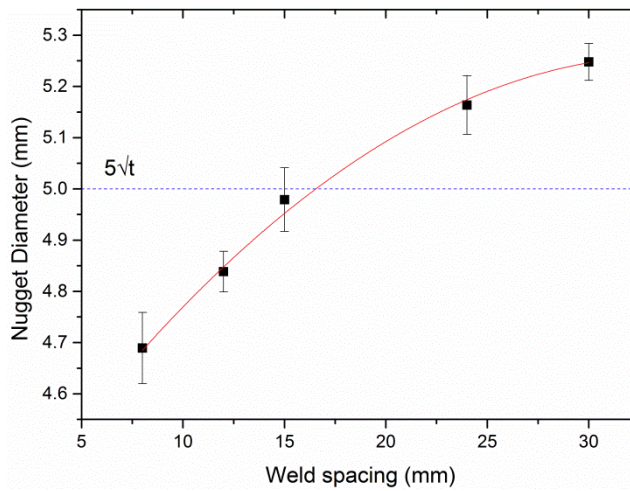
Figure 5.6 Nugget diameters of the first single shunted welds with different weld spacings

The seven ED profile quantities (D1 − D7) with respect to nugget diameters are presented in Figure 5.7. Some of values (D1, D3, D5 and D7) show strong correlation to the nugget diameter, whereas D4 displays an inverse polynomial correlation to nugget diameter. The trends developed among D1, D3, D5, and D7 are similar to each other. D1 and D3, known as the ED peak and ED velocity, are strongly related to the overall magnitude of thermal expansion and the rate of thermal expansion. Both these characteristics played a key role in nugget nucleation and development. Few previous studies have focused on the ED in the hold stage, because the thermal expansion ceases and the molten metal gradually solidifies at this stage. Nonetheless, the indentation mark and liquid-to-solid phase transformation occurred at the hold stage. D5, dependent on D1 and D4, was used to describe the solidification of the fusion zone. A strong relationship was found among the shunted welds in D5, where the volume changed in solidification at the hold stage determined the relative nugget size. Pouranvari disclosed a strong correlation between indentation depth and nugget diameter at various heat inputs [146]. The indentation depth showed a polynomial correlation against the heat input, matching the curves fitted for D4 and D5. On the other hand, D2, the time of ED

peak, did not exhibit any linear relationship with the nugget diameter. It is worth noting, however, that the shunted welds that exceeded the minimum nugget size attained lower D2 values than those of the undersized welds. Shunt welds with sufficiently large weld spacing resulted in significant variance in ED values due to thorough thermal expansion and solidification. Thus, D7, the standard deviation of ED, was related to the nugget diameter. Lastly, the mean value of ED (D6) fluctuated with different weld spacings, making it less useful in detecting shunting problems. Three profile quantities, D1, D3, and D7, could be considered for shunting detection.
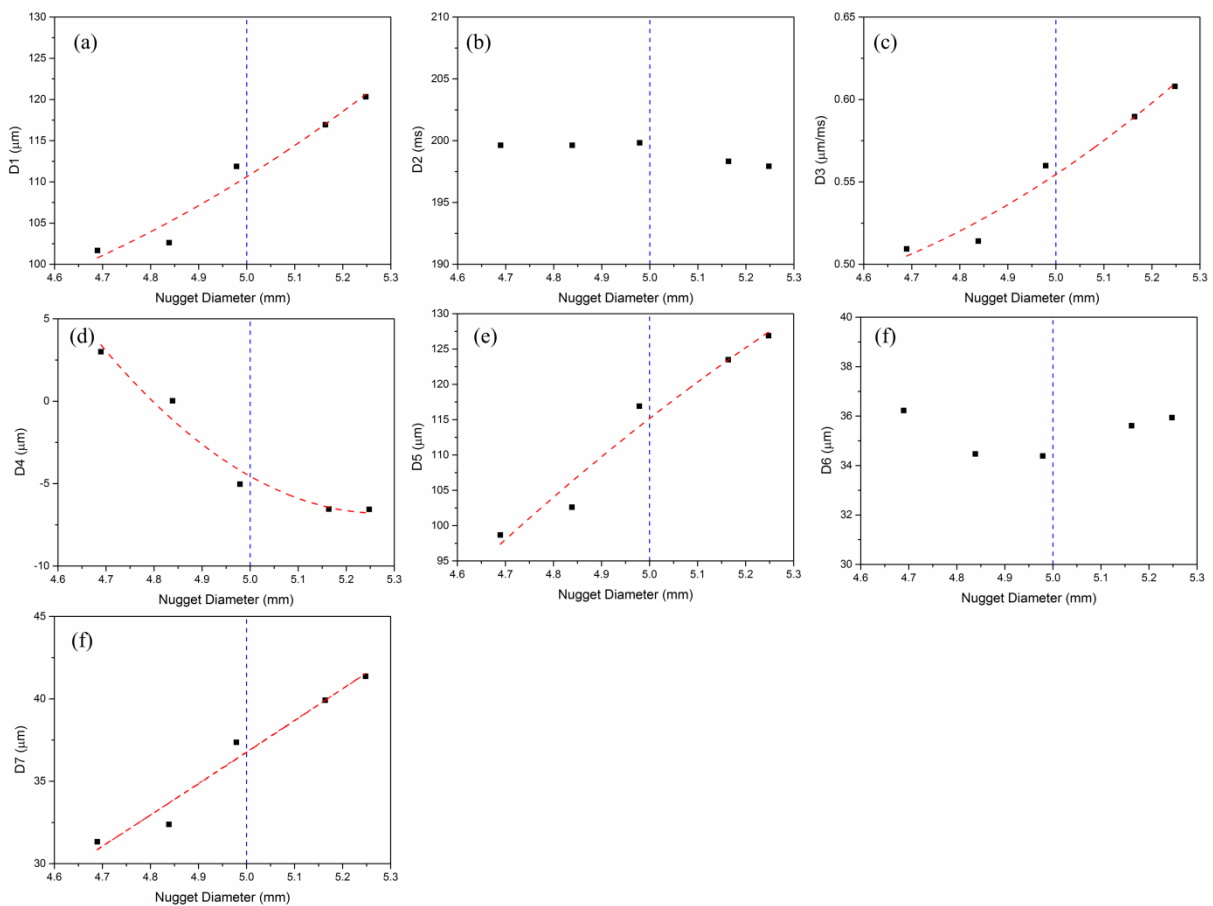
Figure 5.7 Profile quantities of ED signals and nugget diameters with different weld spacing.

5.2.3 Effect of number of shunted welds on electrode displacement

Figure 5.8 presents the impact of double shunting on ED signals. Single shunting and double shunting were implemented via the welding sequences shown in Figure 3.7, with the welding spacing of 8 mm and 15 mm. Double shunting from neighbouring welds led to a significant decline in the peaks of the ED curves illustrated in Figure 5.8 (a) and (b). The peak values of the ED curves with 8 mm weld spacing were lower than those with 15 mm spacing.
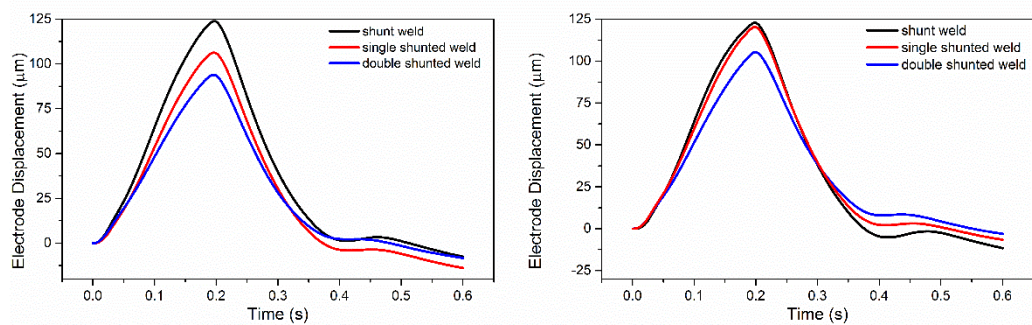
Figure 5.8 Electrode displacement of varied number of shunted welds with weld spacing of (a) 8 mm and (b) 15mm

Figure 5.9 demonstrates some cross-sections of double shunted welds It can be seen that the shape of double shunted welds (2nd) is affected by the existing welds (1st and 3rd). The outline of the double shunted weld is more rectangular than elliptical as that in the case of the shunt weld. The nugget diameters of spot welds are demonstrated in Figure 5.10, in which of the double shunted welds meets the minimum nugget diameter. Hence, the critical double shunting distance should be greater than15 mm.
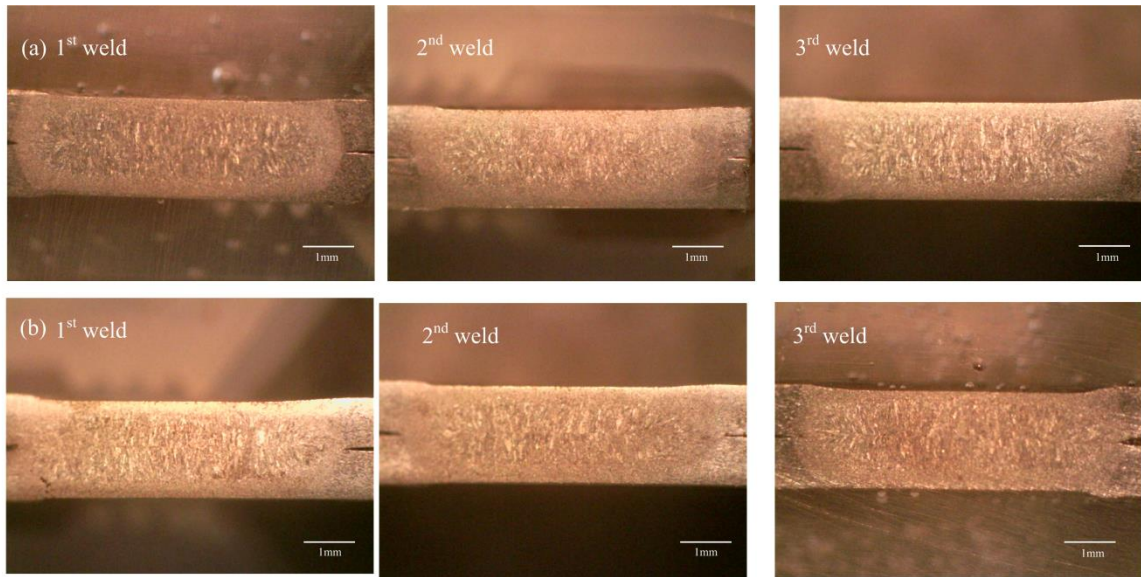
Figure 5.9 Longitudinal-sectional views of the double shunted welds made on a 1-mm mild steel, with weld spacing of (a) 8 mm and (b) 15 mm.
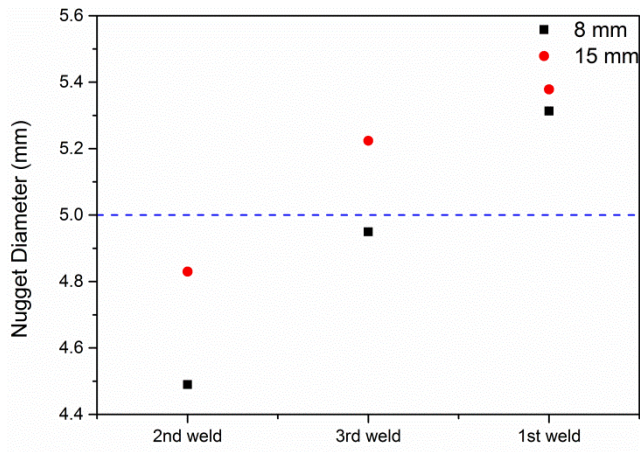
Figure 5.10 Nugget diameters of single shunting and double shunting

(a)

shunt weld
shunt weld
30mm single shunted
16mm single shunted
15mm double shunted
8mm single shunted
8mm double shunted

D1 (µm)
Nugget Diameter (mm)

(b)

shunt weld
30mm single shunted
shunt weld
16mm single shunted
15mm double shunted
8mm single shunted
8mm double shunted

D3 (µm/ms)
Nugget Diameter (mm)

(c)

shunt weld
shunt weld
30mm single shunted
16mm single shunted
15mm double shunted
8mm double shunted
8mm single shunted

D7 (µm)
Nugget Diameter (mm)

Figure 5.11 Relationship of profile quantities and nugget diameters under single and double shunting. (a) D1. (b) D3. (c) D7

Figure 5.11 summarizes the relationship between the profile quantities and the measured nugget diameters under various shunting conditions. It is worth mentioning that D1, D3, and D7 could precisely predict the nugget diameter in double shunting at different weld spacings. Good linear correlations existed among extracted profile features and nugget diameters for the shunted weld. Welds with acceptable sized nugget are circled and are easily distinguished from the shunted welds with undersized nuggets. Double shunted welds generated much smaller nugget diameters than single shunted

welds at the same weld spacing. From Equation (3.6), it is worth mentioning that the additional shunt weld diverts a substantial portion of the welding current and produces an undersized weld.

5.2.4 Comparison with dynamic resistance signal

Many studies have built weld quality monitoring systems based on DR signals of the single weld [64, 71, 147]. They have identified that, for the single weld, the DR curves varied with respect to welding parameters and could be utilized for quality monitoring via their endpoint and mean values. Spot welds with large nugget diameters usually have lower mean values and end point values than those with small nugget diameter. In this study, dynamic resistances with shunting was measured at different weld spacings ranging from 8 mm to 30 mm. The DR signals of single shunted welds and double shunted welds are demonstrated in Figure 5.12(a) and Figure 5.13 (a) and (b), respectively. For single shunted welds, the bulk resistance in shunting $R_{b,s}$ was proportional to weld spacing. The ratio $(R_{b,w} + R_{f,w})/ R_{b,s}$ declined under increased weld spacing. The DR of shunted welds, equivalent to the total resistance in Figure 3.7 (b), tended to decrease with increased weld spacing, in accordance with Equation (5.2). As a consequence, DR curves were found to shift downward with the decrease in weld spacing.

$$R = 2R_{ce} + \frac{R_{b,s}(R_{b,w} \times R_{f,w})}{(R_{f,w} + R_{b,s} + R_{b,w})} \tag{5.2}$$

Like the above characterization of ED signals, the mean value of DR against weld spacing was first derived from the DR curves. The relationship between nugget diameter and the mean DR value is established for a single shunted weld, as shown in Figure 5.12 (b) and (c), from which strong correlations were found. Likewise, the mean DR value in double shunting is illustrated in Figure 5.13 (c) and (d). It is notable that

106

the contribution of the shunted path to total resistance has been doubled with two existing welds, causing the associated DR curve to decline. The findings in the comparison between singl and double shunting validated that DR signals were sensitive to the additional parallel circuit caused by shunting. The existing quality monitoring system, based on the DR signals of single welds, was found to make little contribution to characterising the quality of welds accompanied by severe shunting [64]. It is likely that inaccurate results for shunted welds could be obtained from DR signals.
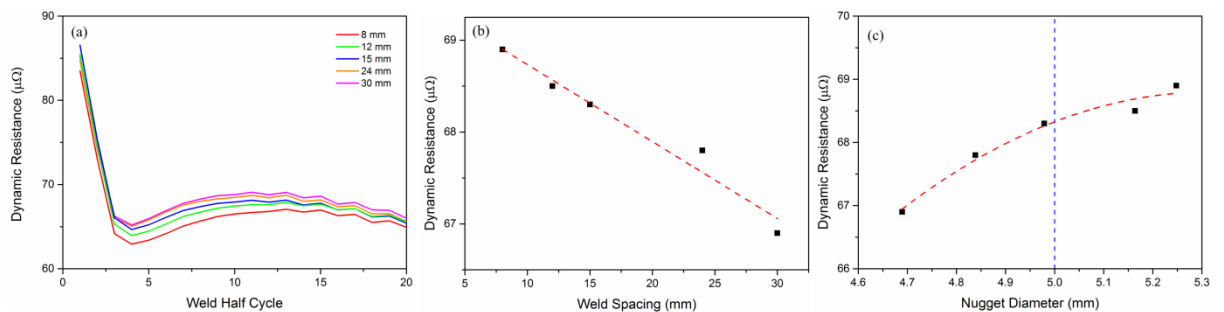
Figure 5.12 (a) Dynamic resistance of first shunted weld with different weld spacings. (b) mean values of dynamic resistance at different weld spacings. (c) mean values of dynamic resistance against nugget diameters.
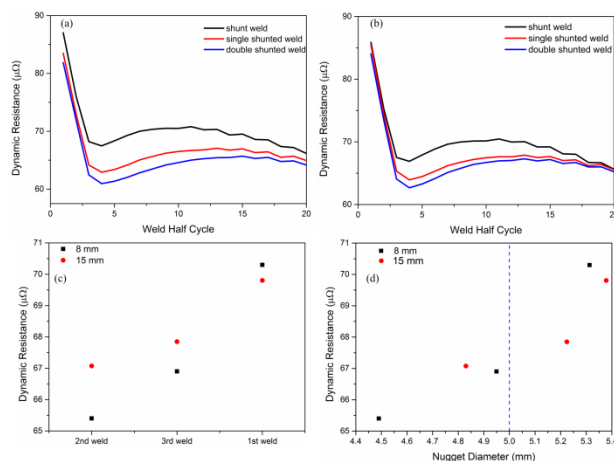
Figure 5.13 Dynamic resistance of double shunted welds with weld spacings of (a) 8 mm and (b) 15 mm. (c) mean values of dynamic resistance in double shuntings. (d) mean values of dynamic resistance against nugget diameters.

5.3 Poor fit-up problem

The above study of shunting effect did not address the influence of mechanical deformation of the base metals. When a shunted weld is made, the welding current is diverted from the shunt path, and an air-gap is generated due to the deformation resulting from the EF. This study considered two airgap types from distinct weld sequences, such as the single-sided and double-sided gaps in Figure 5.14. It can be seen that noticeable air-gaps were formed after the spot welds were made at the center of the sheet metal.
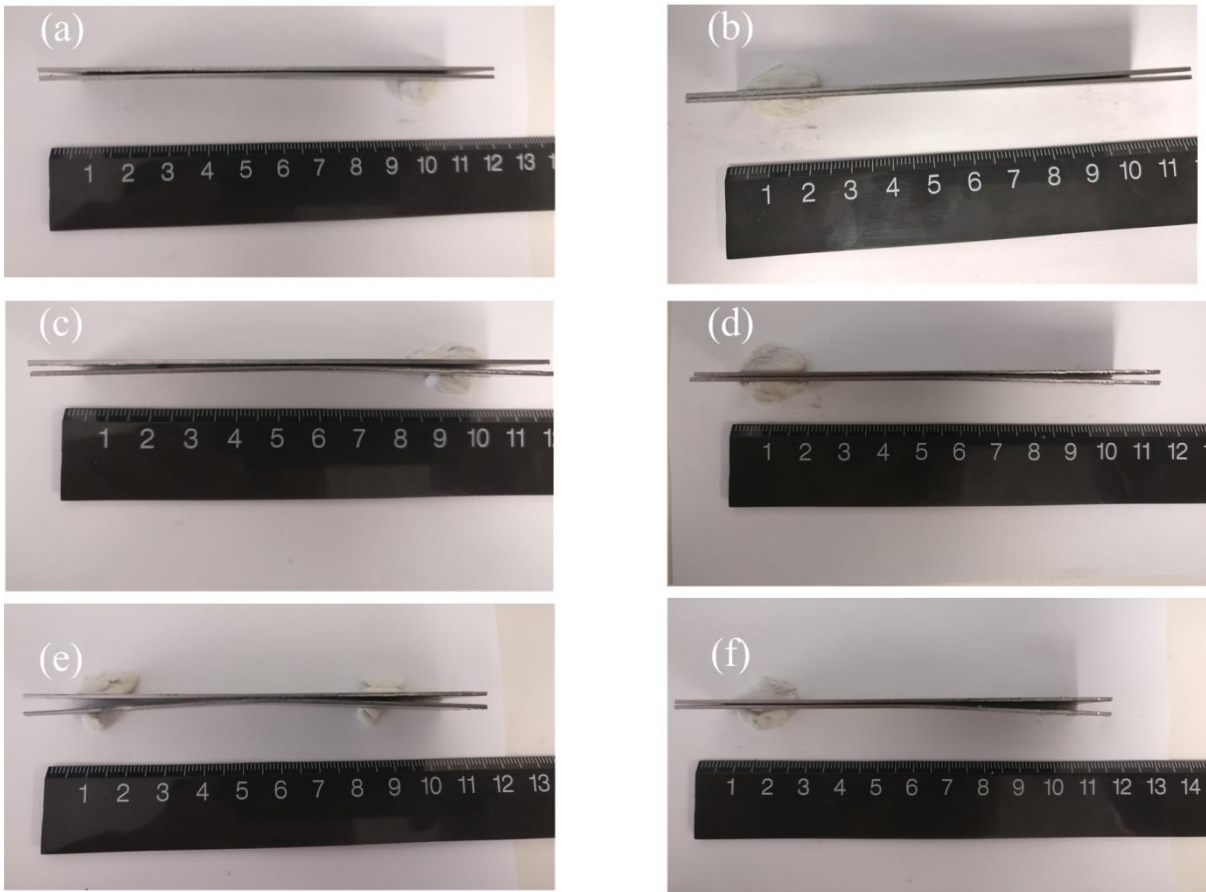
Figure 5.14 Welds with poor fit-up problems. (a) 0.5 mm double gap. (b) 0.5 mm single gap. (c) 1 mm double gap. (d) 1 mm single gap. (e) 2 mm double gap and (f) 2 mm single gap
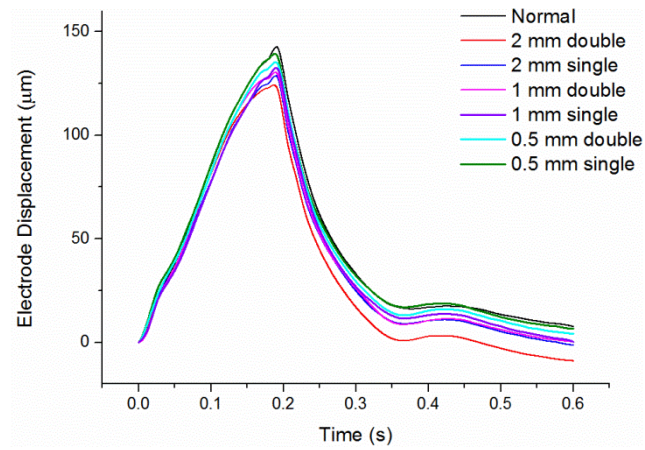
Figure 5.15 Electrode displacement curves of different poor fit-up intensity
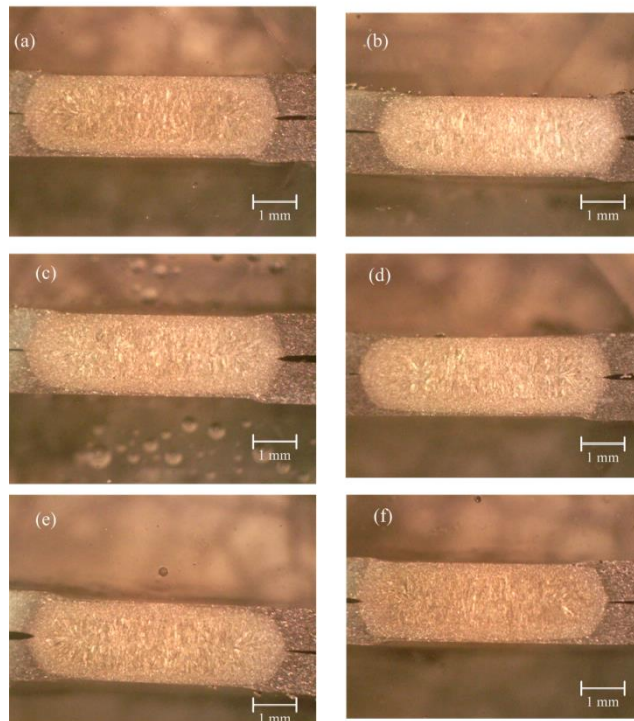
Figure 5.16 Cross-sectional views of poor fit-up welds. a) 2 mm double gap. b) 2 mm single gap. c) 1 mm double gap. d) 1 mm single gap. e) 0.5 mm double gap and f) 0.5 mm single gap.

The ED and DR were captured for the welds with the problems of poor fit-up. The ED curves under different gap intensities are summarized in Figure 5.15. Difference in fit-up intensity resulted in a discernible variance in the amplitude of the ED. As mentioned in the foregoing sections, the peak value and velocity of ED were strongly related to the thermal expansion of the sheets and size of the nugget. The ED amplitude was inversely

proportional to the fit-up distance H, and the air-gap generated due to a single existing shunt weld was found to have less influence on the ED than that attributed to two existing shunt welds.
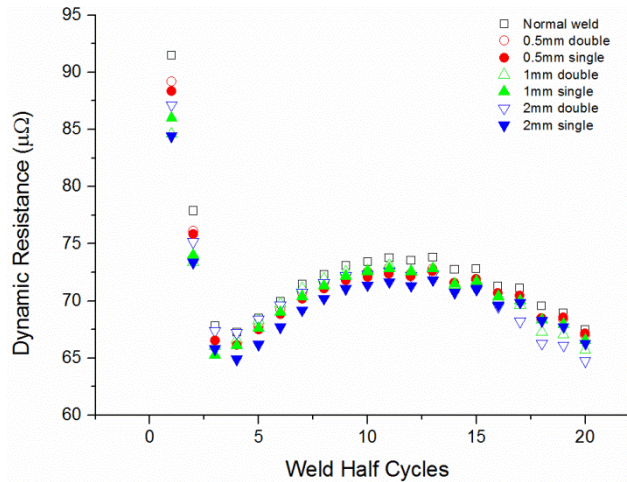
Figure 5.17 Dynamic resistance curves of different poor fit-up conditions

The DR curves with different fit-up intensity are presented in Figure 5.17. An outstanding difference among the DR curves is seen, where the gap intensities (H) varied. The greater the gap intensity, the greater the decline in DR values. Podrzaj compared the stress distribution at the sheet interface between non-deformed and deformed sheets [130]. The higher electrode was usually required for high gap intensities, and the stress distribution was then related to contact resistance. Then, the DR was proportional to the total heat generation in the base metals. That finding accounted for the potential decline in the ED curves and DR values.

5.4 Close-to edge welds

Welds close to an edge were produced on the mild steel sheets as in Figure 5.18. Three different distances from the edges were selected, 6 mm, 8 mm and 10 mm. Three welds

close to the edge were made on the same sheet for averaging, where the weld spacing was 30 mm. Sufficient weld spacing ensured that no substantial portion of the welding current was diverted.
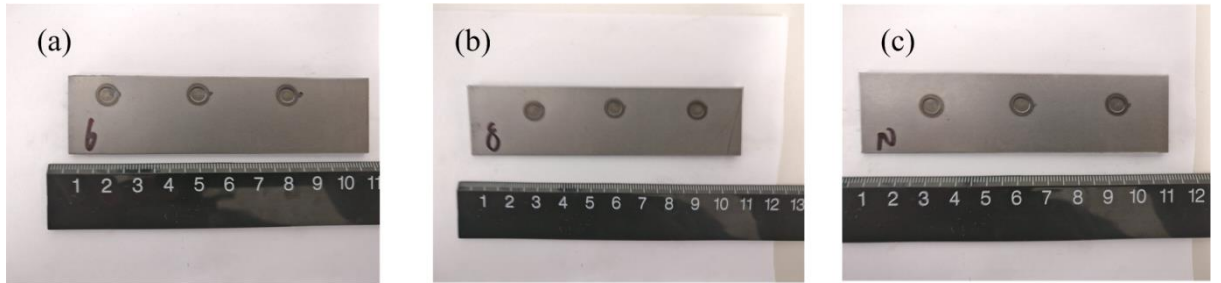
Figure 5.18 Close-to-edge welds at different distances. (a) 6 mm. (b) 8 mm and (c) 10 mm.
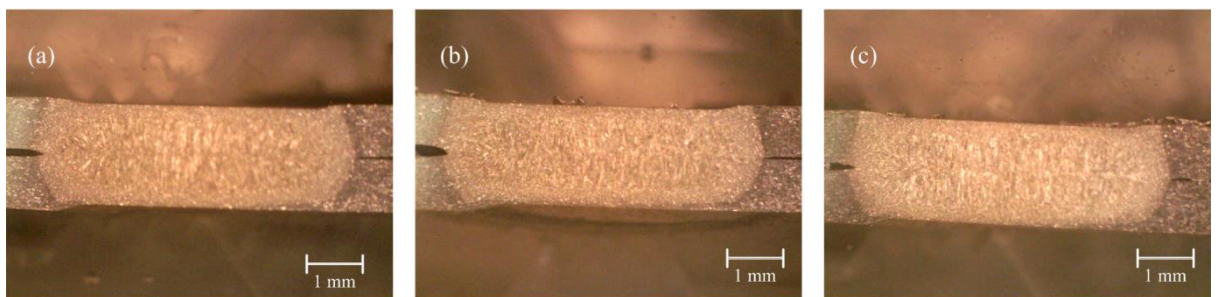
Figure 5.19 Cross-sectional views of close-to-edge welds. a) 6 mm. b) 8 mm. c) 10 mm.
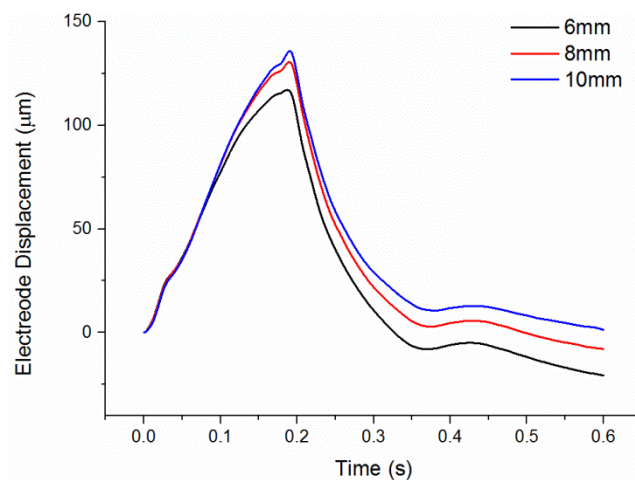
Figure 5.20 Electrode displacement curves of different distances from the edge
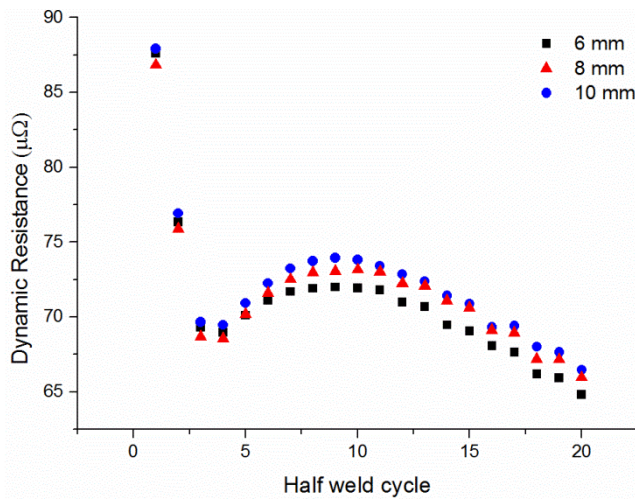
Figure 5.21 Dynamic resistance curves of different distances from the edge

The ED curves and DRcurves were captured at different values of *L*, as demonstrated in Figure 5.20 and Figure 5.21. It is evident that the amplitudes of ED curves dropped with the decrease in distance from the edge, where insufficient thermal expansion was produced from the surrounding cold metals. The ED velocity also decreased with the decrease in distance from the edge. The amplitudes of DR curves also showed proportional trends with the distance from the edge. The volume of surrounding sheet metal influenced the heating and cooling via conductive heat in the welding stage. When the distance from the edge was small, the cooling rate in the sheet metal was constrained, and the heating effect became dominant. Thus, the DR curve of *L* = 6 mm yielded a higher values than that of *L* = 10 mm. A similar finding in stainless steel was presented by Wen et.al [64]. They also suggested that further reduction caused expulsion at the faying surface, as insufficient EF was exerted to withstand the thermal expansion force from the molten zone.

112

5.6 Summary of the effects of abnormal process conditions on the dynamic signals

It was found that abnormal process conditions had a pronounced impact on the dynamic signals. Shunting effects, close-to-edge welds, and airgap conditions affected the DR and ED values. In this study, the effects of electrode misalignment were not considered for ED and DR curves, where the large amplitude of axial and angular misalignment could lead to severe expulsion in mild steel. Moreover, electrode misalignment could easily be identified via uneven indentation marks. The endpoint value and average value of DR curves usually declined under such abnormal process conditions, an effect that differed from the features in the cold welds. On the other hand, the peak value of ED was strongly related to total thermal expansion of the base metal, and thus a direct correlation between nugget diameter and ED values was derived. Figure 5.22 summarizes the peak values of ED curves under different types of abnormal process conditions. It is found that the shunting effect has the greatest influence on nugget size in mild steel, where a narrow weld spacing below 16 mm can result in an undersized nugget. In contrast, the weldability range of mild steel close to an edge and with an air gap is much wider. Thus, it is believed that ED curves are more suitable for detecting abnormal process conditions in the plant environment.
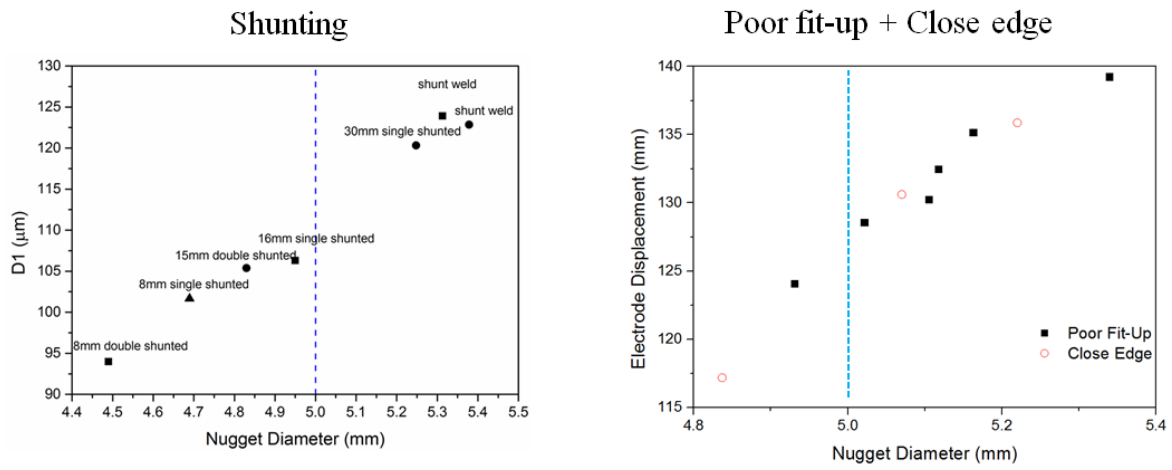
Figure 5.22 A summary of ED peak value under abnormal process conditions.

Chapter 6 Monitoring and characterization of electrode degradation in RSW under abnormal process conditions

Electrodes used in RSW gradually deteriorate under mechanical and chemical factors. Mushrooming occurs that to enlarges the contact radius, reducing the current intensity and heat generation. In addition, voids and inadequate melting can be found due to a cavity and pits on the electrode tip surface, from which the mechanical strength of the joint and electrode life can be dramatically affected. Abnormal process conditions such as shunting, poor fit-up, and electrode misalignment result from poor arrangement of the weld sequence and deformation of the sheet metals and welding arm of the machine. These factors can also have significant impacts on electrode degradation. In this section, the electrode degradation mechanisms of two zinc-coated steels with preset electrode misalignmenwere examined.

6.1 Electrode life with Zn-coated steels under electrode misalignment

6.1.1 Endurance test

The electrode life of misaligned electrodes was determined via carbon imprints of the electrodes and the tensile shear strength. Table 6.1 presents the carbon imprints of the upper electrode throughout the endurance test. At 0 welds, the misalignment was introduced at the beginning of the electrode life by adjusting the machine gun of the spot welder by 5°. The electrode welded with galvannealed steel (GA electrode) developed small voids at its center at weld number 50, which was faster than the cavity formation at 200 welds in previous study [148]. The small voids at the center enlarged further in axial directions during testing and the final diameter of the cavity was approximately 2.2 mm at 200 welds. In contrast, the electrode welded with galvanized

steel (GB electrode) gradually developed a small irregular contact area, with no obvious pitting or cavity found at 200 welds.

Table 6.1 Carbon imprints of upper electrode from 0 to 200 welds

Weld Number	GA	GB
0		
50		
100		
150		
200		

It wais noted that both electrode tip area decreased with an increase in the number of welds, but with different mechanisms. The changes in electrode tip morphology are shown in Figure 6.1 and 6.2. The area of the GA electrode decreased with an increase in the number of welds, and the tip diameter remained steady. Considerable pitting was observed at the center of the tip, due to picking up of the brittle IMCs by the electrodes. Limited mushrooming was found in the carbon imprints due to the reduced electrode life. In constrast, the contact region of the electrode welded with galvanized steel (GB electrode) decreased sharply after the first 50 welds, although the expanded contact area owing to the electrode mushrooming was expected. The changes in tip diameter and tip area for the GB electrode were steady. Sticking of the electrode occurred occasionally after 100 welds, possibly as a result of the reduced contact in the GB electrodes. The

current intensity was inversely proportional to the contact area, and the value should climb dramatically due to shrinking of the contact region. More heat was generated from the base metal and a large amount of alloy products was produced between the base metal and the electrodes.
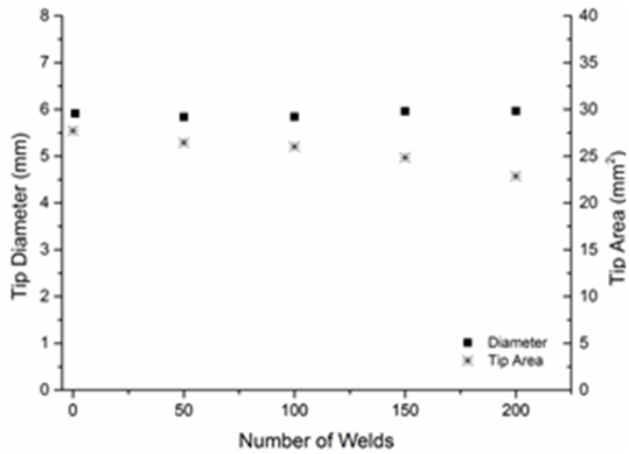
Figure 6.1 Summary of tip diameters and areas from carbon imprints of GA electrode
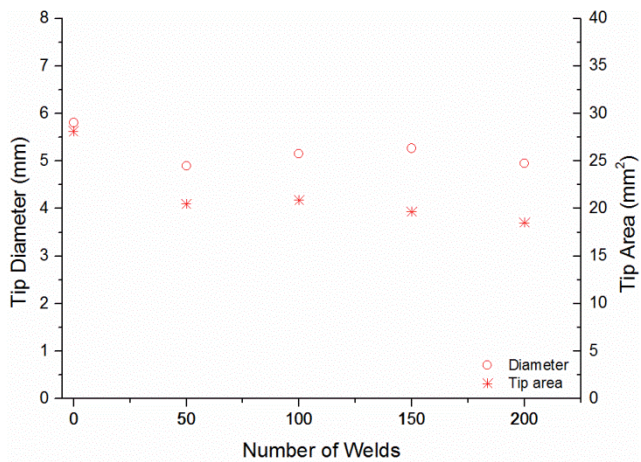
Figure 6.2 Summary of tip diameters and areas from carbon imprints of GB electrode

Side views of the GA and GB electrodes are presented in Figure 6.3, where annulus electrode topology is not discernible from the side view. A slight increment in the axial direction in the GA electrode is seen in Figure 6.3 (c). On the other hand, a much severer mushrooming is seen on the GB electrode, that was not obvious on the carbon imprints. The GB electrode with increased diameter outperformed the GA electrode.

117

Moreover, the curved tip morphology was revealed from the side view by the CCD camera.

Figure 6.3 a) Side view of GA electrode from CCD camera at 200 welds. b) Side view of GB electrode from CCD camera at 200 welds. c) electrode outlines of 0 welds and 200 welds.
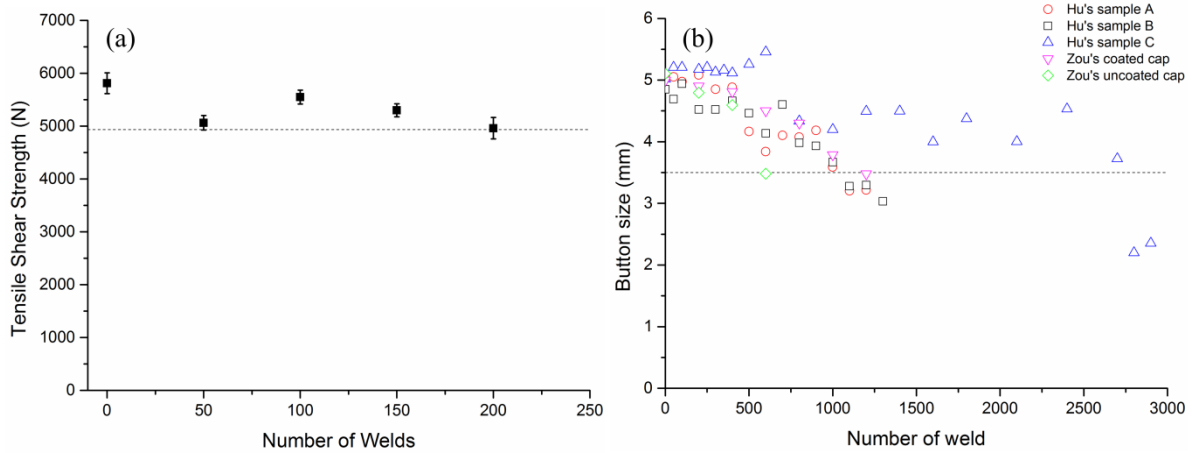
Figure 6.4 Electrode life during welding with GA steel. (a) current study. (b) previous works [10, 95]
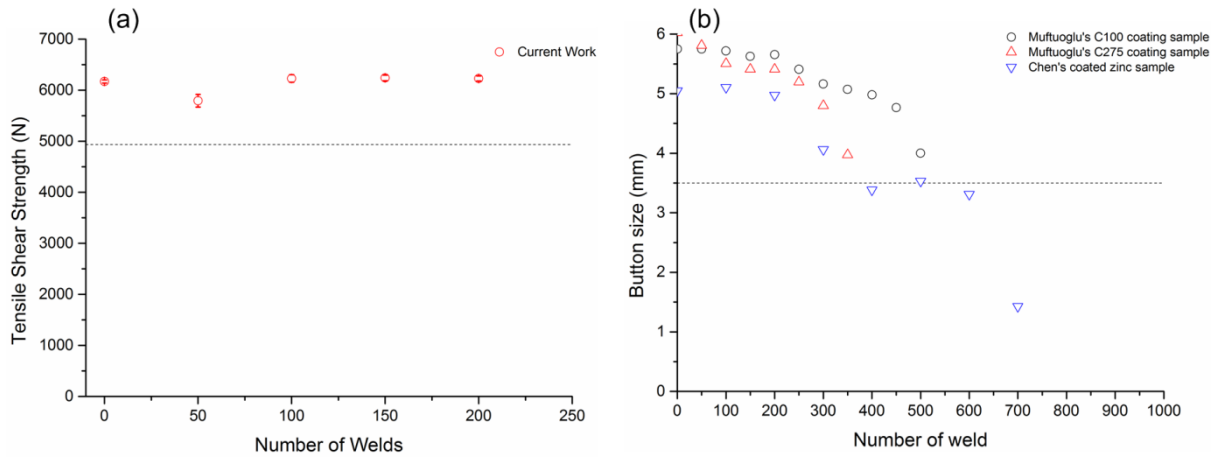
Figure 6.5 Electrode life during welding with GB steel. (a) Current study. (b) previous works [92, 149]

The electrode life found in this study and previous work is summarised in Figure 6.4 and 6.5. In the current study, the tensile shear strength of GA joints fluctuated during the first 100 welds and a clear decline in strength was found from 100 to 200 welds. In contrast, the strength of the GB joints remained steady from 0 to 200 welds. In previous studies of Hu and Zou, the fluctuations in button size were seen and much longer electrode lives were reported [10, 95]. The shortest electrode life during welding GA steel reached nearly 600 welds, three times of that in the current study. In addition, the electrode life in Muftuoglu's study varied with the thickness of the hot-dip galvanized coating, where a thicker Zn coating had a short electrode life [149]. The shortest electrode life during welding GB steel was about 400 welds. However, no electrode sticking was reported in previous study of electrode life. Different criteria were used for the current work and previous work, where 80% of the original TSS and 3.5-mm button size were considered, respectively. This difference in electrode life criteria might also account for the substantial differnce in electrode life between this work and previous studies.
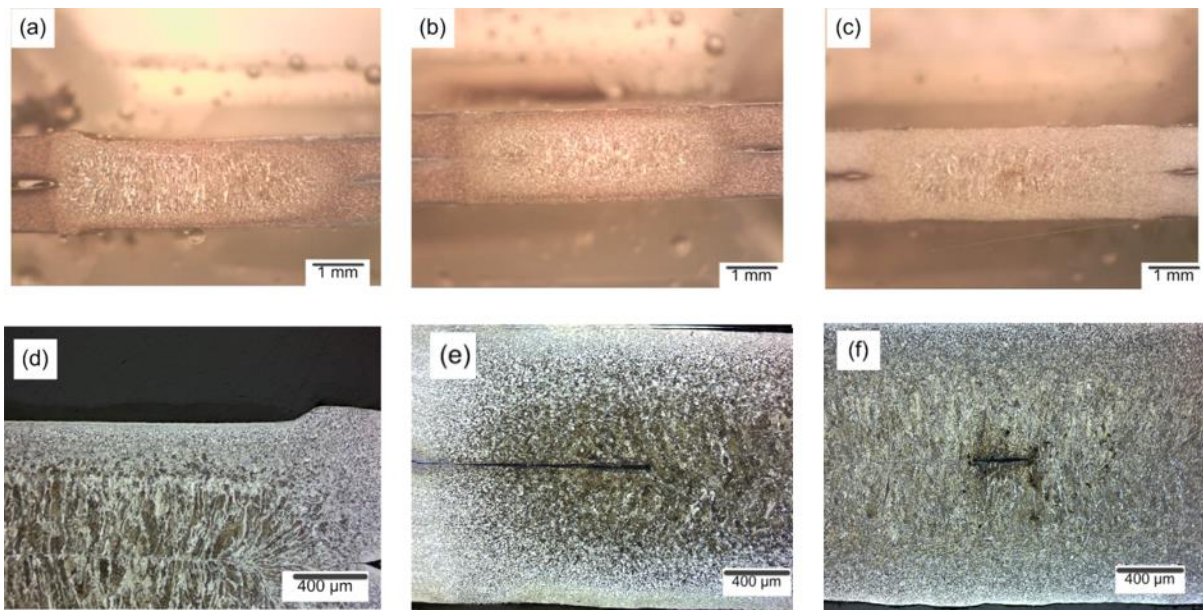
Figure 6.6 Cross-sectional views of nuggets under stereomicroscope and optical microscope at (a,d) 0 welds. (b,e) 50 welds and (c,f) 150 welds

Angular misalignment led to a short electrode life when welding GA steel. To investigate the decline in the TSS of GA joints, cross-sectional views of the nuggets at a different number of welds are presented in Figure 6.6. At the beginning of the test, an uneven indentation mark is observed due to the electrode misalignment, as manifested in Figure 6.6 (a). The nugget is found to be larger on the left side of the cross-section due to the shorter electrical current path [150]. Furthermore, cracks in Figure 6.6 (b, e) are found on the edge of the nugget as a consequence of electrode misalignment. In the tensile shear mode, the nugget size determines the predominant failure mode of the joint [17]. The void at the nugget edge considerably reduces the effective diameter of the fusion zone, in turn undermining the load-bearing capacity in pull-out mode. The tensile strength is found to drop again at 150 welds, where un-melted regions are found at the edge and center of the nugget in Figure 6.6 (c, f). Electrode wear was found to contribute to solidification voids at the center of the faying surface. The cavity in the electrode tip caused a wider spread of the current, resulting in low current density and less heat generated [98]. Wang identified the critical pitting diameter in electrode wear

of steel welding [79]. When the void grows beyond 3 mm, the center of the faying cannot be melted with incomplete fusion, as little current goes through the center of the faying surface. In this study, the final cavity diameter at 200 welds was 2.2 mm, indicating that electrode wear had a minor influence on nugget strength.

6.1.2 Electrode displacement curves of worn electrodes

Electrode displacement was directly recorded and processed from the laser triangulation sensor mounted on the AC pedestal welder. Figure 6.7 depicts the ED signals of GA steel, from which distinct curves due to electrode wear can be observed. The thermal expansion of the sheets contributed directly to the ED, which can be considered one of the criteria of spot weld quality [56]. It is noted that the peak values of the displacement gradually declined with increasing number of welds, as shown in Figure 6.7 (a). The decline can then be attributed to decreased tip area due to the pitting and be associated with reduced heat input. Moreover, the decline in strength at 50 welds due to the void in the nugget is reflected by the decreases in the peak value. In addition, the heat generated per unit time was found to be proportional to the ED velocity in Figure 6.7 (b). The carbon imprints indicated that the tip area decreased due to the cavity, and the current intensity increased correspondingly. Nevertheless, the ED curve, a measure of thermal expansion of the sheets, showed no increase in the peak value. The center region with severe pitting had no contact with the workpiece and no current flow through the region. This region was melted by the heat conduction from the surrounding contact regions. Based on Wang's numerical simulation, the volume of fusion zone was inversely proportional to the cavity size [79]. Thus, thermal expansion of the base metals is expected to decrease in the worn electrodes, an conclusion that matches the observed ED curves.
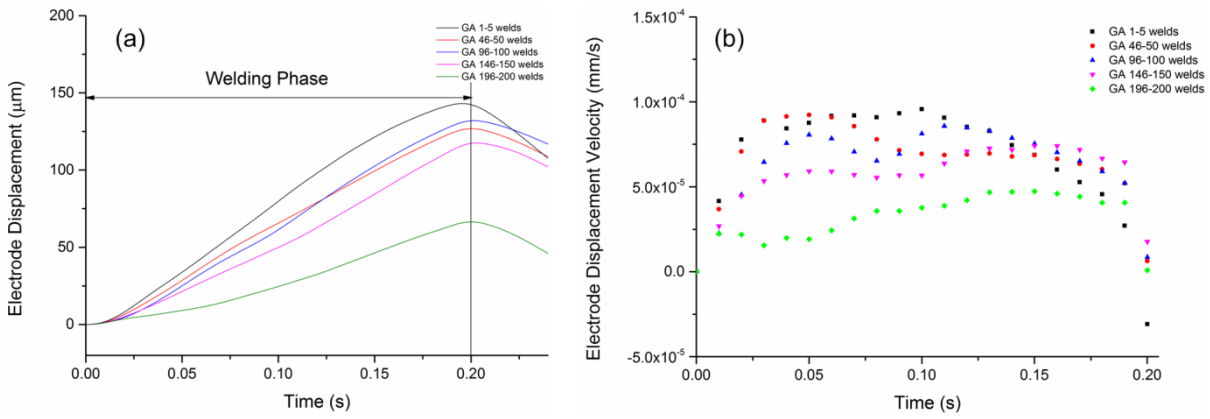
Figure 6.7 (a) Electrode displacement signals of GA steel from 0 to 200 welds. (b) electrode displacement velocity from 0 to 200 welds.
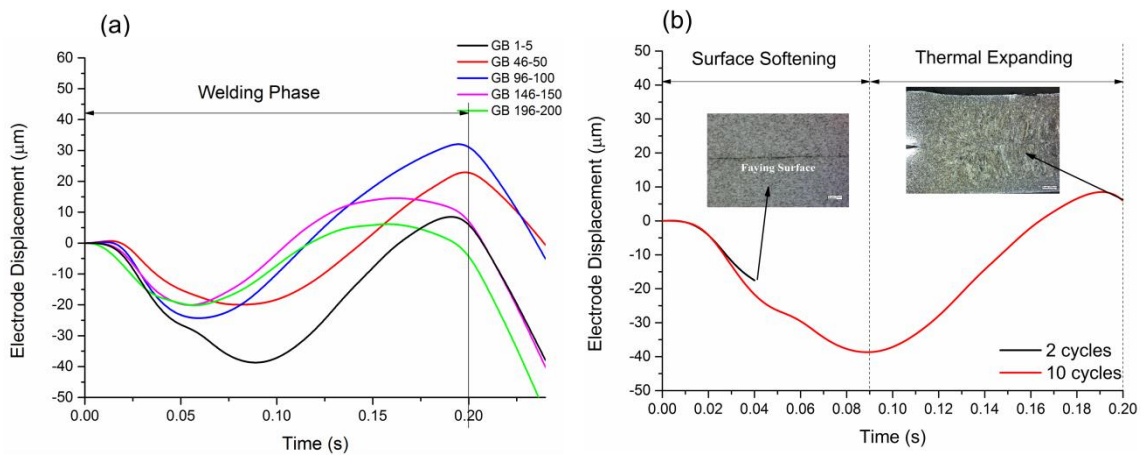
Figure 6.8 (a) Electrode displacement curves of GB steel from 0 to 200 welds. (b) microstructure of GB nugget at different welding times

Distinct ED curves are seen for welding with GB steel in Figure 6.8. A noticeable decline occurs in the first few cycles in the welding stage. It was determined that the declines in ED curves resulted from the melting and squeeze-out of the zinc coating. The η-Zn phase had a low melting point (~ 420 °C), when the initial heat generated melted the zinc layer on the sheet metal. Figure 6.8 (b) clearly shows the microstructure of the faying surface after two and ten cycles. No zinc layer was found at the faying surface and electrode-workpiece surface after two cycles. Then a proper nugget was formed at ten cycles, along with a gradual increase in ED values. Thus, the ED curves of GB steel could be divided into two phases, a surface softening stage and a thermal expanding stage. Therefore, the ED curves at different weld numbers presented different

122

patterns. It was noted that a decline in contact area was disclosed in the carbon imprints of GB electrodes, indicating that the degree of surface softening would be lessened with the worn electrode. A reduced decline in the softening stage was seen. Moreover, the decline in tip diameter constrained the peak value of ED curves. Thus, a decline in ED peak value was reported when substantial electrode degradation had occurred at 200 welds.

6.2 Electrode degradation mechanism of different zinc coated steels under angular misalignment

Electrode misalignment led to much shorter electrode lives in both GA and GB electrodes. Alloy formation and mechanical deformation are the two major factors in shortening electrode life when welding zinc-coated steel [86]. Electrodes gradually mushroomed as a consequence of the softening effect. Further, copper can be picked up via fracture of the brittle intermetallic compounds. The electrode life with misaligned electrodes was drastically reduced, compared to those previous reported studies in welding galvannealed steel [16, 87, 151]. Thus, alloying distribution and recrystallization were expected to be influenced under electrode misalignment, leading to the rapid degradation in the Section (6.1.1).

6.2.1 Alloying reaction
To predict the potential IMC formation, the coating layer of the base metal was examined via SEM and EDS. The thickness of the zinc coating of GA and GB was around 13 μm and 17 μm, respectively, averaged from ten measurements in Figure 6.9. The EDS results are summarized in Table 6.2. Due to annealing of the zinc layer at 500°C, the GA coating consisted of δ, $\delta + \Gamma_1$ and Γ_1, where the Fe content increased graduall. Γ_1 was considered an effective Fe-rich barrier to prolong the electrode life during the welding of galvannealed steel [16]. On the other hand, η-Zn was found in the

GB coating. The transition layer between pure zinc layer and Fe matrix was so narrow that it was beyond the EDS resolution.
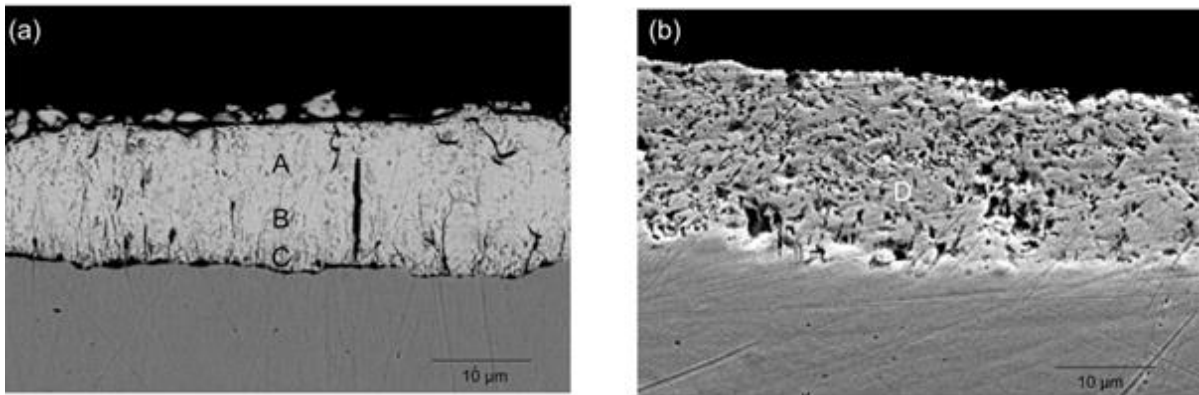
Figure 6.9 SEM images of GA and GB coatings

Table 6.2 Chemical compositions in GA and GB coatings

Material	Site of point	Fe (wt%)	Zn (wt%)	Possible Phase
GA	A	10.6	89.4	δ
	B	13.6	86.4	$\delta + \Gamma_1$
	C	23.5	76.5	Γ_1
GB	D	0.8	99.2	η
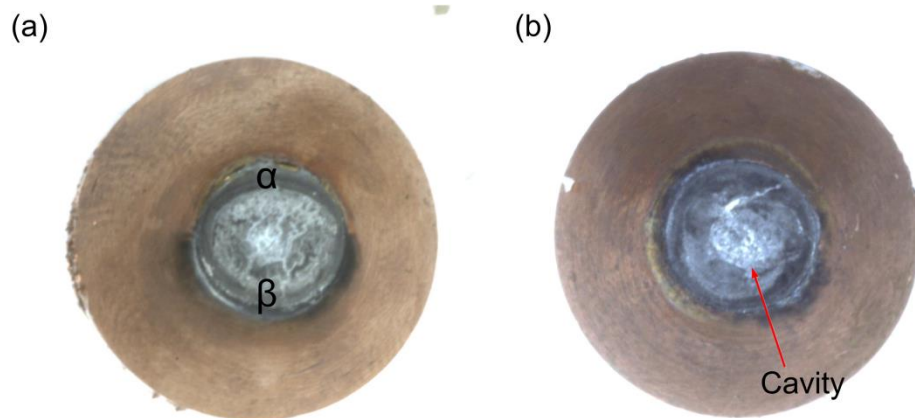
Figure 6.10 Top views of worn GA electrodes. (a) 10 welds. (b) 200 welds
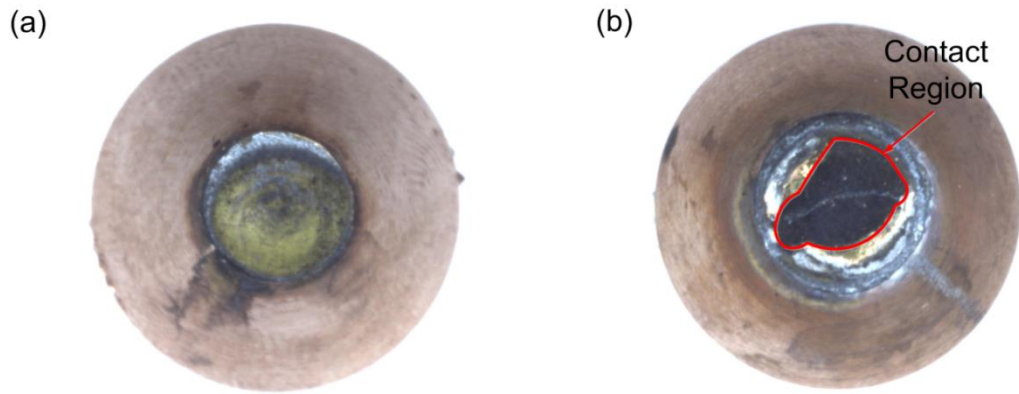
Figure 6.11 Top views of worn GB electrodes. (a) 10 welds. (b) 200 welds

The affected electrode tip surfaces were observed via CCD camera. The top views of the GA electrodes and the GB electrodes at 10 and 200 welds are presented in Figure 6.10 and Figure 6.11. The appearance of the worn GA electrodes is moderately changed from that of the brand-new electrode. Compared to the GA electrode at 200 welds, no visible mushrooming or pitting could be found on the electrode tip at 10 welds. Grey layers were observed on the electrode surface, suggesting potential alloying of base metal and electrode. On the GB electrodes, most of the tip surface was covered by a yellow alloy product at 10 welds, while the silver edge clearly indicated limited alloying between Cu and Zn. The uneven temperature profile on the electrode tip did not cause abundant alloy formation. At 200 welds, a dark contact region identical to the shape of the carbon imprint was evident. The rest of the tip areas did not contact properly with the sheet metal at 200 welds. Even though the GB electrode mushroomed, the effective tip area did not increase.
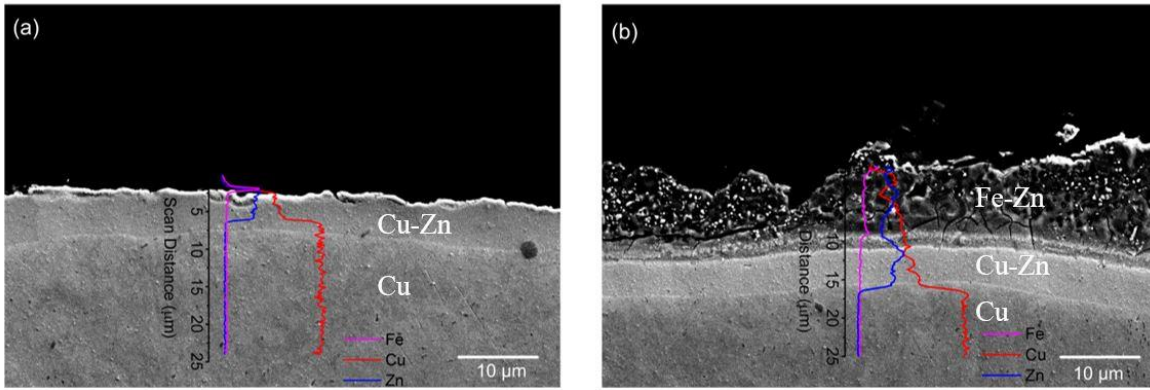
Figure 6.12 a) SEM image of region α of a worn electrode at 10 welds. b) SEM image of region β of a worn electrode at 10 welds.

To reveal the composition of IMC products at different regions of a worn electrode, an EDS study of selected regions of the GA electrode at 10 welds was presented in Figure 6.12. Different alloying products were found at two edges of the electrode due to an uneven temperature profile. In Figure 6.12 (b), Fe-Zn phase Is found on the outermost layer of the GA electrode, coming from the zinc coating of the base metals as reported in Hu's study [16]. However, the δ Fe-Zn phase is limited to the very thin outermost layer in Figure 6.12 (a), where inefficient localized heat could not reach the melting point of the Fe-Zn phase. In conventional steel spot welding, the temperature at the tip surface can reach 600 °C - 700 °C, and the melting temperature of δ Fe-Zn is around 660 °C [16]. Misalignment in electrodes caused the δ phase to melt partially and accumulate on the electrodes. Minimal Fe content could be found in the middle and innermost layers of the electrode. The thicknesses of alloy products in Figure 6.12 (a) and (b) were measured to be ~ 5 μm and ~ 15 μm, respectively.
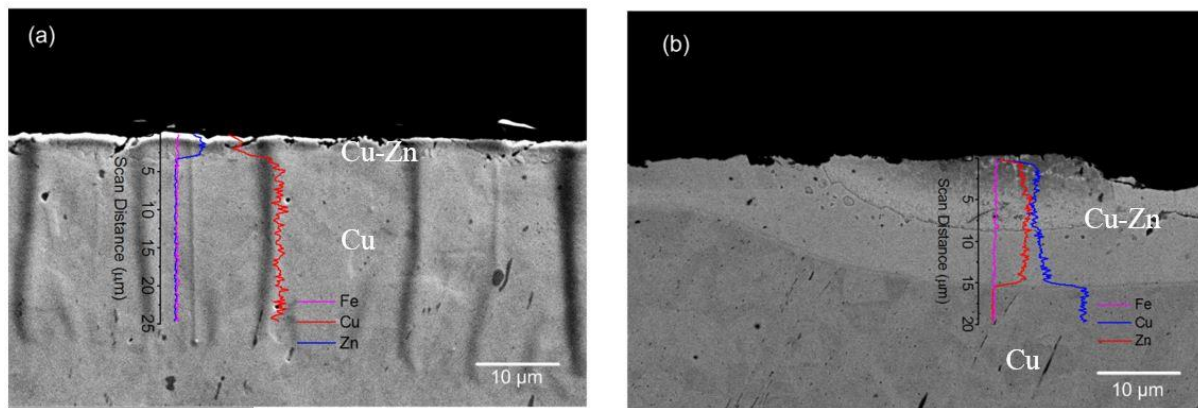
Figure 6.13 (a) SEM image of the silver edge of GB electrode at 10 welds. (b) SEM image of the yellow area of GB electrode at 10 welds.

Distinct alloy products were found at the GB electrode at 10 welds, as shown in Figure 6.13. The amount of Fe was scarce throughout the GB electrode because the GB coating had restricted amount of Fe. The melting point of η Zn is lower than that of δ Fe-Zn, causing the readily fomration of a Zn-Cu layer readily form at both edges of the electrodes. However, the penetration depths of the zinc element were varied depending on the local thermal field during production of the spot weld. The Cu-Zn alloy thicknesses was found to be ~ 4 μm and ~ 15 μm in Figure 6.13 (a) and (b), respectively.
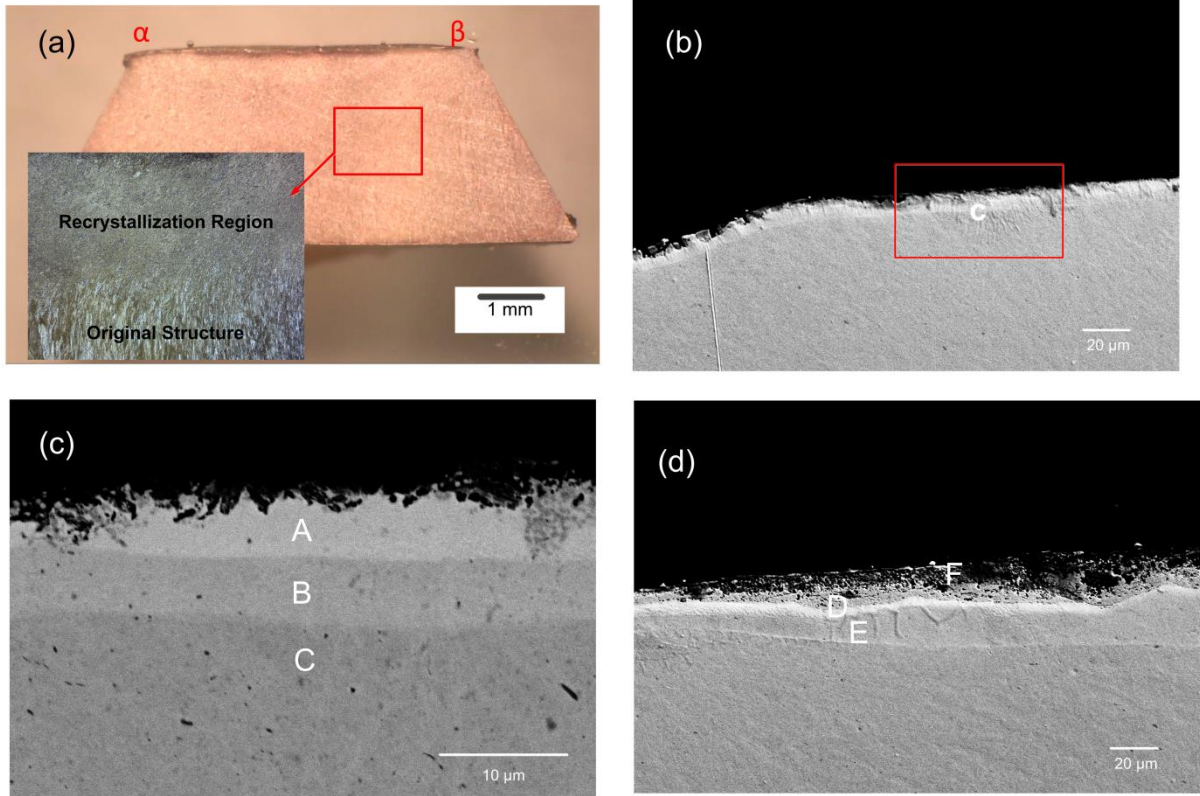
Figure 6.14 Metallographic examination of the worn electrode at 200 welds. (a) Stereo microscope examination at 15x magnification. b) SE image of region α of the worn electrode at 200 welds. c) BSE image of highlighted area. d) SE image of region β of the worn electrode at 200 welds.

Severe electrode pitting occurred by 200 welds with GA steel. The cross-section of the electrode and the SEM results of edges of the electrode tip at 200 welds are shown in Figure 6.14. It was found that recrystallization occurred and distinct grain structures could be observed. Due to the electrode misalignment in the study, the grains were re-orientated towards the edge of the electrode tip because of the thermal gradient. Two regions (marked α and β in Figure 6.14 (a)) located at the edge of the electrode tip were further investigated with SEM and EDS analysis. It should be noted that different alloy compositions were explored in two regions depending on the local temperature field and contact condition. The averaged thickness of the alloy layers at α and β increased to 10.5 μm and 29.5 μm, respectively, onsiderably wider than the thickness at 10 welds.

Multiple layers were identified in each region via EDS analysis. Table 6 analyzes each layer based on the BSE images of the specimens. Region β was found to display Cu-Zn alloys and Fe-Zn phase was also picked up from the base metals, whereas region α comprised only $\beta + \gamma$ Cu-Zn at point A and $\alpha + \beta$ Cu-Zn at point B. Though the δ Fe-Zn phase was identified from the GA coating, the region α showed restricted distribution of Fe, indicating that a barrier with low Fe could not effectively protect Cu from picking up the base metal. Like to sample #2 in the study of Hu et.al [16], much faster wearing-out was expected to initiate in those Fe-free regions.

Table 6.3 Element composition at alloying regions on electrodes at 200 welds

Material	Site of point	Fe (wt%)	Cu (wt%)	Zn (wt%)
GA	A	10.9	32.5	56.4
	B	0.8	52.7	46.3
	C	0.4	97.9	1.1
	D	2.5	37.8	59.7
	E	1.1	54.4	44.2
	F	51.4	16.8	31.4
GB	A	68.3	22.1	9.7
	B	5.5	72.4	22.1
	C	0	100.0	0
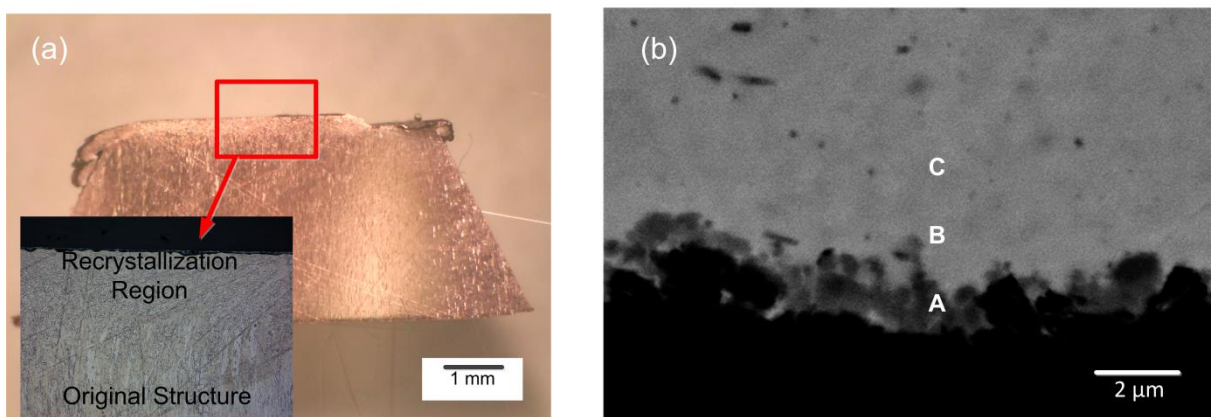
Figure 6.15 Metallographic examination of GB electrode after 200 welds. (a) stereo microscope examination at 15x magnification. (b) BSE image of alloy region on electrode.

Figure 6.15 shows a different electrode wear mechanism when welding with GB steels. The electrode tip experienced pitting on its right side, which was not clear from the CCD images and the carbon imprints. The formed intermetallic compound was brittle and readily fractured under mechanical force. It is also worth mentioning that a much thinner recrystallization region was formed than in GA steel welding. The element compositions of alloys distributed on the electrode remained nearly the same across the electrode tip. According to Table 6.3, A 68.3Fe-22.1Cu-9.7Zn alloy was found at the outermost area of the tip surface, the Fe content y reduced dramatically to 5.5 wt% at point B and the Zn content climbed substantially to 22.1%. Then, region C was identified as the copper matrix. A much higher Fe content was formed at the outermost layer of the electrode tip, whereas the very low Fe content was discovered after 10 welds with galvanized steel. The element composition identified from the EDS also showed a different Fe-Cu-Zn layer from that reported in previous work, from which the alloy layers were much thicker ($\sim$ 10 μm) and the β or $\beta+\gamma$ phase was expected. The gap was believed to be caused by the electrode sticking during the experiment. Electrode sticking usually resulted from local metallurgical bonding between the electrode and the base metal [152]. Because Cu-Zn brass formed readily during the spot welding, the brass alloy that covered the electrode was discernible. Electrode sticking is likely to occur and collapse of the alloy layer present initiates when the base metals and the electrodes separate. It is then difficult to observe a complete brass layer similar to those previous reported. To minimize electrode sticking, small welding current, short welding time, or a high EF should be implemented.

6.2.2 Electrode softening effect

Vickers microhardness of worn electrode

Different levels of mushrooming were found in the two sides of the worn electrodes at 200 welds in Figure 6.3 (a), indicating that the electrode tip softened differently under electrode misalignment, possibly due to different physical properties of the zinc coating.
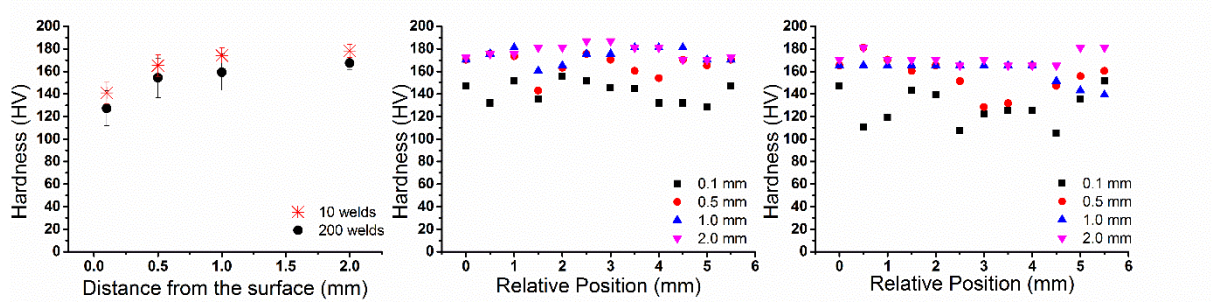
Figure 6.16 (a).Averaged electrode Vickers microhardness after different numbers of welds with GA steel. The influence of electrode misalignment on Vickers microhardness. (b). 10 welds. (c) 200 welds.

The temperature field in the regions of the electrode tip under electrode misalignment was nonuniform. To investigate the inhomogeneous softening, Vickers microhardness tests were performed on the etched cross-sections of the electrodes. Figure 6.16 (a) compares the Vickers microhardness of the GA electrode at 10 and 200 welds. It is noted that softening in the worn electrode is proportional to the number of welds, illustrating the reduction of Vickers microhardness and the softening area affected. At 10 welds, a substantial reduction in Vickers microhardness was observed at the measurement line 0.1 mm away from the electrode tip, and the softening region gradually enlarged with the number of welds. When 200 welds had been made, the softening zone reached ~ 1 mm. The influence of misalignment on softening was also examined by Vickers microhardness test as shown in Figure 6.16 (b) and (c). The electrode misalignment substantially influenced the distribution of Vickers microhardness. A moderate reduction in the electrode Vickers microhardness was found

at the right side of the electrode when 10 samples had been welded, because more heat was generated due to the misalignment. A strong oscillation in the Vickers microhardness profile was noticed along the electrode tip at 200 welds. The electrode experienced severe copper pickup at the center of the tip, and the electrode surface gradually developed more asperities. Thus, the peak temperature of the electrode increased significantly at the localized asperities and thereby aggregated softening effect at these sites.
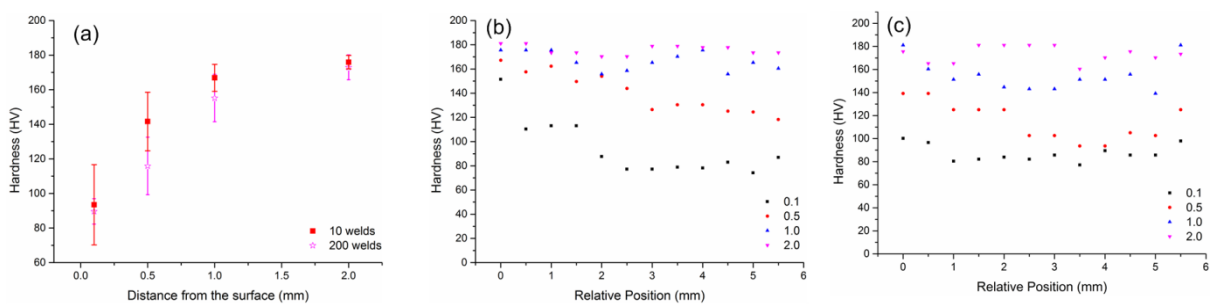
Figure 6.17 (a).Averaged electrode Vickers microhardness after different numbers of welds with GB steel. The influence of electrode misalignment on Vickers microhardness. b). 10 welds. c) 200 welds.
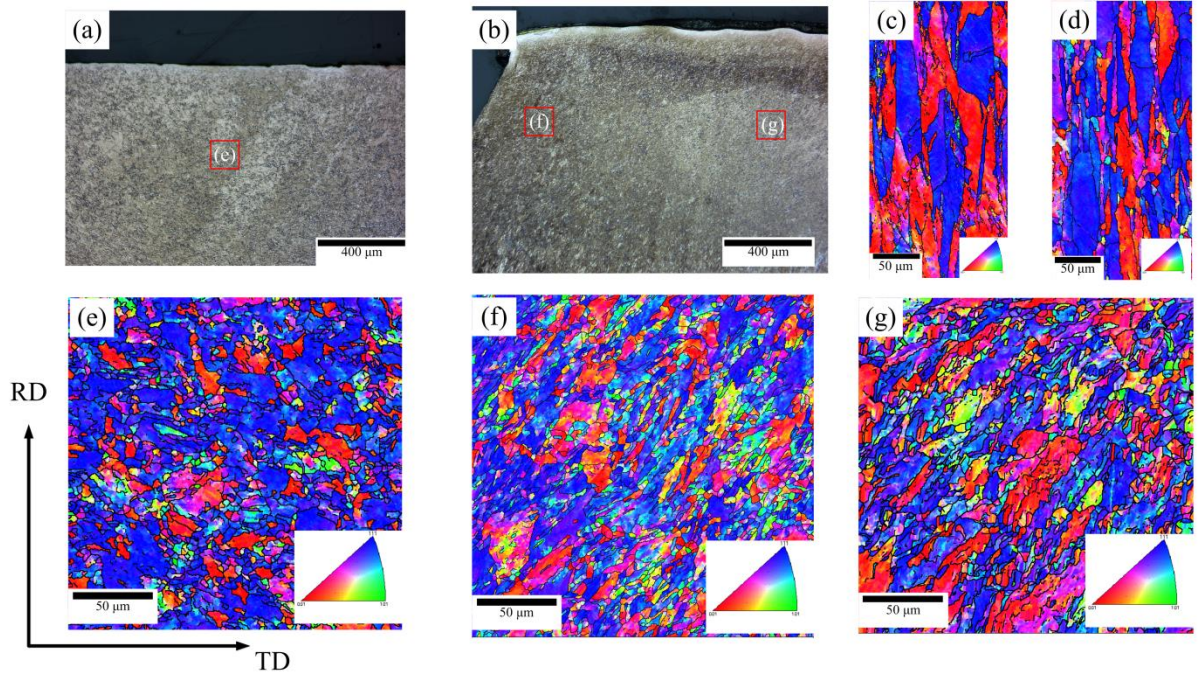
Figure 6.18 Etched cross-sections of worn electrodes of GA. (a) 10 welds. (b) 200 welds. EBSD mapping of the base metal region. (c) 10 welds. (d) 200 welds. EBSD mapping of the highlighted areas of the recrystallization regions at (e) 10 welds and (f-g) 200 welds.

In Figure 6.14(a), a clear boundary between the base metal and recrystallization region was seen. Recrystallization processes accounted for the softening of the worn electrode. The uneven temperature field introduced by electrode misalignment also affected the grain morphology in the recrystallization region. Previous studies only qualitatively examined recrystallized regionsng using OM images. To quantitatively understand the microstructure evolution under electrode misalignment, EBSD mapping was implemented on the cross-sections of the worn electrodes after 10 and 200 welds with GA steel, as demonstrated in Figure 6.18. Several recrystallization regions of interest are marked in the OM images in Figure 6.18 (a) and (b). Region (e) was the center of the worn electrode after 10 welds with GA steel. Regions (f-g) were taken at the same distance from the electrode surface, whereas region (f) was closer to the electrode

contact region, where a high temperature was attained at the contact region of the misaligned electrodes.

Table 6.4 Average grain diameters at the mapped regions in Figure 6.18

Mapped regions	(c)	(d)	(e)	(f)	(g)
d in RD direction (µm)	13.98	12.99	2.89	2.57	2.87
d in TD direction (µm)	6.06	4.94	3.62	2.58	2.55

EBSD mapping revealed the recrystallization and grain rotation due to the electrode misalignment. Because the electrode was manufactured from cold extruded copper rod and no annealing was performed before the welding, the base metal presented a very strong fiber texture in the <100> and <111> directions, as shown in Figure 6.18 (c). A strong fiber texture <111> existed at the recrystallization region at 10 welds in Figure 13 (e). Then, the fiber texture <111> continued to weaken at 200 welds because more grains with different orientations could be found in the recrystallization regions shown in Figure 13 (f-g). The averaged grain diameters in the rolling direction (RD) and transverse direction (TD) of the mapped regions in Figure 6.18 are summarized in Table 6.4. Compared to base metals, the grain diameter declined dramatically in the RD direction from ~ 13 μm to 2.5 μm, and smaller grains could be observed in the recrystallization regions, even after only 10 welds. More importantly, a rotation in the grain orientation was readily seen in Figure 6.18 (e-f) over the asymmetric pressure under the misaligned contact. 2D finite element simulation of angularly misaligned electrodes showed that higher pressure was attained in proximity to the shortest electrical current path and an asymmetric pressure distribution was seen [102]. The grains were re-oriented in the direction normal to the inclined pressure.
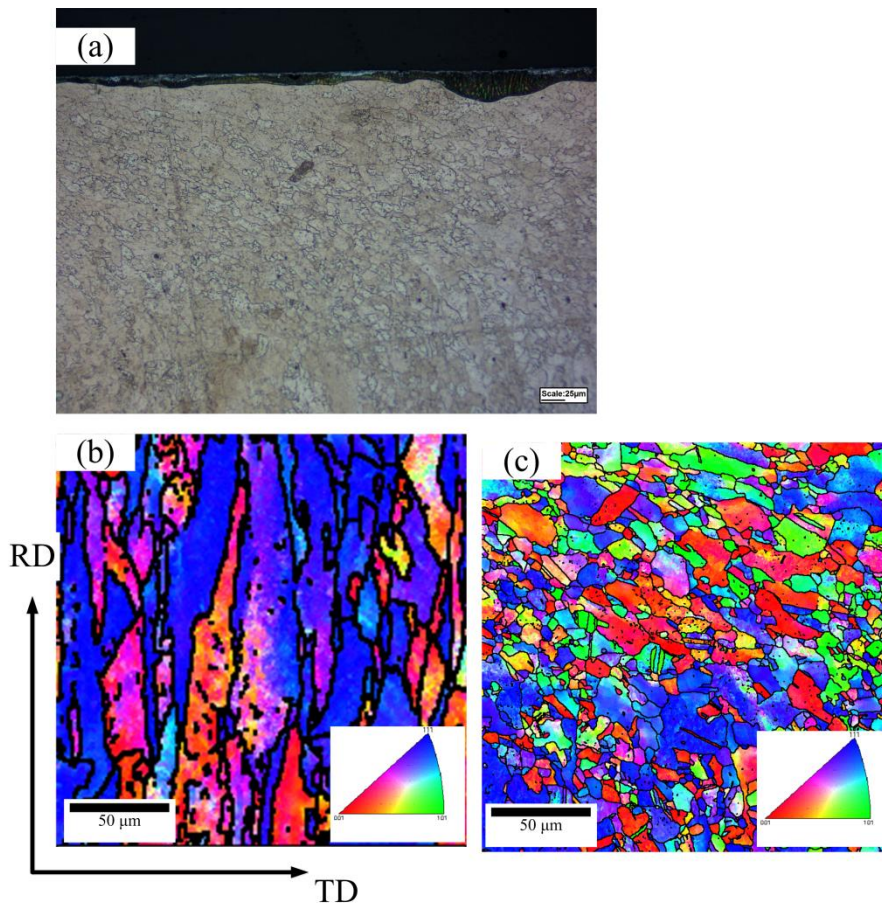
Figure 6.19 (a) Etched cross-section of worn electrode of GB. EBSD mapping of the (b) BM region. (c) Recrystallized region

EBSD mapping was also carried out on the worn electrode welded with GB steel. The cross-section of a worn electrode shows that a much narrower recrystallized region formed on the worn electrode compared to the counterpart in Figure 6.18. The EBSD mapping was taken at the base metal and the recrystalized regions. The same fiber texture via the cold extrusion process is found at the base metal region in Figure 6.19 (b), whereas the rotation of the recrystallized grains was completely different. Due to the severe softening effect in the worn electrode with GB steel, a much severely mushroomed electrode tip was seen. The grain in the recrystallized region was found to expand and rotate axially, as shown in Figure 6.19 (c). The influence of uneven pressure distribution from angular misalignment was very limited on the GB electrode. The average grain diameters of the mapped region in Figure 6.19 are summarized in Table

136

6.5. It is clearly seen that the average grain diameter in the recrystallized regions of the GB worn electrode was much greater than those in GA worn electrode. In other words, a finer microstructure was formed when welding with GA steel than with GB steel, that was strongly dependent on the welding current used. Higher welding current was required to melt the galvanized coating, increasing the peak temperature in the electrode.

Table 6.5 Average grain diameters at the mapped regions in Figure 6.19

Mapped regions	(b)	(c)
d in RD direction (μm)	14.8	4.4
d in TD direction (μm)	6.3	4.6

Taylor factor analysis
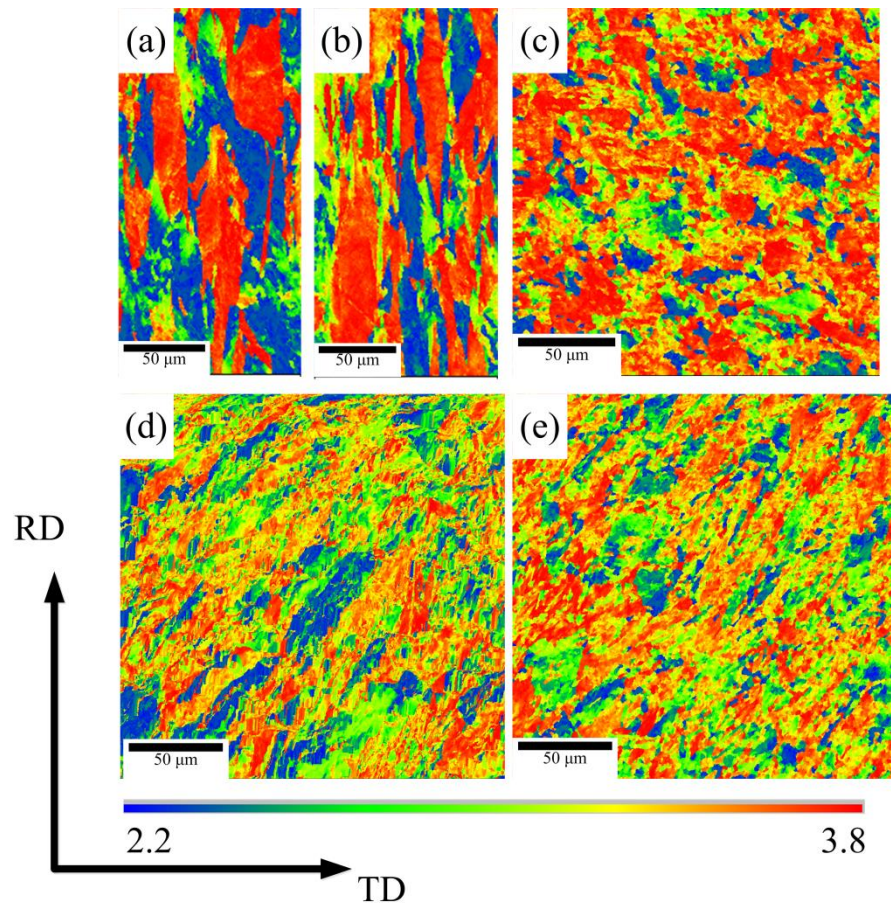
Figure 6.20 Taylor factor contours in mapped regions (c-g) from GA EBSD mapping.
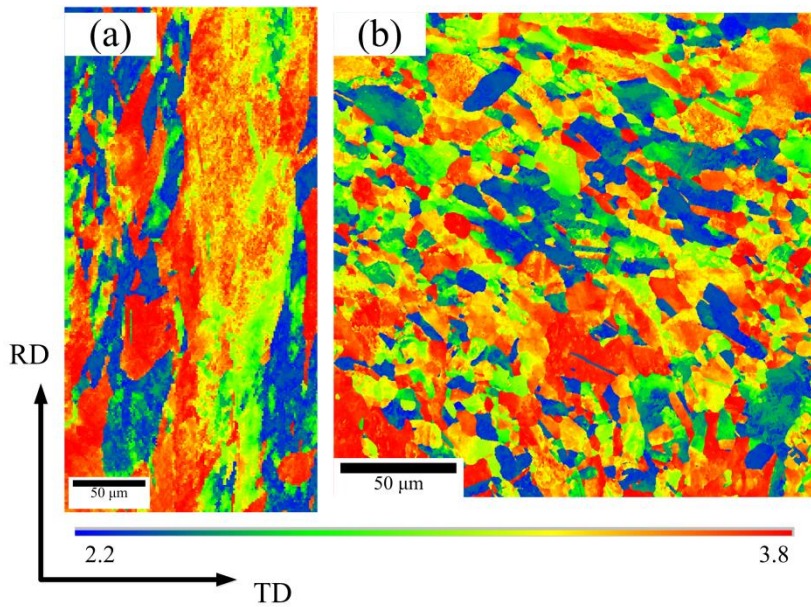
Figure 6.21 Taylor factor contours in mapped regions (b-c) from GB EBSD mapping

The weakened texture in the recrystallized region required less deformation energy against the EF. To reveal the influence of recrystallization on electrode deformation, the Taylor factors along the EF direction of the mapped regions are summarized in Figure 6.20 and 6.21).
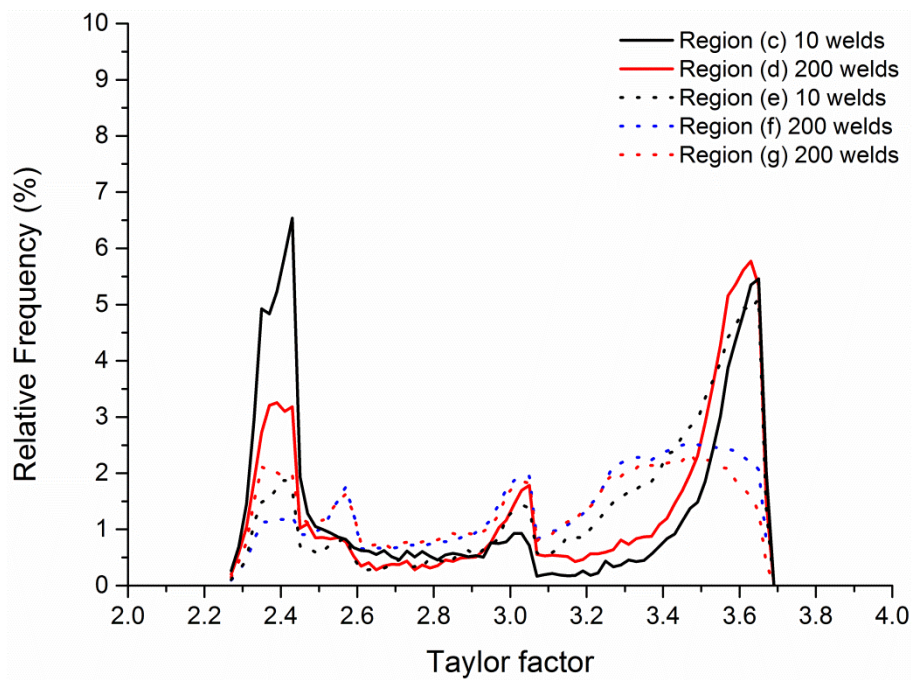
Figure 6.22 Evolution of the Taylor factors of mapped regions in Figure 6.20.
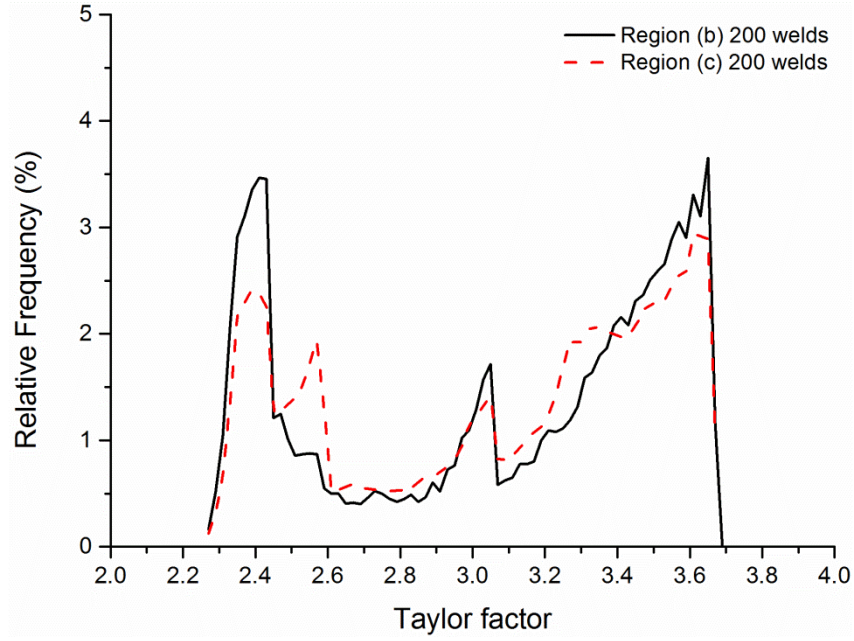
Figure 6.23 Evolution of the Taylor factors of mapped regions in Figure 6.21.

Distinct distributions of the Taylor factors are observed in Figures (6.22 and 6.23), providing insight into how the recrystallization tuned the mechanical properties of the electrode tips. The Taylor model assumes that slip of polycrystal relies on five independent slip planes. Among all combinations of the five slip systems, the active combination has the minimum value of accumulated slip. Taylor also assumed that slip systems are hardened at the same rate[153]. If a randomly oriented polycrystal is subjected to uniaxial tension along the x-direction, deformation occurs by the axially symmetric flow. Thus, the following equations are yielded:

$$d\varepsilon_y = d\varepsilon_z = -\frac{1}{2} d\varepsilon_x$$

(6.1)

$$d\gamma_{yz} = d\gamma_{zx} = d\gamma_{xy} = 0$$

(6.2)

And the work per volume within a grain is known as:

$$dw = \sum_i \tau dy_i = \tau \sum_i |dy_i|$$

(6.3)

where τ is the critical resolved shear stress (CRSS) for the slip that is identical on all slip systems and dy_i is the incremental slip on an individual slip system. For a uniaxial

139

deformed polycrystal, the incremental work per unit volume due to the external stress is

known,

$$dw = \tau \, dy = \sigma_x d\varepsilon_x \qquad (6.4)$$

Equation (6.4) is then transformed into:

$$\sigma_x / \tau = dy / d\varepsilon_x = M \qquad (6.5)$$

where M is the Taylor factor.

Table 6.6 Summary of Taylor factors in Figure 6.22

Mapped regions Taylor factor (M)	(c)	(d)	(e)	(f)	(g)
2.26 – 2.54	39.84	24.67	14.42	14.09	20.39
2.54 – 2.83	8.15	5.65	5.74	11.51	12.11
2.83 – 3.11	8.13	12.07	11.51	17.32	16.64
3.11 – 3.39	4.94	9.53	18.90	25.11	24.17
3.39 – 3.67	38.94	49.44	48.08	31.97	26.70

Table 6.7 Summary of Taylor factors in Figure 6.23

Mapped regions Taylor factor (M)	(b)	(c)
2.26 – 2.54	25.29	20.80
2.54 – 2.83	7.81	11.47
2.83 – 3.11	12.06	12.73
3.11 – 3.39	18.10	22.43
3.39 – 3.67	36.74	32.57

The partition fractions of the mapped regions at different Taylor factor ranges are

summarized in Tables 6.6 and 6.7, respectively. The Taylor factor in this study is

calculated based on the slip system <111>/{110} in face-centered cubic (FCC) metal. For a randomly-textured polycrystalline FCC metal, the Taylor factor under a uniaxial tension Mt is 3.06 [153]. The Mt value (3.06) matches one of the discernible peaks in Figures 6.22 and 6.23. To some extent, it discloses the strength of texture in the mapped regions. The base metal in the electrodes attained a combination of fiber textures in <100> and <111> direction. As a result, the relative frequency at M=3.06 of the base metal at 10 welds was the lowest. Due to the high temperature and inclined pressure experienced by the electrode, the grains underwent dynamic recrystallization and the <111> and <100> fiber texture continuted to weaken. This process was reflected in the increased relative frequency at M=3.06 in the recrystallization regions (f-g) in Figure 6.22. The <100> fiber texture was weakened simultaneously, where the low relative frequency was found in all recrystallized regions (e-g) in Figure 6.22 and region (c) in Figure 6.23.

Moreover, the distribution of the Taylor factor indicated the deformation work required for a polycrystalline metal. Gains with high Taylor factor required more deformation energy. The rotation of grains due to the inclined pressure led to a substantial decline in the portion of <111> fibre texture. Thus, the fractions of the recrystallization regions (f-g) in Figure 6.22 and region (c) in Figure 6.23 at higher Taylor factors (3.39<M<3.67) were 31.97%, 26.7% and 32.57%, respectively, the lowest among all the mapped regions. Compared to base metal regions with high deformation resistance, the recrystallization regions around the electrode tip were likely to be deformed due to the decreased portion of high Taylor factor.

Local deformation analysis

To understand the potential deformation state of the worn electrodes, EBSD mapping evaluated local deformation of the recrystallization regions via the kernel average

misorientation (KAM), as shown in Figure 6.24. The KAM value is calculated via the average misorientation between the chosen point and the surrounding points, where any misorientation angle above 5° is excluded.
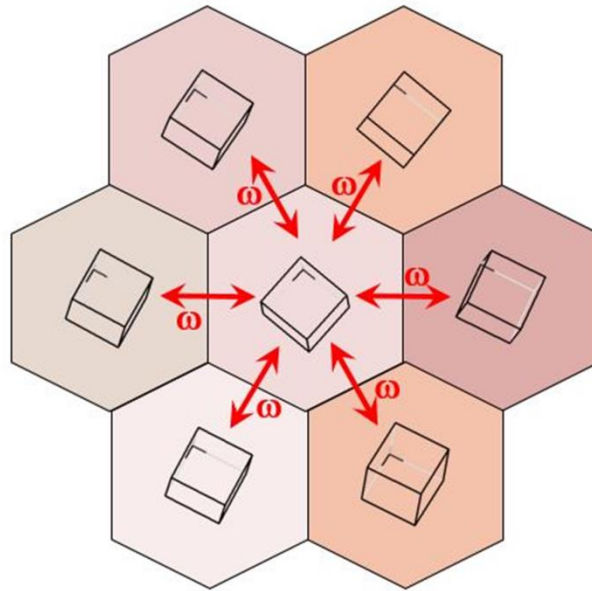
Figure 6.24 Schematic diagram of KAM calculation [154]
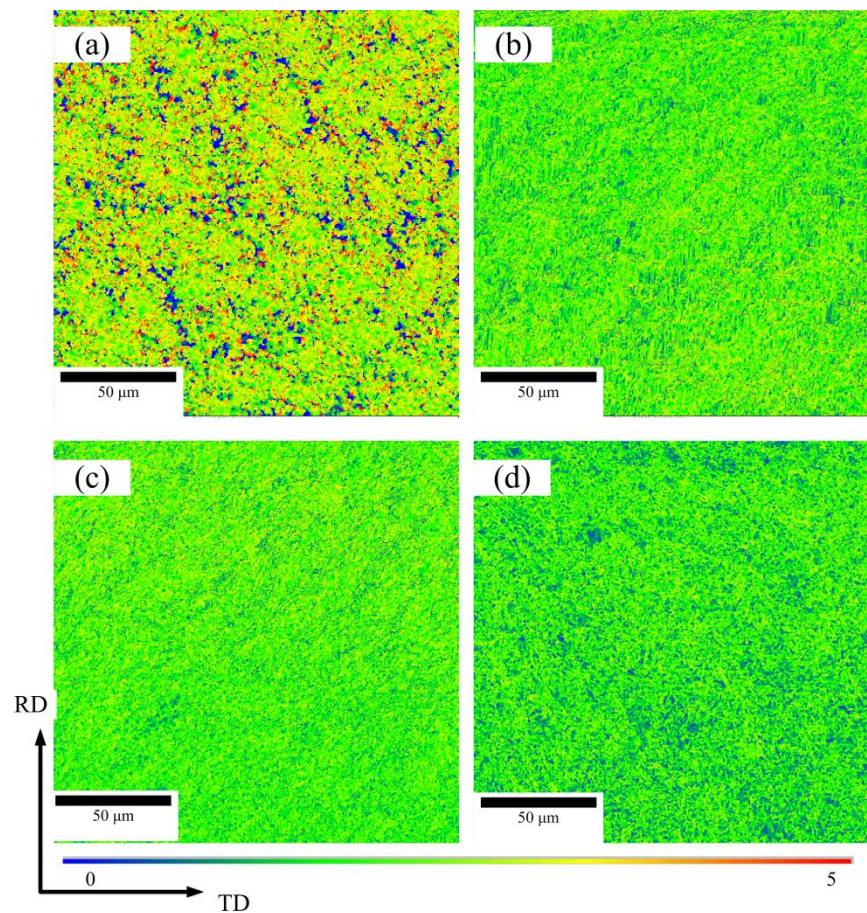
Figure 6.25 KAM mappings of recrystallized regions. (a-c) region e-g in GA worn electrode, (d) region c in GB worn electrode.

The KAM mappings of all the recrystallization regions are shown in Figure 6.25. The average KAM values fpr all chosen regions are manifested in Table 6.8 and Table **6.9**. After 10 welds, a strong variation in KAM values was found in the mapped recrystallization region. With further dynamic recrystallization, the KAM values are found to decline substantially in Figure 6.25 (b-d). The original fiber texture attained a high KAM value, indicating of relatively high deformed state. During the endurance test, the regions close to the electrode tip face experienced high temperature, and underwent recrystallization. The KAM values of recrystallized regions were found to drop significantly in both worn electrodes. This finding matched the Vickers microhardness test in the worn electrodes.

Table 6.8 Average KAM at the mapped regions in Figure 6.18

Mapped regions	(c)	(d)	(e)	(f)	(g)
KAM	3.06	2.99	2.66	2.14	2.15

Table 6.9 Average KAM at the mapped regions in Figure 6.19

Mapped regions	(b)	(c)
KAM	3.1	1.52

6.3 Summary of the influence of angular misalignment on electrode degradation

In this section, the influence of angular misalignment on electrode degradation was investigated via endurance test and microstructure characterization. It was found that the electrode degradation during welding of galvannealed steel and galvanized steel was substantially affected by the pre-set angular misalignment. Much shorter electrode life was found in the welding galvannealed steel, when significant pitting was found at 200 welds. In the welding of galvanized steel, no significant pitting was found at 200 welds, but the electrode tip diameter enlarged due to mushrooming effect.

Electrode degradation was found to be strongly associated with the electrode softening effect and IMC compound formation. Both galvannealed and galvanized coating reacted with the copper electrode and produced some brittle IMC products. In addition, the δ Fe-Zn phase from the galvannealed coating could be picked up by the electrode, which was considered to prevent further penetration of the Zn element. With angular misalignment, however, the temperature field developed on the electrode tip was non-uniform, causing a the difference in Fe concentration and leading to a much faster pitting rate in the GA electrode. The galvanized coating readily reacted with the

electrode copper to form Cu-Zn brass phase. Because electrode sticking occasionally occurred in the endurance test, the IMC product thickness was found to be relatively thin on the GB electrode. Electrode softening was another issue in electrode degradation. The GB electrode was found to experience much more severe mushrooming in the endurance test. Because the galvanized coating had poor electrical resistivity, a higher electrical current was used, that seemed to affect the level of recrystallization and created a softening effect. EBSD mapping was used to characterize the recrystallization regions of the different worn electrodes. From comparisons of the grain diameter, Taylor factor and KAM, it was concluded that dynamic recrystallization was the main softening mechanism on the electrodes welded with galvannealed and galvanized steel.

Chapter 7 Conclusion and Outlook

In this study, issues related to abnormal process conditions in the RSW were comprehensively investigated. Abnormal process conditions adversely affect the quality of spot welds in the plant environment, leading to a range of undersized welds and expulsion. Another potential issue could be the short electrode life under some abnormal process conditions. Thus, the weld sequence had to be closely monitored. However, while existing studies leading towards an online monitoring system had not fully considered abnormal process conditions, a considerable gap remained in understanding the influence of abnormal process conditions on the RSW process.

A RF-based online-monitoring system was first constructed using the DR signals. Unlike previous studies that only used DR signal from samples tested in the TST, samples made on the same sheets were also considered for constructing the monitoring system. Although the weld spacing met the minimum weld spacing criteria in mild steel, some obvious changes in the DR curves were seen. Yet the system showed a robust classification rate compared to other possible methods reported in the literature. More importantly, the RF method featured variable importance ranking, which could show users the importance of each input variables. Then misclassification between good welds and poor welds could be compensated accordingly.

To better monitor abnormal process conditions and achieve a good consistency with the current monitoring system, an ED signal was recommended in preference to the DR signal. Shunting, close-to-edge welds and airgap were found to change the portion of the welding current, the contact resistance, and the surrounding materials of the spot weld, respectively. Thus, the DR curves were found to shift downwards. In contrast, the decline between peak β and endpoint value in DR curves indicated the volume of the

146

melting material, that was unlike to the results under abnormal process conditions. Moreover, the ED was determined by the actual thermal expansion of the base metal, a finding that agreed well with conclusions from the previous studies. The nugget size under these conditions could be well predicted by the profile features from the ED curves, and the critical values under different abnormal process conditions were derived. The trends derived in ED curves were used to develop a current-compensation system to rule out the negative impact of abnormal process conditions in the plant environment.

Apart from suggesting a suitable signal for abnormal process conditions, the influence of abnormal process conditions on electrode degradation was investigated. Angular misalignment, a common form of electrode misalignment, was manually introduced into a pedestal welder. Galvannealed coated steel and galvanized steel were used, both of which showed very different electrode degradation mechanisms from those reported in previous studies. The missing δ Fe-Zn phase from the galvannealed coating caused rapid copper pick-up and pitting on the electrode, whereas the electrode tip welding with galvanized coating was found to be non-uniform. Quantitative analysis using EBSD mapping helped understanding of the influence of recrystallization on the electrode softening effect. The shift from elongated grain in base metal to equiaxed grain in the recrystallized region accounted for the substantial decline in the Vickers microhardness. Furthermore, due to the difference in physical properties in zinc coating, the level of recrystallization was found to be very different in the two tested electrodes.

This study focuses mainly on the impact of abnormal process conditions on mild steel and zinc-coated steel. All of them have peritectic transformation during solidification. Thus, it is also importatn to consider steels that do not have peritectic transformation. Recently, the research community has been working on the RSW of lightweight metal, such as aluminium and magnesium alloy. It is known that aluminium and magnesium

alloy attain lower electrical resistivity, making the DR curve more prone to shunting. Moreover, the IMC formation between Al and Mg with Cu is much more severe; electrode degradation would be significantly affected by the uneven distribution of IMC products under angular misalignment. Though the impact of electrode softening might be very limited, future studies should consider aluminium and magnesium alloy.

Bibliography

[1]   R. Bowers, C. Sorensen, T. Eagar, Electrode geometry in resistance spot welding, Welding Journal, 69(2) (1990).

[2]   H. Zhang, J. Senkara, Resistance welding: fundamentals and applications, CRC press, 2011.

[3]   A. Yadav, H. Katayama, K. Noda, H. Masuda, A. Nishikata, T. Tsuru, Effect of Fe–Zn alloy layer on the corrosion resistance of galvanized steel in chloride containing environments, Corrosion Science, 49(9) (2007) 3716-3731.

[4]   O. Ighodaro, E. Biro, Y. Zhou, Comparative effects of Al-Si and galvannealed coatings on the properties of resistance spot welded hot stamping steel joints, Journal of Materials Processing Technology, 236 (2016) 64-72.

[5]   J. Parker, N. Williams, R. Holliday, Mechanisms of electrode degradation when spot welding coated steels, Science and Technology of Welding and Joining, 3(2) (1998) 65-74.

[6]   B. Bouyousfi, T. Sahraoui, S. Guessasma, K.T. Chaouch, Effect of process parameters on the physical characteristics of spot weld joints, Materials & design, 28(2) (2007) 414-419.

[7]   M. Alizadeh-Sh, S. Marashi, M. Pouranvari, Resistance spot welding of AISI 430 ferritic stainless steel: phase transformations and mechanical properties, Materials & Design, 56 (2014) 258-263.

[8]   M. Pouranvari, S. Marashi, M. Alizadehsh, Welding metallurgy of dissimilar AISI 430/DQSK steels resistance spot welds, Welding Journal, 94(6) (2015) 203-210.

[9]   R.W.M. Alliance, Resistance welding manual, RWMA, Philadelphia Google Scholar, (2003).

[10]   J. Zou, Q. Zhao, Z. Chen, Surface modified long-life electrode for resistance spot welding of Zn-coated steel, Journal of Materials Processing Technology, 209(8) (2009) 4141-4146.

[11]   S. Alfaro, J. Vargas, M. Wolff, L. Vilarinho, Comparison between AC and MF-DC resistance spot welding by using high speed filming, Journal of Achievements in Materials and Manufacturing Engineering, 24(1) (2007) 333-339.

[12]   Swactec, in, https://www.swantec.com/technology/resistance-welding/.

[13]   T. Saito, Resistance spot weldability of coated sheet for automotive application, Welding international, 6(9) (1992) 695-699.

[14]   L. Friedman, R. McCauley, Influence of metallurgical characteristics on resistance welding of galvanized steel, Welding Journal, 48(10) (1969) S454-&.

[15]   J.E. Gould, M. Kimchi, D.H. Campbell, Weldability and electrode wear characteristics of hot-dip galvanized steel with and without a ferrophos containing primer, 0148-7191, SAE Technical Paper, 1988.

[16]   X. Hu, G. Zou, D. SJ, L. MY, J. JP, Y. Zhou, Effects of steel coatings on electrode life in resistance spot welding of galvannealed steel sheets, Materials transactions, 51(12) (2010) 2236-2242.

[17]   M. Pouranvari, S.P.H. Marashi, On the failure of low carbon steel resistance spot welds in quasi-static tensile–shear loading, Materials & Design, 31(8) (2010) 3647-3652.

[18]   D. Zhao, Y. Wang, L. Zhang, P. Zhang, Effects of electrode force on microstructure and mechanical behavior of the resistance spot welded DP600 joint, Materials & Design, 50 (2013) 72-77.

[19]   S. Aslanlar, A. Ogur, U. Ozsarac, E. Ilhan, Welding time effect on mechanical properties of automotive sheets in electrical resistance spot welding, Materials & Design, 29(7) (2008) 1427-1431.

[20]   M.H. Bina, M. Jamali, M. Shamanian, H. Sabet, Effect of Welding Time in the Resistance Spot Welded Dissimilar Stainless Steels, Transactions of the Indian Institute of Metals, 68(2) (2015) 247-255.

[21]   H. Moshayedi, I. Sattari-Far, Resistance spot welding and the effects of welding time and current on residual stresses, Journal of Materials Processing Technology, 214(11) (2014) 2545-2552.

[22]   N. Charde, Resistance Spot Welds of 304l Austenitic Stainless Steel, Part 1: Fundamental, Simulation, Weld Growth, Tensile Strength And Failure Mode Analysis, Indian Welding Journal, 48(2) (2015).

[23]   S. Babu, M. Santella, Z. Feng, B. Riemer, J. Cohron, Empirical model of effects of pressure and temperature on electrical contact resistance of metals, Science and Technology of Welding & Joining, 6(3) (2001) 126-132.

[24]   K. Zhou, L. Cai, Study on effect of electrode force on resistance spot welding process, Journal of applied physics, 116(8) (2014) 084902.

[25]   M. Pouranvari, Effect of welding parameters on the peak load and energy absorption of low-carbon steel resistance spot welds, ISRN Mechanical Engineering, 2011 (2011).

[26]   J. Shen, Y.S. Zhang, X.M. Lai, Effect of Electrode Force on Expulsion in Resistance Spot Welding with Initial Gap, in: Materials Science Forum, Trans Tech Publ, 2011, pp. 795-798.

[27]   H. Zhang, S.J. Hu, J. Senkara, S. Cheng, A statistical analysis of expulsion limits in resistance spot welding, Journal of Manufacturing Science and Engineering, 122(3) (2000) 501-510.

[28]   N.N. Wang, R.F. Qiu, F.F. Liu, M. Zhang, Q.Q. Xuan, Analyses of Nugget and Expulsion Formation Process during Resistance Spot Welding between Aluminum Alloy and Steel, in: Advanced Materials Research, Trans Tech Publ, 2014, pp. 7-10.

[29]   J. Senkara, H. Zhang, S. Hu, Expulsion prediction in resistance spot welding, WELDING JOURNAL, 83(4) (2004) 123-132.

[30]   W. Li, S. Cheng, S.J. Hu, J. Shriver, Statistical investigation on resistance spot welding quality using a two-state, sliding-level experiment, Journal of manufacturing science and engineering, 123(3) (2001) 513-520.

[31]   W. Li, D. Cerjanec, G.A. Grzadzinski, A comparative study of single-phase AC and multiphase DC resistance spot welding, Journal of manufacturing science and engineering, 127(3) (2005) 583-589.

[32]   J.E.G.a.M. Kimchi, Challenges in Welding New Sheet Steel Products, in: 33rd Mechanical Working and Steel Process Conference Proceedings, 1991.

[33]   H.E. Emre, R. Kaçar, Development of weld lobe for resistance spot-welded TRIP800 steel and evaluation of fracture mode of its weldment, The International Journal of Advanced Manufacturing Technology, 83(9) (2016) 1737-1747.

[34]   G. Weber, S. Göklü, Resistance spot welding of uncoated and zinc coated advanced high-strength steels (AHSS)—weldability and process reliability-influence of welding parameters, Welding in the World, 50(3-4) (2006) 3-12.

[35]   M. Tumuluru, The effect of coatings on the resistance spot welding behavior of 780 MPa dual-phase steel, WELDING JOURNAL-NEW YORK-, 86(6) (2007) 161.

[36] P. Howe, S.C. Kelley, A comparison of the resistance spot weldability of bare, hot-dipped, galvannealed, and electrogalvanized DQSK sheet steels, 0148-7191, SAE Technical Paper, 1988.

[37] J. Sawhill Jr, J. Baker, Spot weldability of high-strength sheet steels, Welding Journal, 59(1) (1980) 19.

[38] D. Dickinson, Welding in the Automotive Industry: State of the Art: a Report, Republic Steel Research Center, 1981.

[39] S. Babu, G. Goodwin, R. Rohde, Effect of boron on the microstructure of low-carbon steel resistance seam welds, WELDING JOURNAL-NEW YORK-, 77 (1998) 249-s.

[40] M. Pouranvari, S. Marashi, Critical review of automotive steels spot welding: process, structure and properties, Science and Technology of welding and joining, 18(5) (2013) 361-403.

[41] M. Pouranvari, Susceptibility to interfacial failure mode in similar and dissimilar resistance spot welds of DP600 dual phase steel and low carbon steel during cross-tension and tensile-shear loading conditions, Materials Science and Engineering: A, 546 (2012) 129-138.

[42] Ó. Martín, M. López, F. Martín, Artificial neural networks for quality control by ultrasonic testing in resistance spot welding, Journal of Materials Processing Technology, 183(2) (2007) 226-233.

[43] M. Pereda, J. Santos, Ó. Martín, J. Galán, Direct quality prediction in resistance spot welding process: Sensitivity, specificity and predictive accuracy comparative analysis, Science and Technology of Welding and Joining, 20(8) (2015) 679-685.

[44] C. Summerville, D. Adams, P. Compston, M. Doolan, Nugget Diameter in Resistance Spot Welding: A Comparison between a Dynamic Resistance Based Approach and Ultrasound C-scan, Procedia Engineering, 183 (2017) 257-263.

[45] J. Liu, G. Xu, X. Gu, G. Zhou, Ultrasonic test of resistance spot welds based on wavelet package analysis, Ultrasonics, 56 (2015) 557-565.

[46] Y. Zhang, H. Shan, Y. Li, C.F. Zhao, Z. Luo, J. Guo, C.Y. Ma, Effects of the oxide film on the spot joining of aluminum alloy sheets: a comparative study between resistance spot welding and resistance spot clinching, The International Journal of Advanced Manufacturing Technology, (2017) 1-10.

[47] M. Jou, Real time monitoring weld quality of resistance spot welding for the fabrication of sheet metal assemblies, Journal of materials processing technology, 132(1) (2003) 102-113.

[48] P. James, H. Chandler, J. Evans, J. Wen, D. Browne, C. Newton, The effect of mechanical loading on the contact resistance of coated aluminium, Materials Science and Engineering A, 230(1-2) (1997) 194-201.

[49] P. Podržaj, S. Simončič, A machine vision-based electrode displacement measurement, Welding in the World, 58(1) (2014) 93-99.

[50] S. Simončič, P. Podržaj, Resistance spot weld strength estimation based on electrode tip displacement/velocity curve obtained by image processing, Science and Technology of Welding and Joining, 19(6) (2014) 468-475.

[51] S. Simončič, P. Podržaj, Image-based electrode tip displacement in resistance spot welding, Measurement Science and Technology, 23(6) (2012) 065401.

[52] L. Xinmin, Z. Xiaoyun, Z. Yansong, C. Guanlong, Weld quality inspection based on online measured indentation from servo encoder in resistance spot welding, IEEE Transactions on Instrumentation and Measurement, 56(4) (2007) 1501-1505.

[53] X. Wang, G. Meng, Q. Ye, W. Xie, Z. Feng, Real-Time Quality Estimation of Resistance Spot Welding Based on Electrode Displacement Characteristics and HMM, in: Natural Computation, 2009. ICNC'09. Fifth International Conference on, IEEE, 2009, pp. 634-638.

[54] Y. Zhang, H. Wang, G. Chen, X. Zhang, Monitoring and intelligent control of electrode wear based on a measured electrode displacement curve in resistance spot welding, Measurement Science and Technology, 18(3) (2007) 867.

[55] Y. Li, J. Xu, G. Chen, Z. Lin, Real-time measuring system design and application of thermal expansion displacement during resistance spot welding process, in: SPIE, 2005.

[56] C. Ji, L. Deng, Quality control based on electrode displacement and force in resistance spot welding, Frontiers of Mechanical Engineering in China, 5(4) (2010) 412-417.

[57] C. Ji, Y. Zhou, Dynamic electrode force and displacement in resistance spot welding of aluminum, Journal of Manufacturing Science and Engineering, 126(3) (2004) 605-610.

[58] X. Wang, Y. Li, G. Meng, Monitoring of resistance spot weld quality using electrode vibration signals, Measurement Science and Technology, 22(4) (2011) 045705.

[59] L. Kuščer, I. Polajnar, J. Diaci, A method for measuring displacement and deformation of electrodes during resistance spot welding, Measurement Science and Technology, 22(6) (2011) 067002.

[60] S. Gedeon, C. Sorensen, K. Ulrich, T. Eagar, Measurement of dynamic electrical and mechanical properties of resistance spot welds, Welding Journal, 66(12) (1987) 378-385.

[61] Q. Fan, G. Xu, T. Wang, The influence of electrode tip radius on dynamic resistance in spot welding, The International Journal of Advanced Manufacturing Technology, (2017) 1-6.

[62] K. Zhou, L. Cai, Online nugget diameter control system for resistance spot welding, The International Journal of Advanced Manufacturing Technology, 68(9-12) (2013) 2571-2588.

[63] D. Zhao, Y. Wang, S. Sheng, Z. Lin, Real time monitoring weld quality of small scale resistance spot welding for titanium alloy, Measurement, 46(6) (2013) 1957-1963.

[64] J. Wen, C. Wang, G. Xu, X. Zhang, Real time monitoring weld quality of resistance spot welding for stainless steel, ISIJ international, 49(4) (2009) 553-556.

[65] Q. Fan, G. Xu, X. Gu, Expulsion characterization of stainless steel resistance spot welding based on dynamic resistance signal, Journal of Materials Processing Technology, 236 (2016) 235-240.

[66] H. Sun, X. Lai, Y. Zhang, J. Shen, Effect of variable electrode force on weld quality in resistance spot welding, Science and Technology of Welding and Joining, 12(8) (2007) 718-724.

[67] H. Tang, W. Hou, S. Hu, H. Zhang, Force characteristics of resistance spot welding of steels.

[68] X. Wang, Y. Li, R. Li, G. Meng, Experimental study on electrode displacement fluctuation characteristics during resistance spot welding, Science and Technology of Welding and Joining, 16(2) (2011) 140-145.

[69] J. Ruisz, J. Biber, M. Loipetsberger, Quality evaluation in resistance spot welding by analysing the weld fingerprint on metal bands by computer vision,

The International Journal of Advanced Manufacturing Technology, 33(9) (2007) 952-960.

[70] X. Wan, Y. Wang, D. Zhao, Y. Huang, Z. Yin, Weld quality monitoring research in small scale resistance spot welding by dynamic resistance and neural network, Measurement, 99 (2017) 120-127.

[71] Y. Luo, W. Rui, X. Xie, Y. Zhu, Study on the nugget growth in single-phase AC resistance spot welding based on the calculation of dynamic resistance, Journal of Materials Processing Technology, 229 (2016) 492-500.

[72] Y. Cho, S. Rhee, New technology for measuring dynamic resistance and estimating strength in resistance spot welding, Measurement Science and Technology, 11(8) (2000) 1173.

[73] H. Wang, Y. Zhang, G. Chen, Resistance spot welding processing monitoring based on electrode displacement curve using moving range chart, Measurement, 42(7) (2009) 1032-1038.

[74] X. Wan, Y. Wang, D. Zhao, Quality monitoring based on dynamic resistance and principal component analysis in small scale resistance spot welding process, The International Journal of Advanced Manufacturing Technology, (2016) 1-9.

[75] D.W. Adams, C.D. Summerville, B.M. Voss, J. Jeswiet, M.C. Doolan, Correlating Variations in the Dynamic Resistance Signature to Weld Strength in Resistance Spot Welding Using Principal Component Analysis, Journal of Manufacturing Science and Engineering, 139(4) (2017) 044502.

[76] H. Zhang, Y. Hou, J. Zhang, X. Qi, F. Wang, A new method for nondestructive quality evaluation of the resistance spot welding based on the radar chart method and the decision tree classifier, The International Journal of Advanced Manufacturing Technology, 78(5-8) (2015) 841-851.

[77] Y. Cho, S. Rhee, Quality estimation of resistance spot welding by using pattern recognition with neural networks, IEEE transactions on instrumentation and measurement, 53(2) (2004) 330-334.

[78] N. Williams, J. Parker, Review of resistance spot welding of steel sheets Part 2 Factors influencing electrode life, International Materials Reviews, 49(2) (2004) 77-108.

[79] B. Wang, L. Hua, X. Wang, Y. Song, Y. Liu, Effects of electrode tip morphology on resistance spot welding quality of DP590 dual-phase steel, The International Journal of Advanced Manufacturing Technology, 83(9-12) (2016) 1917-1926.

[80] L. Han, M. Thornton, D. Boomer, M. Shergold, Effect of aluminium sheet surface conditions on feasibility and quality of resistance spot welding, Journal of Materials Processing Technology, 210(8) (2010) 1076-1082.

[81] X. Wan, Y. Wang, P. Zhang, Modelling the effect of welding current on resistance spot welding of DP600 steel, Journal of Materials Processing Technology, 214(11) (2014) 2723-2729.

[82] Z. Hou, I.-S. Kim, Y. Wang, C. Li, C. Chen, Finite element analysis for the mechanical features of resistance spot welding process, Journal of Materials Processing Technology, 185(1) (2007) 160-165.

[83] G. Zhong, Finite element analysis of resistance spot welding process, in: Control and Decision Conference, 2009. CCDC'09. Chinese, IEEE, 2009, pp. 5799-5802.

[84] H. Eisazadeh, M. Hamedi, A. Halvaee, New parametric study of nugget size in resistance spot welding process using finite element method, Materials & Design, 31(1) (2010) 149-157.

153

[85]   E. Gauthier, D. Carron, P. Rogeon, P. Pilvin, C. Pouvreau, T. Lety, F. Primaux, Numerical Modeling of Electrode Degradation During Resistance Spot Welding Using CuCrZr Electrodes, Journal of materials engineering and performance, 23(5) (2014) 1593-1599.

[86]   S. Babu, M. Santella, W. Peterson, Modeling resistance spot welding electrode life, AWS Welding Shows, Chicago, Illinois, (2004).

[87]   M. Kondo, T. Konishi, K. Nomura, H. Kokawa, Degradation mechanism of electrode tip during alternate resistance spot welding of zinc coated and uncoated steel sheets, Science and Technology of Welding and Joining, 15(1) (2010) 76-80.

[88]   P. Podržaj, S. Simončič, Resistance spot welding control based on the temperature measurement, Science and Technology of Welding and Joining, 18(7) (2013) 551-557.

[89]   E. Kim, T. Eagar, Interfacial Temperature Profiles in Simulated Resistance Spot Welding of Bare and Zinc Coated Steel, Welding Journal, 94 (2015) 35-43.

[90]   R. Holliday, J. Parker, N. Williams, Relative contribution of electrode tip growth mechanisms in spot welding zinc coated steels, Welding in the World, 4(37) (1996) 186-193.

[91]   F. Lu, P. Dong, Model for estimating electrode face diameter during resistance spot welding, Science and technology of welding and joining, 4(5) (1999) 285-289.

[92]   K.R. Chan, Weldability and degradation study of coated electrodes for resistance spot welding, (2005).

[93]   Y. Zhao, Y. Zhang, X. Lai, P. Wang, Effect of inserted strips on electrode degradation in resistance spot welding, Welding Journal, 18(20) (2014) 0-7.

[94]   U.a.H. Dilthey, S, Welding Journal, 1(34) (1998).

[95]   X. Hu, G. Zou, S. Dong, M. Lee, J. Jung, Y. Zhou, Effects of steel coatings on electrode life in resistance spot welding of galvannealed steel sheets, Materials transactions, 51(12) (2010) 2236-2242.

[96]   Z. Chen, Y. Zhou, N. Scotchmer, Coatings on resistance welding electrodes to extend life, 0148-7191, SAE Technical Paper, 2006.

[97]   W. Mazur, A. Kyriakopoulos, N. Bott, D. West, Use of modified electrode caps for surface quality welds in resistance spot welding, Journal of Manufacturing Processes, 22 (2016) 60-73.

[98]   J. Peng, S. Fukumoto, L. Brown, N. Zhou, Image analysis of electrode degradation in resistance spot welding of aluminium, Science and technology of welding and joining, 9(4) (2004) 331-336.

[99]   A. Abdulhadi, M. Gdeisat, D. Burton, F. Lilley, Assessing the Quality of Spot Welding Electrode Tips Using Image Processing Techniques, in: Proceedings of the World Congress on Engineering, 2011, pp. 6-8.

[100]   J. Cullen, N. Athi, M. Al-Jader, P. Johnson, A. Al-Shamma'a, A. Shaw, A. El-Rasheed, Multisensor fusion for on line monitoring of the quality of spot welding in automotive industry, Measurement, 41(4) (2008) 412-423.

[101]   Y. Cho, W. Li, S. Hu, Design of experiment analysis and weld lobe estimation for aluminum resistance spot welding, Welding journal, 85(3) (2006) 45-51.

[102]   C.V. Nielsen, W. Zhang, W. Perret, P.A. Martins, N. Bay, Three-dimensional simulations of resistance spot welding, Proceedings of the Institution of Mechanical Engineers, Part D: Journal of Automobile Engineering, 229(7) (2015) 885-897.

[103] ISO, Resistance welding, Weldability, Part 2: Alternative procedures for the assessment of sheet steels for spot welding, in, 2004.

[104] Q.H. Qin, Fracture mechanics of piezoelectric materials, in, WIT Press, Southampton, 2001.

[105] Q.H. Qin, S.-W. Yu, An arbitrarily-oriented plane crack terminating at the interface between dissimilar piezoelectric materials, International Journal of Solids and Structures, 34(5) (1997) 581-590.

[106] Q.H. Qin, Y.-W. Mai, A closed crack tip model for interface cracks in thermopiezoelectric materials, International Journal of Solids and Structures, 36(16) (1999) 2463-2479.

[107] Q.H. Qin, Y.-W. Mai, S.-W. Yu, Effective moduli for thermopiezoelectric materials with microcracks, International Journal of Fracture, 91(4) (1998) 359-371.

[108] Q.H. Qin, Y.-W. Mai, S.-W. Yu, Some problems in plane thermopiezoelectric materials with holes, International Journal of Solids and Structures, 36(3) (1999) 427-439.

[109] S. Yu, Q.H. Qin, Damage analysis of thermopiezoelectric properties: Part I—crack tip singularities, Theoretical and Applied Fracture Mechanics, 25(3) (1996) 263-277.

[110] H. Wang, Q.H. Qin, A meshless method for generalized linear or nonlinear Poisson-type problems, Engineering Analysis with Boundary Elements, 30(6) (2006) 515-521.

[111] Q.H. Qin, Trefftz finite element method and its applications, Applied Mechanics Reviews, 58(5) (2005) 316-337.

[112] H. Wang, Q.H. Qin, Meshless approach for thermo-mechanical analysis of functionally graded materials, Engineering Analysis with Boundary Elements, 32(9) (2008) 704-712.

[113] J. Jirousek, Q.H. Qin, Application of hybrid-Trefftz element approach to transient heat conduction analysis, Computers & Structures, 58(1) (1996) 195-201.

[114] J. Jirousek, A. Wroblewski, Q.H. Qin, X.Q. He, A family of quadrilateral hybrid-Trefftz p-elements for thick plate analysis, Computer Methods in Applied Mechanics and Engineering, 127(1) (1995) 315-344.

[115] H. Wang, Q.H. Qin, Hybrid FEM with fundamental solutions as trial functions for heat conduction simulation, Acta Mechanica Solida Sinica, 22(5) (2009) 487-498.

[116] Q.H. Qin, Hybrid-Trefftz finite element method for Reissner plates on an elastic foundation, Computer Methods in Applied Mechanics and Engineering, 122(3-4) (1995) 379-392.

[117] Q.H. Qin, Hybrid Trefftz finite-element approach for plate bending on an elastic foundation, Applied Mathematical Modelling, 18(6) (1994) 334-339.

[118] Q.H. Qin, Variational formulations for TFEM of piezoelectricity, International Journal of Solids and Structures, 40(23) (2003) 6335-6346.

[119] H. Wang, Q.H. Qin, FE approach with Green's function as internal trial function for simulating bioheat transfer in the human eye, Archives of Mechanics, 62(6) (2010) 493-510.

[120] B. Wang, M. Lou, Q. Shen, Y. Li, H. Zhang, Shunting effect in resistance spot welding steels—part 1: experimental study, Welding Journal, 92(6) (2013).

[121] Y. Li, B. Wang, Q. Shen, M. Lou, H. Zhang, Shunting effect in resistance spot welding steels—part 2: theoretical analysis, Welding Journal, 92(8) (2013) 231-238.

[122] J. Bi, J. Song, Q. Wei, Y. Zhang, Y. Li, Z. Luo, Characteristics of shunting in resistance spot welding for dissimilar unequal-thickness aluminum alloys under large thickness ratio, Materials & Design, 101 (2016) 226-235.

[123] Y. Li, J. Bi, Y. Zhang, Z. Luo, W. Liu, Shunting characteristics in triangular arranged resistance spot welding of dissimilar unequal-thickness aluminum alloys, The International Journal of Advanced Manufacturing Technology, (2017) 1-8.

[124] H. Chang, H. Cho, A study on the shunt effect in resistance spot welding, Welding Journal, 69(8) (1990) 308-316.

[125] M.S. Choobi, C. Nielsen, N. Bay, Finite Element and Experimental Study of Shunting in Resistance Spot Welding, in: Proceedings of the 11th International Seminar on Numerical Analysis of Weldability, 2015, pp. 27-30.

[126] D. Browne, H. Chandler, J. Evans, P. James, J. Wen, C. Newton, Computer simulation of resistance spot welding in aluminum: Part II, Welding Journal, 74(12) (1995).

[127] H. Zhang, F. Wang, T. Xi, J. Zhao, L. Wang, W. Gao, A novel quality evaluation method for resistance spot welding based on the electrode displacement signal and the Chernoff faces technique, Mechanical Systems and Signal Processing, 62 (2015) 431-443.

[128] L. Wang, Y. Hou, H. Zhang, J. Zhao, T. Xi, X. Qi, Y. Li, A new measurement method for the dynamic resistance signal during the resistance spot welding process, Measurement Science and Technology, 27(9) (2016) 095009.

[129] D. Venugopal, M. Das, V. Fernandez, Study and implementation of a force stepper and a part fit-up solver algorithm for a servo controlled MFDC spot welder, in: Electro/Information Technology, 2009. eit'09. IEEE International Conference on, IEEE, 2009, pp. 286-291.

[130] P. Podržaj, B. Jerman, S. Simončič, Poor fit-up condition in resistance spot welding, Journal of Materials Processing Technology, 230 (2016) 21-25.

[131] S. Brauser, L.-A. Pepke, G. Weber, M. Rethmeier, Influence of production-related gaps on strength properties and deformation behaviour of SPOT welded trip steel HCT690T, Welding in the World, 56(3-4) (2012) 115-125.

[132] P. Podržaj, I. Polajnar, J. Diaci, Z. Kariž, Expulsion detection system for resistance spot welding based on a neural network, Measurement Science and Technology, 15(3) (2004) 592.

[133] M. Kimchi, J. Gould, Effects of prepulse resistance spot welding schedules on the weldability characteristics of galvanized steel, 0148-7191, SAE Technical Paper, 1990.

[134] Y. Zhang, J. Shen, X. Lai, Influence of electrode force on weld expulsion in resistance spot welding of dual phase steel with initial gap using simulation and experimental method, ISIJ international, 52(3) (2012) 493-498.

[135] Y. Zhang, G. Chen, A neuro-fuzzy approach to part fitup fault control during resistance spot welding using servo gun, in: International Conference on Natural Computation, Springer, 2005, pp. 1060-1068.

[136] R.B. Hirsch, Making resistance spot welding safer, Welding Journal, 86(2) (2007).

[137] P. Zhang, H. Zhang, J. Chen, Y. Ma, Quality monitoring of resistance spot welding based on electrode displacement characteristics analysis, Frontiers of Mechanical Engineering in China, 2(3) (2007) 330-335.

[138] X. Wan, Y. Wang, D. Zhao, Y. Huang, A comparison of two types of neural network for weld quality prediction in small scale resistance spot welding, Mechanical Systems and Signal Processing, 93 (2017) 634-644.

[139] M. El-Banna, D. Filev, R.B. Chinnam, Online qualitative nugget classification by using a linear vector quantization neural network for resistance spot welding, The International Journal of Advanced Manufacturing Technology, 36(3) (2008) 237-248.

[140] L. Breiman, Random forests, Machine learning, 45(1) (2001) 5-32.

[141] Ó. Martín, M. Pereda, J.I. Santos, J.M. Galán, Assessment of resistance spot welding quality based on ultrasonic testing and tree-based techniques, Journal of Materials Processing Technology, 214(11) (2014) 2478-2487.

[142] A. Liaw, M. Wiener, Classification and regression by randomForest, R news, 2(3) (2002) 18-22.

[143] D. Chen, J.-C. Kuo, W.-T. Wu, Effect of microscopic parameters on EBSD spatial resolution, Ultramicroscopy, 111(9) (2011) 1488-1494.

[144] F. Provost, P. Domingos, Well-trained PETs: Improving probability estimation trees, (2000).

[145] X. Lai, X. Zhang, Y. Zhang, G. Chen, Weld quality inspection based on online measured indentation from servo encoder in resistance spot welding, IEEE Transactions on Instrumentation and Measurement, 56(4) (2007) 1501-1505.

[146] M. Pouranvari, S. Marashi, Factors affecting mechanical properties of resistance spot welds, Materials Science and Technology, 26(9) (2010) 1137-1144.

[147] X. Wan, Y. Wang, D. Zhao, Quality monitoring based on dynamic resistance and principal component analysis in small scale resistance spot welding process, Int J Adv Manuf Tech, (2016) 1-9.

[148] X. Zhang, G. Chen, Y. Zhang, Characteristics of electrode wear in resistance spot welding dual-phase steels, Materials & Design, 29(1) (2008) 279-283.

[149] F. MÜFTÜOĞLU, T. Keskinel, Effect of coating thickness on electrode life in the spot welding of galvanized steels, Turkish Journal of Engineering and Environmental Sciences, 31(3) (2007) 183-187.

[150] H. Tang, W. Hou, S. Hu, H. Zhang, Z. Feng, M. Kimchi, Influence of welding machine mechanical characteristics on the resistance spot welding process and weld quality, Welding Journal, 82(5) (2003) 116-124.

[151] W. Zhisheng, S. Ping, L. Jinrui, H. Shengsun, Effect of deep cryogenic treatment on electrode life and microstructure for spot welding hot dip galvanized steel, Materials & design, 24(8) (2003) 687-692.

[152] S. Dong, G. Kelkar, Y. Zhou, Electrode sticking during micro-resistance welding of thin metal sheets, IEEE transactions on electronics packaging manufacturing, 25(4) (2002) 355-361.

[153] S. Suresh, Fatigue of materials, Cambridge university press, 1998.

[154] R. Kloe, DO YOU WANT TO BE AVERAGE(D)?, in, https://edaxblog.com/2015/09/22/do-you-want-to-be-averaged/.

List of Publications

B Xing, Y Xiao, QH Qin, H Cui, Quality assessment of resistance spot welding process based on dynamic resistance signal and random forest based. The International Journal of Advanced Manufacturing Technology, 94 (2018), 327-339.

B Xing, Y Xiao, QH Qin Characteristics of shunting effect in resistance spot welding in mild steel based on electrode displacement. Measurement 115 (2018) 233–242.

B Xing, S Yan, H Zhou, H Chen, QH Qin, Qualitative and quantitative analysis of misaligned electrode degradation when welding galvannealed steel, The International Journal of Advanced Manufacturing Technology, 97 (2018), 629-640.

Publications not related to this thesis

Xing et.al. Atomistic study for the vibrational properties on $\Sigma 5$ symmetric tilt bicrystal copper nanowires. Applied Mechanics & Materials, (2016) :846.

Xing et al. Deformation mechanism of kink-step distorted coherent twin boundaries in copper nanowire.AIMS Materials Science, 4(1) (2016). : 102-117.

Xing, B, Yan, S, Jiang, W, & Qin, Q.H. Effect of Inclination Angle on Mechanical Behaviour and Deformation Asymmetry in Aluminium Bicrystal. Journal of Integrated Design and Process Science. DOI 10.3233/jid-2017-0009

S Yan, B Xing, H Zhou, Y Xiao, QH Qin, H Chen. Effect of filling materials on the microstructure and properties of hybrid laser welded Al-Mg-Si alloys joints. erials Characterization, 144(2018), 205-218

Yan, H Zhou, B Xing, S Zhang, L Li, QH Qin. Crystal plasticity in fusion zone of a hybrid laser welded Al alloys joint: From nanoscale to macroscale. Materials & Design, 160(2018), 313-324